

All-optical spinor Bose-Einstein condensation and the spinor dynamics-driven atom laser

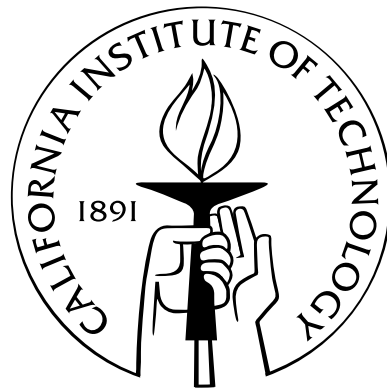
Dissertation by

Nathan Eric Lundblad

In Partial Fulfillment of the Requirements

for the Degree of

Doctor of Philosophy



California Institute of Technology

Pasadena, California

2006

(Defended May 19, 2006)

© 2006

Nathan Eric Lundblad

All Rights Reserved

For my parents

In memoriam—Robert O. Patterson, 1913–2005

Acknowledgments

From all I hear of (Gottfried Wilhelm) Leibniz he must be very intelligent, and pleasant company in consequence. It is rare to find learned men who are clean, do not stink, and have a sense of humour.

ELISABETH CHARLOTTE, PRINCESS PALATINE
A letter to Sophie Charlotte, 30 July 1705.

MY TIME AT CALTECH AND JPL has been shaped by the presence of several remarkable individuals. It is no exaggeration to say that this thesis and the work documented within would not exist without their influence, for which I am profoundly grateful.

First and foremost, I would like to acknowledge my advisor at JPL, Lute Maleki, who gave me an opportunity and a challenge five years ago to which I am proud to think I have risen. His unending support and enthusiasm for my project were absolute pillars when the experimental going was rough, and his optimism and guidance were sustaining. I am particularly appreciative of his well-calibrated sense of timing—when to leave me to seek answers myself, and when to intervene for the better.

Ken Libbrecht, my advisor at Caltech, has been both mentor and confessor to me, and the existence of this thesis is a credit to his patient encouragement. My notions of what it means to be a scientist have been heavily influenced by him, and I am proud to call myself his student.

Most of what I know about being a practicing physicist is due to Rob Thompson. His willingness to let me run amok in the early stages of the BEC experiment represented mentorship above and beyond the call of duty, and his constant open-door

policy for discussing matters of diverse stripe kept me time and again from reinventing the wheel, and also illuminated research pathways that I otherwise would not have seen. His insight and support were invaluable, and my gratitude for his scientific fostering is considerable.

Among my co-workers I would especially like to thank Eric Burt and Bill Klipstein for advice and helpful discussions over the years. An encouraging word at the right time from them meant more than I suspect they know, and their influence on this thesis was not small. The little village of Building 298 was a wonderful place to work, and I feel lucky to have learned from so many people, including Nan Yu, Jim Kohel, Dima Strelakov, Daphna Enzer, Meirong Tu, Bob Tjoelker, Jaime Ramirez-Serrano, Brent Young, Vlad Iltchenko, Brana Jelenkovic, Maggie Beach, and John Dick. I would like to recognize my fellow students: Dave Aveline, who I feel honored to pass the torch to, Makan Mohageg, Ivan Grudin, and Jim Kellogg. Naushad Khakoo and Jeffrey Naecker were my summer students in 2002 and 2005, respectively, and I hope they learned from me as I learned from teaching them. This thesis is also a credit to my undergraduate mentors: Morgan Mitchell, Ray Chiao, Tim Bolton (at KSU), and Carl Heiles, from all of whose considerate and effective teaching I continue to reap benefits.

I cannot overstate the role played by my friends in the traversal of this long road. Alex Papandrew and Ian Swanson are the finest of men—I'm honored to have them as friends, and knowing them has made the vicissitudes of these years worthwhile. Alan Smith, while always far away, has nevertheless been a rock of support. The gentlemen of Caltech Rugby have been nothing short of outstanding as friends and teammates, from the oldest ones who recruited me to the newest rookie. Mary Laura Lind has been a treasured friend, and her ability to motivate the writing of this thesis has only increased my appreciation of her friendship. Nelly Khidekel has been a true friend from the very beginning. Jason Keith bettered my time at Caltech with his loyalty and character, and I was glad for his presence both as my fellow prop and as my friend. Christine Thomas has been an unfailing source of support and a

confidante of the first order, for which I am grateful. Jane Khudyakov is a bright light in the occasional murk of Caltech life, and for lending me strength when I was on shaky ground I am in her debt. Allyson Beatrice bears a special responsibility for the completion of this thesis; her efforts at keeping the group at JPL under control and running smoothly have been superhuman, yet they are paltry in comparison to her contributions as a friend, confidante, and general well-wisher. Mary Devlin has been a wonderful roommate and friend, as have her cats, which have been essential to my stress relief over the past year. Several people from my entry class deserve particular mention, namely Parsa Bonderson, Andy Berglund, John Stockton, and especially Megan Elizabeth Eckart; it is a fine profession indeed where I can know these people both as friends and as colleagues. I am lucky to have a group of my oldest companions within driving distance; Mike Hill and Ian and Megumi Hurst have been a constant source of fun and encouragement. To the various gentlemen with whom I have had the pleasure of sharing a poker table these last several years, my thanks—depending on the stakes and the game they were either blessed or cursed with my presence, but regardless, I looked forward to every one of those games. I cannot neglect to mention Devin Sullivan and Rob Fergus, two good fellows who lit up my early years here, nor two of my oldest friends, Jordan Zamir and Tater Read. I could not phrase it any better:

*Think where man's glory most begins and ends,
And say my glory was I had such friends.*

Penultimately, it would be remiss of me not to cast thanks into the void toward Neal Stephenson, whose recent books provided much more than the occasional epigram—books that those readers who are amused by such things should read, and those who think that I am too long-winded should weigh.

To bring these acknowledgements to a close, I would like to recognize the constant flow of love and support from my family, to whom this thesis is dedicated: Mom, Dad, Jen, Robert, Mimi, Roger, and Jerry—*thank you*.

Abstract

OPTICAL TRAPPING as a viable means of exploring the physics of ultracold dilute atomic gases has revealed a new spectrum of physical phenomena. In particular, macroscopic and sudden occupation of the ground state below a critical temperature—a phenomenon known as Bose-Einstein condensation—has become an even richer system for the study of quantum mechanics, ultracold collisions, and many-body physics in general. Optical trapping liberates the spin degree of the BEC, making the order parameter vectorial (‘spinor BEC’), as opposed to the scalar order of traditional magnetically trapped condensates.

The work described within is divided into two main efforts. The first encompasses the all-optical creation of a Bose-Einstein condensate in rubidium vapor. An all-optical path to spinor BEC (as opposed to transfer to an optical trap from a magnetic-trap condensate) was desired both for the simplicity of the experimental setup and also for the potential gains in speed of creation; evaporative cooling, the only known path to dilute-gas condensation, works only as efficiently as the rate of elastic collisions in the gas, a rate that starts out much higher in optical traps. The first all-optical BEC was formed elsewhere in 2001; the years following saw many groups worldwide seeking to create their own version. Our own all-optical spinor BEC, made with a single-beam dipole trap formed by a focused CO₂ laser, is described here, with particular attention paid to trap loading, measurement of trap parameters, and the use of a novel 780 nm high-power laser system.

The second part describes initial experiments performed with the nascent condensate. The spinor properties of the condensate are documented, and a measurement is

made of the density-dependent rate of spin mixing in the condensate. In addition, we demonstrate a novel dual-beam atom laser formed by outcoupling oppositely polarized components of the condensate, whose populations have been coherently evolved through spin dynamics. We drive coherent spin-mixing evolution through adiabatic compression of the initially weak trap. Such dual beams, nominally number-correlated through the angular momentum-conserving collision $2m_0 \rightleftharpoons m_{+1} + m_{-1}$ have been proposed as tools to explore entanglement and squeezing in Bose-Einstein condensates.

Contents

Acknowledgments	iv
Abstract	vii
Preface	1
1 Background	9
1.1 Bose-Einstein condensation	10
1.1.1 Evaporative cooling	12
1.1.2 The condensate wavefunction	13
1.1.3 Condensate expansion	16
1.2 Optical trapping	17
1.2.1 History	20
1.3 Atom lasers	21
1.4 Spinor BEC	22
1.4.1 Spin mixing	25
1.4.2 Entanglement and correlation	26
2 Apparatus	29
2.1 Resonant light	30
2.1.1 The doubled 1560 nm system	31
2.1.2 Offset locking the doubled 1560 nm laser	34
2.1.3 Repump light, probe light, and absorptive imaging	36
2.2 Laser cooling setup	42

2.2.1	Vacuum	42
2.2.2	The 2D-MOT and 3D-MOT	43
2.3	The dipole trap	48
2.3.1	Beam design	48
2.3.2	Intensity measurement and control	52
2.3.3	Alignment	53
3	All-optical BEC	58
3.1	Loading the dipole trap	58
3.1.1	Background on technique	60
3.1.2	Our approach	62
3.2	Characterization and phase space density	66
3.2.1	Number	67
3.2.2	Temperature	69
3.2.3	Trap frequencies	75
3.3	First observations of condensation	78
3.3.1	Free evaporation	79
3.3.2	Evaporative paths and gravity correction	79
3.3.3	Condensation	84
3.4	BEC palette	87
3.4.1	The supported condensate	90
3.4.2	The downward-directed atom laser	93
4	Spinor dynamics and the dual-beam atom laser	96
4.1	Observations of spin mixing	96
4.1.1	Magnetic field issues	97
4.1.2	Density, adiabatic compression, and spin mixing	99
4.2	The dual-beam atom laser	105
4.2.1	Varieties	106
4.2.2	Modeling	109

Concluding Remarks	113
A Rubidium energy levels	118
B Offset lock circuit diagram	119
C Two-species cold atomic beam	121
D High power frequency doubling	126
Bibliography	133
Vita	150

List of Figures

1.1	Asymmetric mean-field expansion of the condensate	17
2.1	Diagram of the doubled-1560 nm fiber amplifier system.	33
2.2	Diagram of the offset-locking setup for the doubled 1560 nm laser.	37
2.3	Spectrum analyzer trace of 1560 nm/probe beat signal: span 50 kHz	37
2.4	Spectrum analyzer trace of 1560 nm/probe beat signal: span 2 MHz	38
2.5	Spectrum analyzer trace of 1560 nm/probe beat signal: span 100 MHz	38
2.6	Diagram of repump spectroscopy	40
2.7	Diagram of probe beam/absorption imaging lens setup.	42
2.8	Schematic of vacuum chamber	44
2.9	The 2D-MOT in action	45
2.10	Photograph of the vacuum chamber and in-vacuum lenses prior to assembly	49
2.11	Photograph of the assembled vacuum chamber	50
2.12	Results of Gaussian-beam propagation code	56
2.13	Calibration curve for the germanium acousto-optic modulator	57
3.1	The single-beam dipole trap potential	60
3.2	Images of the trap-loading process	63
3.3	Calibrating the length scale of absorption images using gravity	72
3.4	Nonlinear fitting of thermal clouds; original imaging system	73
3.5	Nonlinear fitting of thermal clouds; vibration-stabilized imaging	74
3.6	<i>In situ</i> images of the optical trap, in and out of focus.	74
3.7	Sample trap-frequency resonance curves	77

3.8	Trap frequency scaling vs. power	77
3.9	Demonstration of free evaporation, in number and temperature	80
3.10	Sample evaporative paths	81
3.11	Gravity correction for trap depth	84
3.12	Approaching condensation I	86
3.13	Approaching condensation II	87
3.14	Our first BEC	88
3.15	The spinor condensate	89
3.16	The pure $m_F = 0$ condensate	90
3.17	The ‘supported’ $m_F = +1$ condensate	91
3.18	Formation of the ‘supported’ $m_F = +1$ condensate	92
3.19	Downward-directed atom laser I	94
3.20	Downward-directed atom laser II	95
4.1	Spin-spin energy diagram	97
4.2	Sample adiabatic compression paths	100
4.3	Images of spin mixing as driven by adiabatic compression.	100
4.4	Relative spin population vs. time, for several compression powers	101
4.5	Measured spin-mixing rate vs. density	102
4.6	Proposed scheme for novel atom laser	106
4.7	A typical outcoupling run of the dual-beam atom laser.	107
4.8	Several other varieties of the dual-beam atom laser	108
4.9	Modelling outcoupling and mean-field expansion	111
4.10	The motion of $m_F = \pm 1$ condensates in the outcoupling potential	112
A.1	^{87}Rb D_2 energy levels	118
B.1	Offset lock circuit diagram	120
C.1	Photographs of the LVIS setup, ca. 2002.	121
D.1	Photograph of the doubling setup	127

List of Tables

2.1 Relevant frequencies for resonant-light spectroscopy 39

Preface

Mr. BOYLE mentioned, that he had been informed that the much drinking of coffee produced the palsy... Mr. GRAUNT affirmed, that he knew two gentlemen, great drinkers of coffee; very paralytical.

THE HISTORY OF THE ROYAL SOCIETY OF LONDON
FOR IMPROVING OF NATURAL KNOWLEDGE
18 January 1664.

I JOINED THE QUANTUM SCIENCES & TECHNOLOGY LABORATORY in the spring of 2001 under immediate direction to join forces with Rob Thompson and build a BEC as part of research related to NASA's Condensate Laboratory Aboard Space Station (CLASS) project, a proposal within the LCAP (Laser Cooling and Atomic Physics) framework for science aboard the International Space Station. I was immediately put to work manning the existing laser-cooling apparatus, which at the time was a pyramidal LVIS set up for both rubidium and cesium. My first project (working with Rob and Dave Aveline, then a summer intern) was to build a dual-species MOT and see where that would lead. The idea at the time for the long run was the construction of a magnetic trap to integrate with that apparatus and work toward a standard magnetic-trap BEC.

The appearance in June 2001 of all-optical BEC at Georgia Tech stimulated an immediate discussion as to the destination of the BEC project. The apparent ease with which condensation was achieved in a system previously thought of as a dead end was too promising to ignore, and we launched a dipole trap effort beginning with the purchase of a 50 W CO₂ laser late in 2001. The early work on this mostly

involved researching ZnSe optical solutions and devising a way of mounting the lenses intravacuum.

Before ramping up optical trapping efforts, I made a set of dual-species collision observations in mid-2002, looking at the loss dynamics of co-located rubidium and cesium MOTs. A conference debut soon followed, with me presenting the resulting measurement of the inelastic Rb-Cs collision rate at DAMOP in Williamsburg. Initially we intended to use the pyramidal LVIS (the geometry of which drew far more interest at DAMOP than the collision measurements) as the source of atoms for a UHV MOT, which would load the dipole trap. This was not to be, as the first lab disaster of my tenure (along with an aftershock or two) rendered the venerable ‘MOTzilla’ unusable. The quantum gravity gradiometer group next door had experienced successful loading with a cesium 2D-MOT, leading us to settle on a similar arrangement for our cold atom source. Using a cuvette joined to glass-to-metal seals by the always-impressive work of the Caltech chemistry department’s glassblower Rich Gerhart, we loaded a UHV MOT using a 2D-MOT cold atomic beam in the fall of 2002.

We moved into a shiny new lab essentially once the calendar year 2003 arrived. I personally date all progress on the BEC experiment from January 2003—not entirely accurately, as I had looked for signs of optical trapping with the setup in the fall of 2002, as well as doing significant design work, but that time was more notable for finishing up the dual-species work and thinking about CO₂-laser safety issues than for any attempts at BEC. Interestingly, we were in a race for all-optical BEC that had apparently started in earnest in June 2001, when the Georgia Tech report came out. Rumors of the difficulty of duplicating the impressive effort were beginning to filter out into the community, rumors that I’m thankful weren’t forceful enough to keep me from persisting.

While the Ti:sapphire laser had performed well in the service of the experiments so far, it was by this point becoming increasingly irritable, and requiring a greater and greater fraction of my working day to keep happy. It was thus an absolute delight

when a novel laser system we had developed proved to be not only operationally satisfactory for laser cooling applications, but rock-steady in terms of intensity and frequency performance as well. It was initially built using a distributed feedback (DFB) laser as a seed for the 5 W EDFA, but was switched to a Vortex after initial proof-of-principle experiments and was fully incorporated into the optical trapping experiment by summer 2003.

The spring of 2003 saw successful alignment of the CO₂ laser through the germanium acousto-optic modulator, the external telescope, and the vacuum system in a crossed-beam configuration, construction and optimization of an ⁸⁷Rb UHV MOT, and the construction of anticipated loading-phase timing. Our first optical trap (using a detuned dark SPOT loading scheme) was observed using simple fluorescence in July 2003. That summer saw the installation of absorption imaging capability and the first attempts at placing the two separate dipole traps on top of one another. This was more difficult than we had anticipated, not to mention particularly tedious. In retrospect we were closer than I had imagined to good overlap, as the central region probably needed some free evaporation time to become strongly populated. Nevertheless, this obstacle and the appearance of the first post-Georgia Tech all-optical condensate (Tübingen) in December 2003, itself done with a single beam, convinced us to switch to a single-beam apparatus.

The switch combined with proper focusing of the absorption imaging system marks the point where I feel things became much more intense in terms of our approach to all-optical BEC. I began seriously thinking about temperature measurements around then, beginning with the first evaporative cooling in January 2004. By the spring I realized that estimates of trap frequency and density based on Gaussian-beam estimates of w_0 , the trap waist, were probably inaccurate, and I started measuring the trap frequencies using parametric resonance methods. These were particularly satisfying in their simplicity as well as the way they immediately revealed whether an adjustment of the external CO₂ laser telescope resulted in a tighter trap or not. By the spring of 2004 I had managed to get the trap as tight as possible with the given

aperture to the vacuum system, and shifted focus to trap loading. The possibility was discussed around this time that a larger-volume trap might be more efficient at loading while a tighter one would be better at evaporation. Some thought was put towards a dynamic trap but eventually shelved—ironically, this was a solution that was later documented to be quite effective.

The spring and summer were particularly devoted to frequency control. We knew that a small difference in initial number would make a large difference in any attempt to obtain BEC, and the one obvious ‘leak’ in our loading process was that we did not detune particularly far compared to what had been documented to be ideal. We thus switched away from a saturated absorption-based locking and jumping scheme and instead offset-locked the doubled 1560 nm laser to a reference laser, which conveniently was already built and had some power to spare: the nearby probe laser. Seemingly arbitrary frequency jumps could then be made through control of the offset lock’s reference frequency.

A major breakthrough in evaporative cooling was made in August 2004. We had previously been using an embarrassingly cumbersome system of optical shutters to switch the intensity of the repump beam, and finally got around to replacing it with a proper AOM-based intensity control system. The resulting re-tweaking of the trap-loading process combined with more aggressive evaporation illuminated an important problem: the putative zero-intensity level of the AOM was still significant enough to heat the atoms, as the repump laser was exactly on resonance with the $F = 1$ atoms. Careful arrangement of shutter timing on top of AOM intensity control (and reduction of the zero level of the rf amplifier involved) resulted in typical low temperatures observed dropping from ~ 600 nK to ~ 300 nK.

November 2004 found us increasingly perplexed by the apparent stalling at phase-space densities a factor of two away from BEC. Our custom evaporative paths were working and all heating problems had been eliminated, but the trap loading was still unsatisfactory and unrepeatable. My candidacy talk in late November was marked by a sense that things needed to change, and soon—while I was nervous given my ad-

vancement in grad-school years I felt that we were very close to BEC, and that I would ‘dance with the girl who brought me.’ As a result changes were made that led to a sense in the months afterward that either BEC was imminent or something was maliciously wrong with our trap characterization. In what was a major disappointment initially, I discovered the cause of the asymmetry in some of our ballistically expanded absorption images: imperfect turnoff of the CO₂ laser at the end of a run, resulting in distorted clouds. Modeling this turnoff using various Monte Carlo approaches confirmed the problem, including the fact that this distortion resulted in much higher temperature measurements. Fixing the turnoff problem was relatively easy, and while it indeed resulted in higher temperature measurements, it corrected misguided notions I had developed about particular evaporative paths and their efficiency. In our most drastic change, December found us switching to a 6-beam free-space MOT, and in January 2005 we bit the bullet and went to a fiber-coupled arrangement. MOT stability, MOT quality, and trap-loading repeatability all noticeably increased as a result.

Our first BEC signal was observed on the afternoon of February 17th, 2005. In retrospect, we probably reached criticality some days before; I particularly remember showing a visitor (Kris Helmerson) some promising absorption images that I would recognize now as being most likely partially condensed. The biggest helping factors toward obtaining the first signal were the care taken in calibrating the new rf amplifier that replaced its dead partner, whose intensity calibration was most likely out of date, the cleaner MOT setup offered by the 6-beam fiber MOT, and, amusingly, the water-cooling of a CO₂-laser beam dump that was located directly underneath the main 780 nm trapping beam, which would become miraged quite significantly by the hand-burningly hot beam dump after around half an hour of running.

The joy of this achievement (and the few initial experiments we were able to perform, including a first look at the spin distribution using Stern-Gerlach spectroscopy) was soon tempered by a lab disaster, namely the appearance of a strong leak in the vacuum system that shut down the ion pumps and ended up requiring several months

of baking, reconstruction, and more baking. The culprit was a window that appeared to have a crack in it that had been slowly growing for an unknown period of time. Needless to say, I felt quite lucky that this random bout of bad luck had seen fit to wait until *after* our first BEC, rather than before. In terms of the ‘race,’ our BEC (presented at conferences that summer) was one of the first post-2001 all-optical ^{87}Rb condensates; we joined Georgia Tech and Tübingen in the set of groups with condensates (succeeding around the same time as us were groups at Oklahoma State and Penn State).

The eight months following the rebirth of our condensate in June 2005 was a buzzing and active experimental period for us. In a major improvement to our condensate observation process, I moved our absorption setup around such that the camera was much less vulnerable to vibration, which was causing significant shifts in the observed absorption beam on a 10 ms timescale. Since we had improved diagnostics on a repeatable condensate, the question now rather luxuriously turned to what particular experimental ideas we wanted to implement.

We had become intrigued by the third kind of condensate on our palette—the supported $m_F = +1$ condensate, and the downward-directed atom laser generated by carefully removing the support. Clearly this phenomenon had something to do with the strongly distorting effect of gravity on our near-critical trap, so we spent a considerable amount of time exploring ways to levitate our atoms against gravity. In a smaller vacuum system this gradient (31.7 G/cm) would have been trivial, but in ours it was a significant challenge. A solution using ferromagnetic-core coils was investigated and eventually discarded as being too cumbersome, and eventually I settled on the installation of twin water-cooled anti-Helmholtz coils driven by a 300A–20V DC power supply. Needless to say it was a somewhat intimidating solution, but certainly fun to use. The supporting coils performed adequately; this avenue of investigation was postponed, though, as the spinor dynamics results were beginning to look promising.

Spin mixing had been observed in a similar condensate, so as a check that every-

thing was working well we had aimed to duplicate that observation using the $m_F = 0$ condensate I had been able to generate using a tweaked version of the MOT gradient during evaporative cooling. Frustratingly, even given long hold times we initially observed no mixing. We immediately realized that there were two culprits—high magnetic field and low condensate density. Jumping our bucking coils (which had been set for a relatively high field aimed at optimizing trap loading) to new values and calibrating the magnetic field using a simple rf spectroscopy technique was necessary but not sufficient to overcome the energy barrier to spinor dynamics. To access that realm required increased condensate density; increased number was not an option at this point, so I implemented an adiabatic compression scheme. This worked quite nicely, and I was able to demonstrate (through the winter 2005/2006) spin mixing at several compression levels and hold times, resulting in an order-of-magnitude measurement of the spin-spin energy c_2 , confirming indirect scattering-length measurements and spin oscillation measurements elsewhere.

Around this point we realized that outcoupling these coherently produced subpopulations was an interesting idea, and I set about trying to see if it were possible. I found some key theory papers from early on in the spinor game that had discussed this in the framework of the creation of massively entangled states as well as squeezing in the outcoupled beams. Through January and February I worked at getting the system running well enough to a) drive spin mixing with regularity and b) outcouple the mixed sublevels with regularity. Eventually we were able to do this, with the caveat that the atoms didn't go exactly where we wanted them to go—one of the populations preferred to reverse its initial direction, pass back through the $m_F = 0$ state in the center of the trap, and go out the other side of the trap. This was due to some odd velocity kicks introduced in the system, which we are currently looking at in more detail. Given that the next obvious step—proving the correlated nature of the outcoupled beams—was going to require some major changes to the experiment, the time seemed just about right to take a water break and graduate.

Currently the experiment is primed for a modification of several key aspects, all

of which will be discussed in the upcoming chapters. The journey from empty lab to a borderline turnkey BEC setup has been a long one and an admitted roller coaster. Nevertheless, the work has paid off, and the next generation of the experiment is in sight. The papers listed below are all from my time as a graduate student; we have plans for a longer paper based on the spinor work as well as one detailing the next doubled-fiber-laser 780 nm system.

Publications based on graduate work

- N. Lundblad, R. J. Thompson, D. C. Aveline, and L. Maleki, “Spinor dynamics-driven formation of a dual-beam atom laser,” submitted (2006).
- N. Lundblad, D. C. Aveline, R. J. Thompson, J. M. Kohel, J. Ramirez-Serrano, W. M. Klipstein, D. G. Enzer, N. Yu, and L. Maleki, “Two-species cold atomic beam,” *J. Opt. Soc. Am. B* **21** (2004) 3–6.
- R. J. Thompson, M. Tu, D. C. Aveline, N. Lundblad, and L. Maleki, “High power single frequency 780nm laser source generated from frequency doubling of a seeded fiber amplifier in a cascade of PPLN crystals,” *Optics Express* **11** (2003) 1709–1713.

Chapter 1

Background

Ludwig Boltzmann, who spent much of his life studying statistical mechanics, died in 1906, by his own hand. Paul Ehrenfest, carrying on the work, died similarly in 1933. Now it is our turn to study statistical mechanics.

DAVID L. GOODSTEIN
States of Matter.

BOSE-EINSTEIN CONDENSATION of dilute atomic vapors as a field seemingly appeared fully formed from the brows of several trailblazing groups. These definitive 1995 experiments were at JILA (led by Eric Cornell and Carl Wieman) and at MIT (in Wolfgang Ketterle's group) [1,2]; a third group at Rice presented tantalizing results that same year that were later confirmed [3–5]. The years following those initial experiments (in ^{87}Rb , ^{23}Na , and ^7Li , respectively) saw magnetic-trap BEC achieved in ^{85}Rb , hydrogen, potassium, and metastable helium [6–10], with the technology developing to the point where undergraduate colleges had operating condensates [11]. In a groundbreaking experiment, the first all-optical condensate was achieved in 2001 (using ^{87}Rb) at Georgia Tech [12]; other all-optical condensates in ^{87}Rb followed somewhat more arduously at Tübingen [13], at Penn State [14], here at Caltech–JPL [15], at Oklahoma State [16], and at Williams College [17]. All-optical condensation of cesium was seen in 2003 at Innsbruck [18] and of ytterbium (also in 2003) at Kyoto [19]. Hybrid magnetic/optical traps have become common in ^{87}Rb

condensate experiments [20, 21]; using such a hybrid, chromium was added to the ranks of condensed atoms in 2005 [22]. In addition, all-optical traps have been the basis of degenerate Fermi gas research [23, 24].

The link from the original groundbreaking experiments to the work described here is a fascinating one. It is the goal of this chapter to provide a concise introduction to the subject matter of this thesis and to place the work in the context of the last ten years of BEC and, by association, the last nigh–thirty years of cooling and trapping.

1.1 Bose-Einstein condensation

In 1925 Albert Einstein extended ideas put forth by Satyendra Nath Bose, who had been examining photon statistics and blackbody radiation; these insights resulted in our modern notion of Bose-Einstein statistics, despite the fact that this was before quantum mechanics had been significantly developed [25–27]. These notions were based on the simple analogy between the photons of blackbody radiation and matter, representing the first application of de Broglie’s novel hypothesis. They even predated the relationship between what would be called spin and statistical behavior, a relationship that soon emerged, separating all matter into fermions and bosons. Most importantly, Einstein realized that a consequence of the statistics that he had developed was a strange saturation of the lowest energy state even while the temperature T remained finite: “I maintain that, in this case, a number of molecules steadily growing with increasing density goes over in the first quantum state (which has zero kinetic energy) while the remaining molecules separate themselves according to the parameter $\lambda = 1$... A separation is effected; one part *condenses*, the rest remains a *saturated ideal gas*.”² [27].

The Bose-Einstein distribution, describing the occupation of energy states in a

¹ λ is the fugacity; Einstein uses it as e^{-A} where A is the chemical potential.

²“Ich behaupte, daß in diesem Falle eine mit der Gesamtdichte stets wachsende Zahl von Molekülen in den I. Quantenzustand (Zustand ohne kinetische Energie) übergeht, während die übrigen Moleküle sich gemäß dem Parameterwert $\lambda = 1$ verteilen... Es tritt eine Scheidung ein; ein Teil *kondensiert*, der Rest bleibt ein *gesättigtes ideales Gas*.” [27]

system of N indistinguishable particles of integer spin, is derived in any number of modern thermodynamics texts [28] from basic notions of statistical mechanics and is typically expressed as the average number of particles n_i in a state of energy ϵ_i :

$$n_i = \frac{1}{e^{(\epsilon_i - \mu)/k_B T} - 1} \quad (1.1.1)$$

where μ (the chemical potential) is fixed by number conservation, viz. $N = \sum_i n_i$. As aptly described elsewhere [29], this is simply the most random way to distribute a fixed amount of energy among N bosons with a given set of available energies. It is a standard derivation to show that for an ideal gas there exists a critical temperature T_c below which the lowest energy state becomes macroscopically occupied, with the condensate fraction increasing from zero as the temperature is lowered further. The phase transition for the ideal gas in free space is identified by the following relation:

$$\rho = n\lambda_{dB}^3 = n(2\pi mk_B T)^{-3/2} = \zeta(3/2) \sim 2.612 \quad (1.1.2)$$

With some effort, the same physics is demonstrated with the ideal gas confined to a harmonic trap of secular frequencies $\omega_{i=x,y,z}$ in which case criticality is denoted by:

$$\rho = N \left(\frac{\hbar\bar{\omega}}{k_B T} \right)^3 = \zeta(3) \sim 1.202 \quad (1.1.3)$$

The chemical potential μ as set by number conservation is large and negative at high temperatures; the condition for condensation then becomes that $\mu \rightarrow 0_-$ (or whatever minimum energy state is available) for some temperature T at which the minimum energy state becomes macroscopically occupied [30]. The fraction of atoms in the condensate grows as the temperature is lowered further:

$$\frac{N_0}{N} = 1 - \left(\frac{T}{T_c} \right)^\alpha \quad (1.1.4)$$

where $\alpha = 3/2$ for the unconfined ideal gas and $\alpha = 3$ for the harmonically confined

gas.

The resulting object—a macroscopic manifestation of the wavefunction itself in a truly dilute system, directly showcasing the nature of quantum statistics— is a remarkable tool for the exploration of quantum mechanics, low-temperature atomic physics, and many-body physics in general.

1.1.1 Evaporative cooling

The great breakthrough in the cooling and trapping of atoms that led to the first BEC was the technique of radiofrequency-induced evaporative cooling, first experimentally realized at MIT [31]. Evaporative cooling permitted for the first time access of subrecoil temperatures in a high-density atomic vapor; optical techniques existed to breach the recoil limit, but all were in some fashion connected to low-density requirements. In addition, magnetic trapping of hydrogen had been realized for some time, and evaporative cooling had been implemented simply by lowering the strength of the trap, but the process suffered from low densities and a collisional leak [32]. The ‘rf knife’ technique, however, allowed for constant trap depth during evaporation, resulting in rather spectacular increases in density during the evaporative process and the phenomenon of runaway evaporation. Evaporation in optical traps, in contrast, proceeds via lowering the depth and thus strength of the trap (as with early efforts in hydrogen magnetic traps) but with the compensatory advantage of high initial densities, as we shall see.

Successful evaporative cooling relies on continually removing the hottest fraction of atoms at such a rate that the gas continually rethermalizes and the hottest fraction is replenished. The process of evaporation is thus a battle between the so-called ‘good’ and ‘bad’ collisions—the former being the elastic collisions that redistribute energy in the trap and ensure thermalization, and the latter being the inelastic collisions that result in trap loss. The most common culprit for a bad collision is background vapor, although depending on the particular species and the densities involved, dipolar relaxation and three-body recombination can cause problems. The elastic collision

rate γ is determined by peak density and the interparticle scattering cross-section:

$$\gamma = n_0 \sigma \bar{v} / \sqrt{3\pi} \quad (1.1.5)$$

where $\bar{v} = \sqrt{\frac{3k_B T}{m}}$ and $\sigma = 8\pi a^2$, a being the s -wave scattering length, which is sufficient for a complete description of the dilute system at such a low energy. Collision rate is therefore one of the most important variables to consider in a condensate experiment—it determines the maximum speed at which efficient evaporation can occur and thus the timescale over which a condensate is created, the conventional wisdom being that it only takes ‘several’ collision times for a Maxwell-Boltzmann gas to rethermalize after an evaporative cut. The specific implementation of evaporative cooling in a single-beam dipole trap will be elucidated in §3.3.2.

1.1.2 The condensate wavefunction

We speak of a BEC as a macroscopic quantum object and characterize it as a gas wherein a significant fraction of atoms all occupy the same wavefunction—a giant matter wave. An ideal-gas BEC in a harmonic trap will simply be described, then, by a many-body wavefunction with all the atoms occupying the simple harmonic oscillator (SHO) ground state:

$$\psi(\mathbf{r}) = \frac{N}{\pi^{3/2}} \prod_{i=1}^3 \frac{1}{x_{i,0}} e^{-x_i^2/x_{i,0}^2} \quad (1.1.6)$$

where the $x_{i,0}$ are given by the oscillator lengths $\sqrt{\hbar/m\omega_i}$ and the density distribution is given by $n_c(\mathbf{r}) = |\psi(\mathbf{r})|^2$. However, this is useful solely as a tool of comparison to real condensates, which are dominated by internal interaction energy as described by the chemical potential μ and the scattering length a , which now plays a role even greater than its place as the pacesetter of evaporative cooling.

The notion of a macroscopic wavefunction remains useful, and we can modify the Schrödinger equation that led to Eq. 1.1.6 by incorporating a nonlinear term

proportional to the interaction energy and the density $n_c(\mathbf{r}, \mathbf{t}) = |\psi(\mathbf{r})|^2$:

$$i\hbar \frac{d\psi}{dt} = -\frac{\hbar^2}{2m} \nabla^2 \psi + U(\mathbf{r})\psi + \frac{4\pi\hbar^2}{m} a |\psi|^2 \psi \quad (1.1.7)$$

This is known as the Gross-Pitaevskii equation and can be more formally obtained from a field-theoretic standpoint [30, 33]. The ground-state solution to the GP equation is typically given as:

$$\psi(\mathbf{r}, t) = \psi(\mathbf{r}) e^{-i\mu t} \quad (1.1.8)$$

If we then create a time-independent version of the Gross-Pitaevskii equation and introduce the Thomas-Fermi approximation, whereby we neglect kinetic energy terms as being small compared to interaction energies, we find the following:

$$n_c(\mathbf{r}) = \max \left(\frac{\mu - U(\mathbf{r})}{\frac{4\pi\hbar^2}{m} a}, 0 \right) \quad (1.1.9)$$

The density distribution of the condensate in the Thomas-Fermi approximation is thus simply a mirror of the confining potential, and peak density of the condensate is related to the chemical potential as $n_{c,0} = \mu m / 4\pi\hbar^2 a$. More specifically the BEC density is given by:

$$n_c(\mathbf{r}) = n_{c,0} \max \left(1 - \sum_{i=1}^3 \frac{x_i^2}{R_i^2}, 0 \right) \quad (1.1.10)$$

Integrating this profile yields the following relation between Thomas-Fermi radii and density:

$$n_{c,0} = \frac{15}{8\pi} \frac{N_c}{R_x R_y R_z} \quad (1.1.11)$$

where the dimensions of the condensate R_i are determined by the interaction energy:

$$\mu = \frac{1}{2}m\omega_i^2 R_i^2 \quad (1.1.12)$$

Determining the chemical potential is a simple matter of exploiting the normalization condition, which gives:

$$\mu^{5/2} = \frac{15\hbar^2\sqrt{m}}{2^{5/2}}N_c\bar{\omega}^3 a \quad (1.1.13)$$

This can be conveniently rephrased [33] using the harmonic oscillator parameters:

$$\mu = \frac{\hbar\bar{\omega}_{ho}}{2} \left(\frac{15N_c a}{\bar{a}_{ho}} \right)^{2/5} \quad (1.1.14)$$

This phrasing particularly illuminates the condition of the Thomas–Fermi approximation, in which interaction dominates; here, the ground state energy is increased over that of the harmonic oscillator by the parameter Na/a_{ho} . It is precisely this condition ($Na/a_{ho,i} \gg 1$) that allows the neglecting of kinetic energy in the condensate and that should always be kept in mind when applying the Thomas-Fermi picture. It should also be clear that despite the high densities attained in this state, the gas remains truly dilute, in the sense that the interparticle interaction scale (the scattering length a) is only 5 nm, while even at maximum imaginable density in a condensate experiment (10^{15} cm^{-3}), the mean interparticle separation is $n^{-1/3} = 100 \text{ nm}$, and at more conventional mean densities in our trap of $5 \times 10^{13} \text{ cm}^{-3}$, the separation is more than 250 nm. The wavefunction that all the particles in condensate share is of course much larger than either of these values—it is cigar-shaped and typically a few μm by a few tens of μm .

1.1.3 Condensate expansion

The question of what happens to a condensate in a time-dependent potential is an illuminating one. When a formed condensate is released via a quick turnoff of the enclosing potential, the process by which stored mean-field (interaction) energy is converted to kinetic energy is revealed by a changing aspect ratio of the condensate. The famous experimental signature of this is the asymmetric expansion of a condensate; the tighter a condensate is held in any given dimension, the quicker the initial expansion rate in that direction is observed to be. This is of course totally different from a thermal gas, which maintains its aspect ratio once the cloud has reached spherical symmetry, since the ballistically expanded gas is a probe of the initial momentum distribution, which is itself symmetric (see §3.2.2). The development of this asymmetry is determined as follows, described in detail elsewhere [34]. Given a BEC in the Thomas-Fermi limit and time-dependent trap frequencies $\omega_i(t)$, the Gross-Pitaevskii equation will allow solutions that preserve the Thomas-Fermi parabolic profile but have time-dependent radii $R_i(t)$. These are parametrized as:

$$R_i(t) = R_i(0) b_i(t) = \sqrt{\frac{2\mu}{m\omega_i^2(t)}} b_i(t) \quad (1.1.15)$$

where $b_i(0) = 1$. A set of coupled differential equations describing the $b_i(t)$ are found:

$$\ddot{b}_i + \omega_i^2(t)b_i - \frac{\omega_i^2(0)}{b_i b_x b_y b_z} = 0 \quad (1.1.16)$$

Quick trap release frees the condensate from any confining potential, rendering the second term irrelevant; the resulting differential equations describe the expansion of a trapped gas. In particular, for a cigar-shaped trap we have two second-order equations for b_x and $b_r = b_y = b_z$:

$$\ddot{b}_r = 1/b_r^3 b_x \quad , \quad \ddot{b}_z = \kappa/b_r^2 b_x^2 \quad (1.1.17)$$

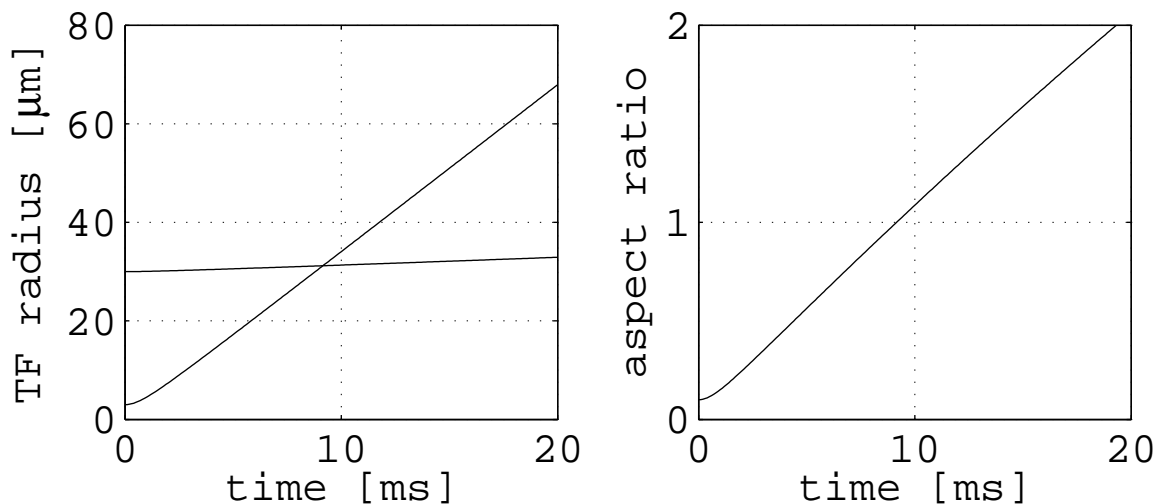


Figure 1.1: *The asymmetric expansion of the condensate, depicted on the left as the Thomas-Fermi radii R_x and R_{yz} as a function of time, and on the right as an aspect ratio R_{yz}/R_x . The dimensions used ($R_x(0) = 30 \mu\text{m}$ and $R_{yz}(0) = 3 \mu\text{m}$) are characteristic of our experiment. In particular note the perpetual increase in aspect ratio reflecting the preferred conversion of mean-field energy to kinetic energy along the initially tightly confining direction.*

where $\kappa = \omega_x/\omega_r$ and the time has been scaled to units of $\tau = \omega_r t$. A simple solution exists for a trap such as ours, where $\kappa \ll 1$:

$$b_r(t) = \sqrt{1 + \tau^2} \quad , \quad b_x(t) = 1 + \kappa^2(\tau \tan^{-1} \tau - \log \sqrt{1 + \tau^2}) \quad (1.1.18)$$

Clearly, the expansion along the tightly confined direction greatly outpaces that along x ; for all intents and purposes the latter remains constant. A typical situation is depicted in Fig. 1.1, showing an initial aspect ratio in the trap of $3 \mu\text{m}/30 \mu\text{m} = 0.1$ evolving to > 2 over the course of 20 ms.

1.2 Optical trapping

A longstanding goal of the early laser cooling and trapping community was the confinement of atoms not through the radiative (‘spontaneous’) force alone [35, 36] or with spatially varying Zeeman shifts (as in magneto-optical traps (MOTs) [37] and magnetic traps [38]), but via the dipole force, whereby atoms experience a potential

based on an induced electric dipole moment—i.e., traps based on the AC Stark shift or ‘light shift.’ The obvious advantage was that the scattering rate from such traps was quite low, in principle enabling very tight confinement for long times at temperatures that were potentially much lower than allowed by radiation-pressure methods. Our particular interest with respect to Bose-Einstein condensation is that the dipole trap has trap depths accessible to existing pre-cooling mechanisms (the MOT), has the ability to reach nK-level temperatures via evaporative cooling, and allows significantly tighter confinement than any spontaneous-force trap and most conventional magnetic traps, enabling (in principle) much faster evaporation. Another feature is the total spin independence of the the dipole-force trap, either in the realm of the far-off resonance trap (FORT) or the so-called quasi-electrostatic trap.

An atom interacting with a light field is described classically by its complex polarizability $\tilde{\alpha}$, the real part of which, $\Re(\tilde{\alpha}) \equiv \alpha$, is associated with conservative forces stemming from induced dipole moments, while the imaginary part $\Im(\tilde{\alpha})$ governs near-resonant absorption. As reviewed in detail elsewhere [39], the potential energy of an atom in a far-off resonant dipole trap is calculated beginning with the energy of a polarized object in an applied external electric field:

$$U(\mathbf{r}) = -\frac{1}{2}\langle \mathbf{p} \cdot \mathbf{E} \rangle = -\frac{1}{2}\alpha |\mathbf{E}(\mathbf{r})|^2 \quad (1.2.1)$$

This relates to the intensity of a laser field via the standard relation:

$$I(\mathbf{r}) = \epsilon_0 c |\mathbf{E}(\mathbf{r})|^2 \quad (1.2.2)$$

such that the potential energy is simply given by:

$$U(\mathbf{r}) = -\frac{\alpha}{2\epsilon_0 c} I(\mathbf{r}) \quad (1.2.3)$$

thus allowing the atom to be trapped at a local maximum of electromagnetic intensity, as long as the trapping laser is to the red of resonance. The real polarizability α of

the ^{87}Rb ground state is $5.39 \times 10^{39} \text{ C}\cdot\text{m}^2/\text{V}$, and that of the excited state $13.0 \times 10^{39} \text{ C}\cdot\text{m}^2/\text{V}$, the latter only relevant in that its value comparable (indeed, greater) than the former ensures that the trap-loading process (which occurs during the cycling between ground and excited states) does not have a fundamental leak.

Since we are interested in the domain of being far off resonance (in our case $\lambda_{\text{CO}_2}/\lambda_{\text{Rb}} \gg 1$), the phenomenon of heating from scattering becomes negligible. The scattering rate is given in the semiclassical Lorentz ansatz for electron motion by

$$\gamma_{sc} = \frac{2\Gamma}{\hbar\omega_0} \left(\frac{\lambda_0}{\lambda} \right)^3 U_0 \quad (1.2.4)$$

which for a CO_2 laser is very low: for a full-strength trap at 1 mK, $\gamma_{sc} = 1.8 \times 10^{-3} \text{ s}^{-1}$, or one photon every ten minutes.

The vanishingly small scattering rate ensures that the trap is truly conservative and can be used for evaporative cooling over timescales determined solely by collisional dynamics. Unfortunately, there exists no technique equivalent to the ‘rf knife’ approach utilized so well in concert with magnetic traps; instead, evaporative cooling must be implemented via the rampdown of laser intensity. This has the advantage of being experimentally very easy to implement, but has the unescapable drawback of the trap frequencies (and thus the atomic density) falling off with power, and the resulting impossibility of the blessing bestowed upon the magnetic trap community—so-called runaway evaporation. Nevertheless, the extremely high initial collision rates available in an all-optical setup can more than make up for the progressive weakening of the trap during evaporation, even allowing for condensation times significantly quicker than the best traditional magnetic trap BEC setups³.

³So-called chip traps, with the magnetic fields generated by in-vacuum microwires, have shown particularly fast condensation, also due to their high initial collision rate.

1.2.1 History

The first optical trap was realized in sodium in 1986 fulfilling a proposal made eight years earlier [40,41]; early traps were relatively close to resonance, and the first far-off resonance trap (FORT) was not made until 1993 [42]. In 1995 an attempt was made at evaporative cooling in a crossed 1.06 μm FORT [43]; this effort, while groundbreaking, was hampered by low atom number and density. The first quasi-electrostatic trap, or QUEST as it was dubbed by its creators, was established using cesium in 1995 [44,45]. Using a CO₂ laser for a dipole trap was presumably avoided previously due to the fact that the interaction strength was thought to be very small compared to lasers such as the Nd:YAG at 1.06 μm or FORTs detuned by hundreds of GHz; yet such high powers (tens of Watts easily) were available with standard CO₂ lasers that the idea was quickly adopted by several groups. In this first experiment, up to 10^6 cesium atoms were trapped (marking the introduction of improved loading techniques) and the low scattering rate of the QUEST was confirmed [45]. A CO₂ laser optical lattice with rubidium was reported in 1998 incorporating the new loading techniques and, significantly, showing how trap frequencies could easily be measured using parametric resonance [46,47]. Observations of evaporative cooling in a cesium trap were made in 2000 in an experiment perhaps more remarkable for the long (hundreds of seconds) storage times involved [48]. At the same time, work began using quasielectrostatic traps for fermionic species—a series of seminal experiments using ⁶Li were performed beginning in 1997 exploring heating limits, scaling laws, loading dynamics, and Fermi degeneracy [23,49–53]. The MIT group added a dipole trap to their setup around this time, transferring existing condensates into very shallow optical traps [54]. In 2001 all-optical Bose-Einstein condensation was achieved in ⁸⁷Rb at Georgia Tech [12]. This experiment used the geometry of the 1995 Stanford experiment and built on ideas developed in the QUEST work—nevertheless the work was rather surprising to the community, as atomic densities in the crossed-beam trap were reported as being higher than 10^{14} cm^{-3} . The promise of this initial work stimulated the bulk of the

work in this thesis. A second all-optical condensate in ^{87}Rb was finally reported in 2003, utilizing both crossed- and single-beam geometries [13, 55]. Other important experiments developing through this period include the first BECs of cesium and of ytterbium, both performed using an optical trap [18, 19, 56], and experiments focused on obtaining larger all-optical condensates [14] and on using them to explore many-body phenomena such as the Tonks-Girardeau gas [57].

1.3 Atom lasers

The connection between Bose-Einstein condensation and the laser is compelling. Qualitatively the same phenomenon is observed: a macroscopic fraction of quanta occupying the same spatial mode—in the case of a laser, photons in a particular optical cavity mode [58–60], and in the case of a BEC, atoms in the ground state of a harmonic trap. Even semantically the relation is powerful: the condensate is a particularly stark demonstration of the wave nature of matter, and as Einstein used deBroglie’s hypothesis to justify treating the statistics of certain atoms in the same fashion as that of photons, similarly, phenomena possible with light should thus be possible with properly prepared matter. The differences, of course, are significant; photon number is not conserved, leaving the system perpetually bound to a chemical potential of zero, and the system is not governed by the first-order time evolution of the Schrödinger equation⁴. Nevertheless, integrating the concept of an output coupler and some sort of ‘pump’ with established BEC techniques was a clear goal from early on in the field’s development, due to the allure of a monochromatic, intense, directional and preferably continuous source of coherent matter waves. The matter wave reservoir itself would be generated through a stimulated process, presumably based on the formation of the condensate itself out of the thermal cloud via bosonic stimulation.

⁴Interestingly, in the presence of a nonlinearity mediated by matter, such as the intensity-dependent refractive index (Kerr nonlinearity) of rubidium, laser photons can behave like an interacting Bose gas—the so-called photon fluid [61–63].

The first output coupler for Bose-Einstein condensates was implemented in one of the laboratories where BEC was first achieved. The MIT group in 1997 achieved two important milestones: they showed that condensates were truly matter-wave coherent [64], and they showed a pulsed output coupler [65]. The output coupler was based on pulsed radiofrequency transitions to coherent superpositions of the one trapped state and the two untrapped states. A well-collimated atom laser with a continuous-wave output coupler based on similar radiofrequency transitions was demonstrated by Bloch, Hänsch, and Esslinger in 1999, featuring beams up to 2 mm long of the expected spatial and spectral resolution— ‘brightness’ up to ten orders of magnitude higher than a thermal source such as a Zeeman slower [66]. A quasi-continuous laser using a Raman-transition outcoupler was demonstrated in 1999 at NIST [67]. Also worth noting is the all-optical atom laser demonstrated in concert with the 2001 Tübingen all-optical condensate [13].

Notions of what constitutes an atom laser are as varied as the experiments that have generated them, yet the full understanding of several issues seems necessary to avoid skeptical glances in the court of public opinion: the possibility of continuous operation, the notion of a ‘pump,’ or source of replenished coherent atoms to out-couple, and the nature of the output coupler itself. In §4 we hope to address these issues in detail as part of the experiments performed for this thesis, and the claims of a novel atom laser contained therein.

1.4 Spinor BEC

In 1998 the MIT group published observations of the first example of a spinor condensate, in which they transferred a spin-polarized ^{23}Na condensate created in a traditional magnetic trap into a dipole trap formed by the focus of a far-off-resonant laser [54]. Soon after, they observed the formation of spin domains resulting from

population exchange within the $F = 1$ manifold via the spin-relaxation collision:

$$m_0 + m_0 \rightleftharpoons m_{+1} + m_{-1} \quad (1.4.1)$$

which allowed redistribution of the spin population according to the constraints of the local magnetic field and the spin-spin Hamiltonian [68]. This population exchange could occur without trap loss as (unlike the magnetic trap that birthed the condensate) the dipole trap was spin-independent. Magnetization \mathcal{M} , or the difference in the two polarized populations, is preserved throughout this process simply via conservation of total spin. This study, and the papers that quickly followed it [69, 70], showed that spinor BEC (and multicomponent BEC in general, including the two-component BEC seen in [71]) provided exciting new opportunities to study many-body physics.

Seminal theoretical work, also in 1998, examined the nature of a spinor BEC [72, 73], many of the notions of which I will reproduce now for illumination. We begin with a system of bosons in an $F = 1$ hyperfine spin state, such as the lower hyperfine ground state of ^{87}Rb , and first seek to show what new Hamiltonian applies to the system now that the spin degree of freedom has been liberated. The polarized BEC system is well-known to be described by a single parameter—the scattering length a and the corresponding interparticle potential:

$$\hat{U}(\mathbf{r}) = \delta(\mathbf{r}) \frac{4\pi\hbar^2}{m} a \quad (1.4.2)$$

Taking a step back, we derive the new spinor potential, assuming only that the particles are all confined to the $F = 1$ manifold and that the energy scale is low enough such that pairwise δ -function interactions will suffice. The most general interaction is then the simple expression

$$U(\mathbf{r}) = \delta(\mathbf{r}) \sum_{f=0}^{2F} g_f \hat{P}_f \quad (1.4.3)$$

where \hat{P}_f projects the two colliding atoms into a total angular momentum state f , with an associated energy $g_f = 4\pi\hbar^2 a_f/m$. Symmetry forces only even terms of this sum to apply for bosonic species. Complementing this relation is the inner product of the two colliding spins:

$$\mathbf{F}_1 \cdot \mathbf{F}_2 = \sum_{f=0}^{2F} \lambda_f \hat{P}_f \quad (1.4.4)$$

where $\lambda_f \equiv \frac{1}{2}[f(f+1) - 2F(F+1)]$. Combining these relations with the closure condition $\sum_{f=0}^{2F} \hat{P}_f = 1$ yields the interaction Hamiltonian (dropping the δ -function):

$$\hat{U} = c_0 + c_2 \mathbf{F}_1 \cdot \mathbf{F}_2 \quad \left[c_0 = \frac{g_0 + 2g_2}{3}, \quad c_2 = \frac{g_2 - g_0}{3} \right] \quad (1.4.5)$$

This potential can be turned into a second-quantized Hamiltonian \mathcal{H} and then a variational-method free energy $K = \langle \mathcal{H} - \mu N \rangle$, which is to be minimized to find a ground state. In this scenario the condensate wavefunction is represented by a vectorial order parameter: $\Psi(\mathbf{r}) = \sqrt{n(\mathbf{r})} \boldsymbol{\zeta}(\mathbf{r})$, where $\boldsymbol{\zeta}$ is a normalized three-component vector⁵. The functional is as follows:

$$K = \int d\mathbf{r} \frac{\hbar^2}{2m} [(\nabla \sqrt{n})^2 + (\nabla \boldsymbol{\zeta})^2 n] - [\mu - U(\mathbf{r})]n + \frac{n^2}{2} (c_0 + c_2 \langle \mathbf{F} \rangle^2) \quad (1.4.6)$$

where $\langle \mathbf{F} \rangle^2 = \boldsymbol{\zeta}_a^* \boldsymbol{\zeta}_b^* \mathbf{F}_{\eta,ab} \mathbf{F}_{\eta,cd} \boldsymbol{\zeta}^c \boldsymbol{\zeta}^d$, and the \mathbf{F}_η are the spin-1 matrices ($\eta = x, y, z$). For $c_2 < 0$, the ‘ferromagnetic’ case, the energy is minimized by $\langle \mathbf{F} \rangle^2 = 1$; for $c_2 > 0$, the ‘antiferromagnetic’ or ‘polar’ case, the energy is minimized by $\langle \mathbf{F} \rangle = 0$. The exact nature of these ground states is not particularly meaningful nor accessible to the extremely low energy of the spin interaction, yet there is a crucial consequence of the sign of c_2 ; these issues will be discussed in the next section. A ^{87}Rb BEC in the $|F=1\rangle$ ground state is ferromagnetic according to extensive studies of its scattering properties [74, 75], namely that $c_2 = -3.58(57) \times 10^{-14} \text{ Hz cm}^3$. The MIT work

⁵ As introduced in these theory papers, we make the ‘single-mode approximation,’ that is, we treat the spatial profile of all spinor components as identical and time-independent.

showed conclusively, on the other hand, that the $F = 1$ ^{23}Na BEC was polar [68].

1.4.1 Spin mixing

Theoretical discussion of the phenomenon of spin mixing appeared in the late 1990s driven by the MIT spinor experiments and made several predictions, most notably the observation of oscillations in spin population [72, 73, 76, 77]. The spin-spin interaction energy $E/h = c_2 n$ is quite weak; at condensate densities of 10^{14} cm^{-3} , which are generous for our experiment but generally typical in the field, this energy is 3.6 Hz. For comparison, this corresponds to a first-order Zeeman shift of the $m_F = \pm 1$ levels of $\sim 5 \mu\text{G}$. This would seem to imply that any investigation of spinor dynamics would require a cumbersome magnetically shielded apparatus. Fortunately, this is not necessary. If we look at the spin-relaxation collision, Eq. 1.4.1, more closely, it is apparent that it has the capacity to reveal the spinor nature of the condensate even at significant laboratory background fields. To begin with, the linear Zeeman shift does not play a role in the equation; energy is conserved on either side of the collision. The quadratic Zeeman shift, however, causes a lower total energy if two atoms are in the $m_F = 0$ state versus being of opposite spin polarization. Secondly, the consequences of the functional K (Eq. 1.4.6) are that for $c_2 < 0$ the reaction is biased towards the right [68, 78]. The system will thus evolve driven by the interplay of spin-spin energy and the magnetic field; while population oscillations are predicted and the situation is more complicated than it might first appear, what is clear (and experimentally relevant) is that a state initially prepared as $m_F = 0$ is unstable, unless preserved by the quadratic Zeeman shift [77]. These dynamics were phrased particularly succinctly in a 2003 article by Zhang et al., building on past work [79] by discussing the spinor condensate in the context of a nonzero magnetic field whereby the conservation of \mathcal{M} as in Eq. 1.4.1 leads to more realistic ground states [80]. In particular, they predict a ground state distribution of spin states at zero field, given initial magnetization $\mathcal{M} = n_+ - n_-$ and total constraint $n_+ + n_- + n_0 = 1$, where n

here represents fractional population:

$$n_{\pm} = \frac{1}{4}(1 \pm \mathcal{M})^2 \quad n_0 = \frac{1}{2}(1 - \mathcal{M}^2) \quad (1.4.7)$$

and a solution at nonzero field parametrized by $\delta = (E_+ + E_- - 2E_0)/2$, essentially the quadratic Zeeman shift:

$$n_{\pm} = \frac{1}{2}(x_0 \pm \mathcal{M}) \quad n_0 = 1 - x_0 \geq \frac{1}{2}(1 - \mathcal{M}^2) \quad (1.4.8)$$

The parameter $x_0 = n_+ + n_-$ is found by minimizing $\mathcal{F} = g_+(x) + x\delta$, where $g_+ = c_2 n(1-x)(x + \sqrt{x^2 - \mathcal{M}^2})$. Thus for $\mathcal{M} = 0$, such as if a condensate were to be initially prepared totally in the $m_F = 0$ state, the ground state at zero field is $n_0 = 1/2$, $n_{\pm} = 1/4$. As fields increase, the ground state is biased more and more toward $m_F = 0$, and at a field strong enough such that δ matches the spin-spin energy, no evolution away from $m_F = 0$ occurs.

The first observation of spin mixing was in the $F = 1$ ground state of ^{87}Rb in an optical-lattice BEC at Georgia Tech [78]. Confirmation of this, and observations of spin mixing in the $F = 2$ state, soon followed in two other groups [20,21,81–83]. These observations confirmed the ferromagnetism of $F = 1$ condensate and the polar nature of the $F = 2$ condensate. The presumption of coherence in the spinor dynamics was confirmed in 2005 [84], with attendant theoretical discussion presented as well [85,86]. Spin mixing in an optical lattice with particularly clean observations of atom pairs confined to individual lattice sites was recently observed [87]. Our own observations of spin mixing will be presented in §4.

1.4.2 Entanglement and correlation

Since the inception of BEC as a relatively commonplace window into the quantum world, theorists have pushed to link it with the heart of the quantum/classical divide: multiparticle entanglement and the notions of quantum reality and measurement as-

sociated with it [88,89]. The accessibility of massively entangled atomic states would be of immediate interest to the quantum information and quantum optics communities. The properties of multicomponent Bose-Einstein condensates in particular are extremely suggestive of application to entanglement in that they represent a macroscopic source of pure and separable quantum states.

Many proposals have suggested the creation of entangled states in a BEC either through coherent collisional evolution of a bimodal BEC [90–93], or via interaction of tailored light with a condensate, either through lasers coupling intermediate states, or through the use of squeezed light [94–101].

Of particular interest to experimentalists developing spinor condensates were two proposals in 2000 discussing the creation of dual entangled beams via the spin mixing process in a spinor condensate [102,103]. Discussion of entanglement in spinor condensates unrelated to the specific dual-beam proposal can be found elsewhere [104,105]; in addition a similar scheme has been proposed involving the downconversion-like production of entangled beams from the dissociation of a molecular condensate [106].

In the dual-beam proposals a spinor condensate is envisioned to evolve via the spin-changing collision (Eq. 1.4.1) into an entangled and squeezed state, whereby correlations introduced into the evolved $m_F = \pm 1$ populations from an initial $m_F = 0$ condition ensure the entanglement and squeezing. This process has been compared to four-wave mixing [107,108], and indeed, an experiment creating correlated beams from four-wave mixing in a sodium BEC has been performed [109].

Both proposals suggest a simple experimental setup: an $F = 1$ condensate in a spin-independent trap. An initially prepared $m_F = 0$ condensate will evolve into some fraction of $m_F = \pm 1$, at which point a secondary potential will be employed on top of the main confining dipole trap. This secondary potential, perhaps another laser, will lower the energy of the $m_F = \pm 1$ states with respect to the initial condition. This energy shift, if large compared to the spin-spin energy, will render the spin-changing collisions irreversible, and the reaction products will gain kinetic energy after the collision. Conservation laws ensure that in such a setup the pair would be forced to

propagate in opposite directions, and in a strongly anisotropic cigar-shaped trap this would result in twin beams of outcoupled atoms. Entanglement would result from the fact that the pair was generated by a process in which one of the atoms had to be $m_F = +1$ and the other $m_F = -1$; the twin beams are therefore an EPR-correlated pair—the outcoupling process results only in opposite propagation, meaning that each side of the twin beam is in a superposition of the two states. In addition, the total spin of each side has to be zero due to the nature of the collision; thus, squeezing of the magnetization fluctuations $\delta\mathcal{M} = \delta(n_+ - n_-)$ is also predicted.

Chapter 2

Apparatus

The designer of a research apparatus must strike a balance between the makeshift and the permanent. Too little consideration of the expected performance of a machine may frustrate all attempts to get data. Too much time spent planning can also be an error. . . A new machine must be built before all the shortcomings in its design are apparent.

MOORE, DAVIS & COPLAN
Building Scientific Apparatus.

DESPITE THE RELATIVE SIMPLICITY of the experiment at the heart of this thesis—a dilute sample of atoms loaded into and evolving in a conservative potential, with all the technology fitting on a single optical table—the techniques brought to bear span the history of the cooling and trapping field and include several nontraditional approaches to traditional problems that will be documented in this chapter. Several significant changes were made to the experiment over the more than three years of its operation; where possible I will mention these changes, but the reader should assume that if not mentioned specifically, the apparatus described is the state of the system in the spring of 2006.

2.1 Resonant light

As an introductory note, our choice of element with which to attempt all-optical BEC was largely dictated by existing equipment and published experimental successes, namely the first all-optical condensate experiment [12]. The choice of a bosonic alkali metal was not a choice at all—we sought not to condense a new species, but rather to work with a novel variant of the by-now traditional magnetic-trap condensate. Our lasers at the time allowed a choice between rubidium and cesium; however, the latter was not an option due to a long history of failed attempts at condensation that discouraged any local attempt¹.

The workhorses of any laser-cooling experiment are the lasers themselves that provide resonant light—the requirements in our case are a considerable amount of locked narrowband light (usable power > 300 mW) near 780 nm for laser cooling, > 5 mW locked 6.8 GHz away for repumping, and at least 0.5 mW available at either of these frequencies for absorption probes. In addition, significant dynamic intensity and frequency control is needed for all the lasers.

For the laser-cooling experiments at JPL predating the author (as well as those non-BEC experiments the author participated in, detailed in Appendix C) the source of hundreds of mW of infrared light was the Coherent 899-21 Ti:Sapphire ring laser, pumped by a SpectraPhysics laser providing nominally 10 W of doubled YAG light at 532 nm. The use and care of this expensive system has surely been documented extensively elsewhere; regardless, soon after optical trapping became commonplace in our laboratory we switched to the novel 780 nm system detailed below, which was used for the remainder of the experimental work presented in this thesis².

¹Cesium was, however, condensed all-optically in 2003 [18]. Regarding sodium, which is also commonly used in BEC experiments and is especially convenient due to its small mass—it traditionally requires dye lasers at 589 nm, and given the embarrassment of riches our lab had in the near-infrared, the choice to remain there was obvious.

²This switch relegated the Ti:Sapphire system to doorstep status, metaphorically and (briefly) literally. It remains in place, fighting the fate of the long-mothballed Ar⁺ lasers dating from before the author's arrival.

2.1.1 The doubled 1560 nm system

The recent appearance of inexpensive high-power fiber amplifiers at the telecommunications wavelengths near 1560 nm was a serendipitous event from the point of view of the atomic physicist. These amplifiers (available up to > 10 W) combined with the availability of highly efficient frequency-doubling technology [110–112] allowed the construction of a novel source of narrowband 780 nm light, developed at JPL³ for use in the laser cooling of rubidium.

This apparatus exploits a clever arrangement devised in order to overcome some limits placed on doubling efficiency. The traditional expression for frequency doubling involves the intensity of a plane wave after propagating through a short crystal of length L :

$$I_{2\omega}(x, y, z = L) \propto \omega^2 L^2 I_{\omega}^2(x, y, 0) \quad (2.1.1)$$

Typically, however, the benefits of focusing the laser through a short crystal far outweigh that of sending an unfocused beam through progressively longer and more unwieldy crystals. The cost of focusing the beam is a reduction of the doubling's length dependence to linearity. The production of frequency-doubled light through a single doubling crystal is then specified in terms of the normalized conversion efficiency $\bar{\eta}$, such that:

$$P_{2\omega} = \bar{\eta} L P_{\omega}^2 \quad (2.1.2)$$

The specific value for η will of course depend on the internal physics of the crystal as well as the intensity profile of the focused laser; as might be intuited, the ideal profile is nearly that determined by so-called confocal focusing, where the length of the crystal L is matched to the confocal parameter—twice the Rayleigh range $\pi w_0^2/\lambda$. A clever way to recover the lost L^2 dependence is to place several short crystals in series,

³Described in a 2003 paper [113], reprinted as Appendix D; doubled light had been used previously to lock a 1560 nm laser using rubidium lines, but this only generated μ W-level powers at 780 nm [114].

effectively duplicating the condition of frequency doubling in an optical waveguide, hence the literature sobriquet of *lens waveguiding in a cascade of crystals* [115]. The doubled (scalar) field in such a cascade of crystals is given by superposition:

$$E_{2\omega} = \sum_{i=1}^N E_{2\omega,i} \quad (2.1.3)$$

Combined with Eq. 2.1.2, we obtain the doubled power output, given N identical crystals of length L:

$$P_{2\omega} = \left(\sum_{i=1}^N \sqrt{P_{2\omega,i}} \right)^2 = \bar{\eta} L N^2 P_{\omega}^2 \quad (2.1.4)$$

Thus, for a two-crystal cascade, one would expect a factor-of-four gain compared to operating with a single crystal, given ideal conditions and proper phase matching.

The seed for the Yb/Er-doped fiber amplifier (IPG Photonics) is an external-cavity diode laser (ECDL) in the Littman-Metcalf configuration (New Focus Vortex) providing 10 mW of narrowband light at 1560 nm. The Vortex is tunable over 50 GHz, has a linewidth of 300 kHz at 50 ms, and can be feedback-controlled using piezoelectric tuning of the external cavity as well as fast control of the diode laser current. The amplifier is internally pumped with 980 nm light and is turnkey-operable at output powers up to 5W of 1560 nm light of ostensibly similar spectral profile to that of the diode laser. This beam is confocally focused through a crystal of periodically poled lithium niobate (PPLN) as depicted in Fig. 2.1 (photographically in App. D). After the first crystal, the beam is recollimated and it then traverses an adjustable length before being confocally focused a second time through another crystal. The adjustable length serves to ensure that the 2ω light from the first crystal arrives at the second crystal in phase with the fundamental—a full wave retardation in air between 780 nm and 1560 nm being approximately 50 cm. Phase matching within the 5 cm long crystal is permitted by the periodic poling and is achieved using precision temperature control of the crystals themselves—the poling period used was 19 μm ,

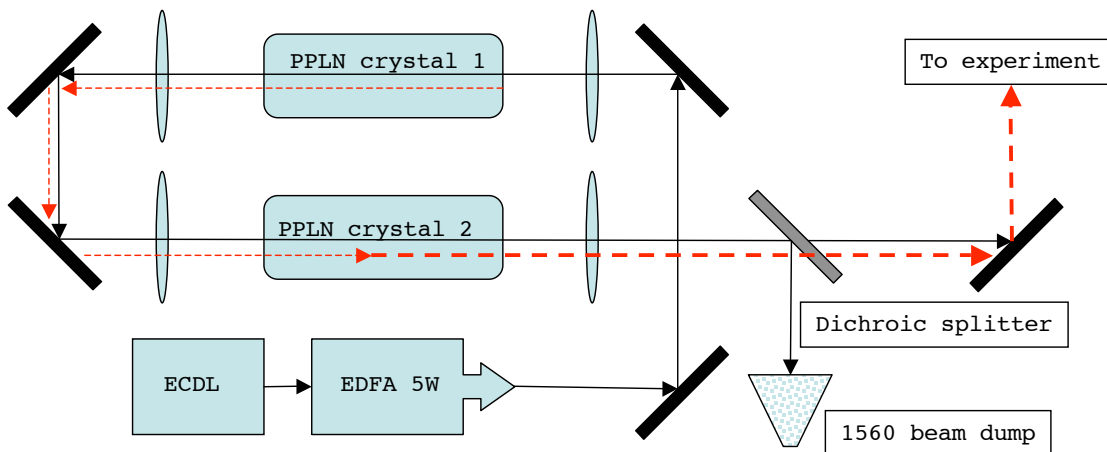


Figure 2.1: *Diagram of the doubled-1560 nm fiber amplifier system.*

which phase-matched at 100°C.

The two-crystal cascade when optimally aligned at full power yielded just lower than 1 W of 780 nm power in our best measurement. In an earlier measurement of the low power limit, the quadratic dependence on input power was observed, resulting in efficiencies of 4.6 mW/(W²·cm) in a denatured two-crystal configuration⁴, and 5.6 mW/(W²·cm) in the cascade. Ideally we would see a factor-of-two difference here, but several factors come into play that reduce the performance to a 20% bonus: most obviously, the insertion of loss of each crystal (4%) and the intra-cascade optical elements, but also spatial mismatch in the second crystal between the doubled beam and the fundamental due to imperfect focusing. Deviations from the simple quadratic formula of Eq. 2.1.2 are of course expected at higher power levels due to depletion of the source beam.

In terms of power generation capability, this setup is remarkable. It easily surpassed the previous source of infrared power in our laboratory, the Ti:Sapph, at less than half the cost, and seems to be astonishingly scaleable in terms of fiber-amplifier power and (with care) number of crystals. The utility of having an unused excess of 3 W of 1560 nm light available for use is also tantalizing, either for separate use with

⁴By which we mean a modified two-crystal cascade where light at 2ω is removed between the crystals using a dichroic beamsplitter in order to isolate the ‘seeding’ effect.

other crystals or for use as a far-off resonant dipole trap.

2.1.2 Offset locking the doubled 1560 nm laser

Given a small pickoff of the 780 nm output, it is possible to lock the system to the relevant transitions in ^{87}Rb using traditional saturated absorption spectroscopy techniques, as is done with the repump and probe lasers. However, the requirements of the experiment demanded a different approach. To load the dipole trap (as detailed in §3.1) a frequency jump of up to 150 MHz was required. The two traditional methods of doing this were inadequate: jumping the driving frequency of the double-passed acousto-optic modulator within a saturated-absorption lock was only practical up to jumps of 40 MHz or so, and placing an external AOM to control the frequency was too wasteful of power, given that a double-pass would be required to maintain alignment. A third path was sought and was found via simply jumping the reference frequency of an offset lock system, using the separately locked probe beam (detailed in §2.1.3) as a reference.

As depicted in Fig. 2.2, to create this lock we beat a sample of the doubled 1560 nm light with a sample of the locked probe beam on a high-speed (~ 1 GHz) photodetector. The difference between this beat signal and a second control signal was locked to a reference signal at 10 MHz. A circuit nominally designed as an offset lock (depicted in App. B) provided feedback to the 1560 nm ECDL piezo and diode current in order to maintain the proper relationship between the two frequencies. In practice, we operated the probe laser on resonance, and the doubled 1560 nm laser approximately -10 MHz off resonance, and then jumped the latter anywhere from -20 to -150 MHz off resonance in order to most optimally load atoms into the optical trap.

Figs. 2.3–2.5 depict spectrum-analyzer traces of the final beat signal between the probe beam and the doubled 1560 nm laser, centered around the input reference of 10 MHz. The main feature is around 4 kHz wide, with a central bandwidth-limited phase-locked peak 15 dBm higher. For a phase-locked circuit this is not particularly

impressive, corresponding to 5–10% of the beat signal power in the phase-locked loop, but since the circuit was only inserted out of desire for an offset lock, this was not a large disappointment. The most likely culprit for this is the fact that we are just applying feedback to the diode laser piezo and (slow) current input, and not modulating the ultrafast current input. For a laser cooling experiment this difference is a moot point. As a check on the linewidth of the system, the locked repump laser and locked trapping laser were beat against each other in order to examine the beat signal near 6.5 GHz. With healthy locks this beat signal was reliably found to be typically 1.5 MHz wide at -3 dB, implying $1.5/\sqrt{2}$ MHz for each laser, an adequate linewidth for laser cooling of rubidium ($\Gamma \sim 6$ MHz).

The actual process of getting the system to lock to the laser-cooling transition was somewhat convoluted, as hinted at by the multiple layers of mixing in Fig. 2.2. We began with a small amount of probe light, as shown exiting the top of Fig. 2.6. Some of this light, which was parked 111.8 MHz below the $|F = 2\rangle \rightarrow |F' = 3\rangle$ resonance, was sent to the experiment after being shifted to resonance; some of it was shifted to $+20$ MHz using the ‘beat assist’ AOM and directed onto a high-speed detector along with a small amount of doubled 1560 nm light in order to create a beat frequency between the two.

On the other side, we began with two VCOs; one fixed at 260 MHz and the other controlled such that it could jump on TTL command between 300 MHz and $300 + \Delta$ MHz. The output of this mixing is filtered, resulting in a signal at $40 + \Delta$ MHz. This signal is mixed with the RF beat signal coming from the high-speed detector. *This* output is filtered and amplified, and the resulting signal is held at 10 MHz through the feedback action of the lock circuit upon the master laser. Thus the whole locking scheme is predicated on the response of a feedback system on a 1560 nm master laser, with both an erbium-doped fiber amplifier and a doubling setup in between. Interestingly, for any given Δ there are four different possible lock points; for example, if the VCO signal is at 40 MHz ($\Delta = 0$), the beat signal will be held to either 50 or 30 MHz; given that the probe beam is parked at $+20$ MHz, this means the light going

to the experiment will be at +70, -30, +50, or -10 MHz. Similarly, if the VCO signal is at 200 MHz ($\Delta = 160$ MHz), the beat signal will be held to either 210 or 190 MHz; the trapping light will then be at +230, -190, +210, or -170 MHz. The first two of each foursome is not available to the lock due to the sign of the internal error signal in the lock. Thus for a given Δ there are two lock points, which is indeed what is observed: the correct one for laser cooling is chosen easily by scanning the piezo voltage (which easily resolves both locations) and looking for a MOT.

The remaining question was how the jump would work; when the LOs were jumped, the lock took the laser to the correct point (in the above example, $-10 \rightarrow -170$ MHz, which was sensible as it was closer than the other option, +230 MHz). This was only accomplished through a little help for the 1560 nm ECDL that was being fed back to. A feed-forward voltage assist was sent to the cavity piezo at the same time as the jump to prevent the control from hitting its rail, and during the jump the fast current control was disengaged, although this latter move was unnecessary. Thus, on a daily basis, to select the frequency one wished to sit at for laser cooling (-10 MHz in this example), one would adjust the 260 MHz VCO, and to adjust how far one would detune during the dipole trap loading process, one would adjust Δ and change the feed-forward voltage such that it matched Δ . Via this process we were able to demonstrate jumps up to 200 MHz away, after which the limiting factor was the bandwidth of the first mixer. The jump itself was shown to not be lossy for the MOT in the limit of very short detuning times, showing that any transients were not destructive.

2.1.3 Repump light, probe light, and absorptive imaging

The repump light used to ensure true cycling in the laser cooling process was provided by a New Focus Vortex ECDL providing approximately 14 mW of raw 780 nm power. It is locked to the $|F = 1\rangle \rightarrow |F' = 2\rangle$ transition using standard saturated absorption spectroscopy. Power is divided between the 2D-MOT and the UHV MOT, and travels to both MOTs via free space. Intensity control for the latter power is provided via

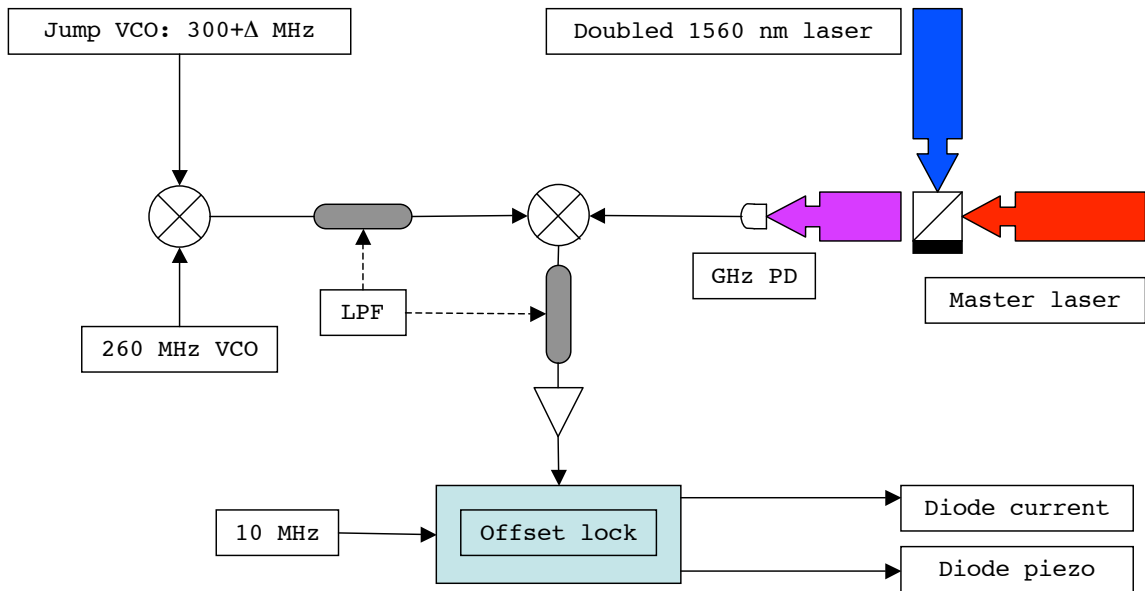


Figure 2.2: Diagram of the offset-locking setup for the doubled 1560 nm laser.

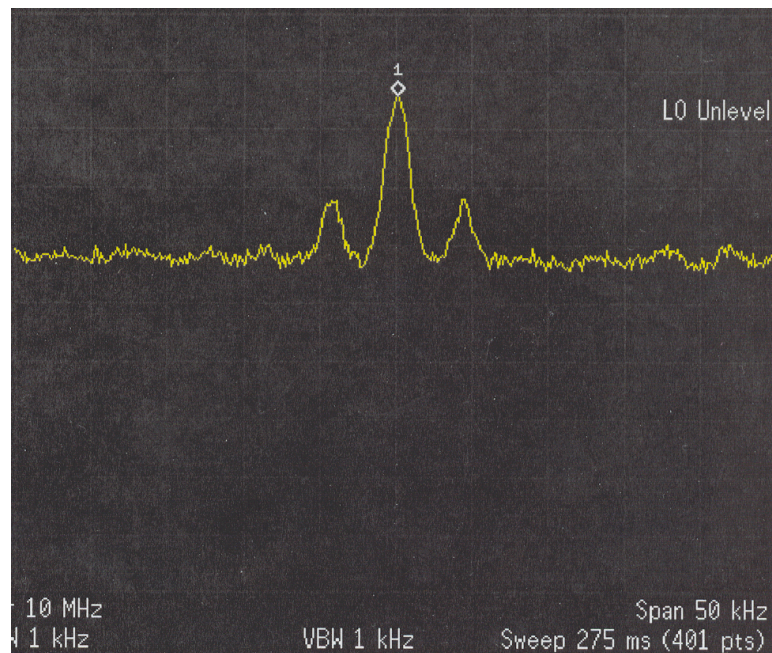


Figure 2.3: Spectrum analyzer trace showing offset lock beat signal; center frequency: 10 MHz, span: 50 kHz, vertical scale: 10 divisions of 6 dB each, bandwidth: 1kHz.

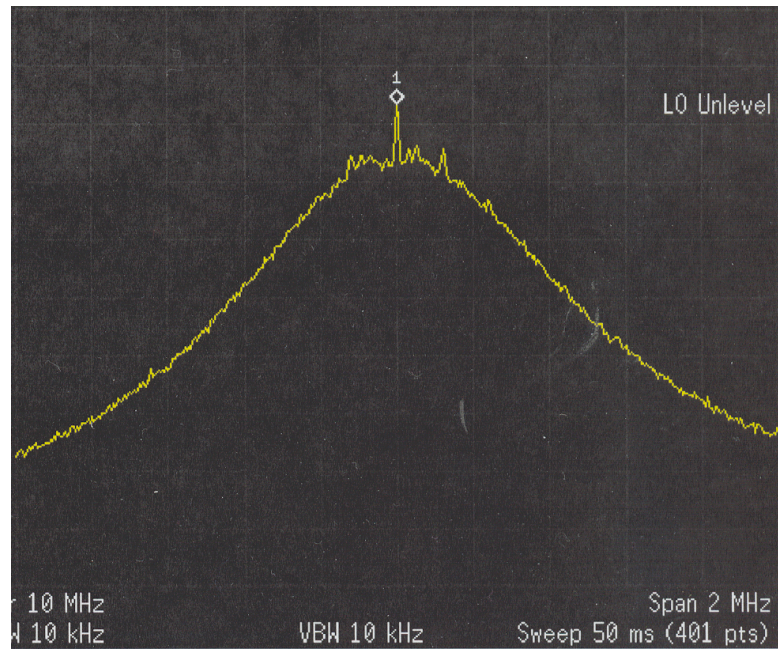


Figure 2.4: Spectrum analyzer trace showing offset lock beat signal; center frequency: 10 MHz, span: 2 MHz, vertical scale: 10 divisions of 6 dB each, bandwidth: 10kHz.

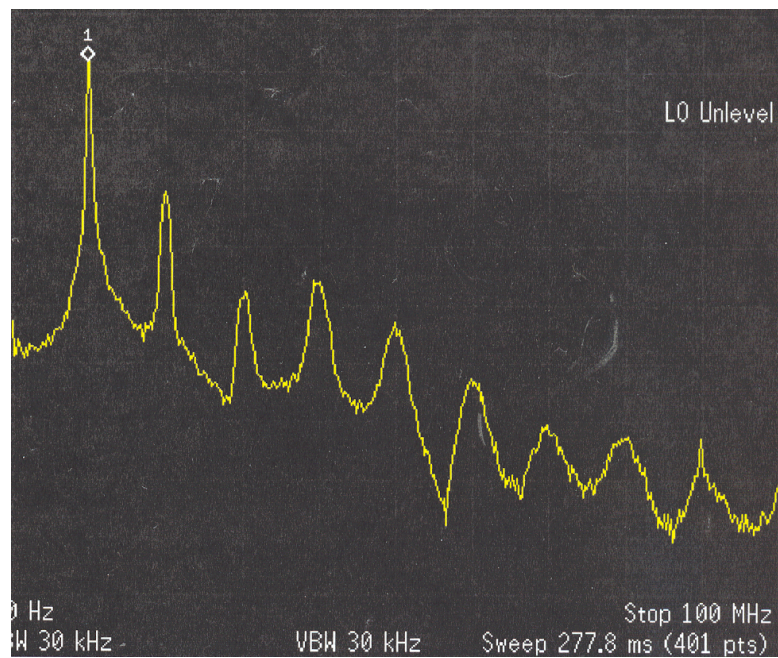


Figure 2.5: Spectrum analyzer trace showing offset lock beat signal; peak signal is at 10 MHz, span: 100 MHz, vertical scale: 10 divisions of 10 dB each, bandwidth: 30kHz.

Probe lock point (from $ F = 2\rangle \rightarrow F' = 3\rangle$)	-211.8
Probe saturated absorption	+100
Probe intensity control	+111.8
Beat signal assist	+131.8
Repump lock point (from $ F = 1\rangle \rightarrow F' = 2\rangle$)	0
Repump saturated absorption	+80
Repump intensity control	-80

Table 2.1: *Relevant frequencies for resonant-light spectroscopy, in MHz. The ‘saturated absorption’ values are frequencies sent to AOMs in double-pass configuration.*

an acousto-optic modulator; at full power the UHV MOT receives approximately 1 mW of power. The intensity control is mainly used for the creation of a ‘dark SPOT’ during dipole trap loading, whereby the repump intensity is drastically lowered to allow for much greater MOT densities, although it is also useful for precise optical pumping during the probing phase of the experiment. The AOM and a mechanical shutter isolate the dipole trap from what for most of the experiment is resonant light. Careful (ms) time control of the mechanical shutter was also necessary, as stray light in the diffracted order out of the AOM was sufficient to significantly heat ultracold clouds and obscure signs of degeneracy. A diagram of the repump locking setup is provided in Fig. 2.6.

The third 780 nm laser required for this experiment is for the absorption imaging of trapped atomic clouds. The probe process (detailed specifically in §3.2) involves illuminating a cloud of ^{87}Rb atoms with resonant light and recording how the probe is shadowed by the sample. As with the repump, this probe light originates with an ECDL (New Focus Vortex) that produces 10 mW maximum and is locked using saturated absorption spectroscopy, which conveniently provides a reference for the locking scheme described in §2.1.2. The locking apparatus is essentially identical to the saturated-absorption repump setup depicted in Fig. 2.6. The probe beam itself is intensity- and frequency-controlled using an AOM, and coupled into a single-mode fiber for convenience and mode quality. A mechanical shutter provides absolute

blocking when necessary.

The optics for probe beam use are depicted in Fig. 2.7. We begin with a beam emerging from the fiber, linearly polarized and collimated to approximately 5 mm in diameter, and significantly below the weakest ^{87}Rb saturation intensity ($0.2 \text{ mW/cm}^2 \ll 1.6 \text{ mW/cm}^2$). It is then passed through an entrance window to interact with the trap and then is passed out through a second window. Per Babinet's principle, the shadow cast by the trapped atoms is at the focus of a objective (light-gathering) lens, which collimates the 'shadow,' which is then imaged by a second lens onto a CCD array. This imaging of the plane of the dipole trap also allows for real-time fluorescence imaging of both the MOT and the dark SPOT process during dipole trap loading.

The lens positions were calibrated in a two-step process. First, the imaging lens was placed at the focal distance f from the CCD array by imaging a distant object. The objective lens was then mounted, at which point a ruler was imaged to establish a rough length scale. This crude process established a length per pixel, which is expected to be consistent within 10% with the known size of the CCD's pixels ($7.25 \mu\text{m}$) and the lens ratio of the telescope, which was one-to-one; using magnification would not likely have been fruitful given the resolution limit of around $5 \mu\text{m}$ set by the exit window and the imaging optics. Later on, gravity was used to more exactly calibrate the length scale of the absorption images. Once the rough calibration was performed, the objective lens was mounted on a translation stage near the vacuum chamber. The distance between the vacuum window and the objective was kept close enough such that the solid angle subtended by the objective lens from the trap was not significantly different from the solid angle subtended by the window. The distance between the objective and the imaging lens was kept to a minimum, although the current setup actually includes a large mirror redirecting the information-bearing probe beam between the objective and imaging lenses.

The CCD system used for the probe imaging (as well as the real-time MOT imaging) was a Kodak Motion Corder notable for its speed, namely the ability to

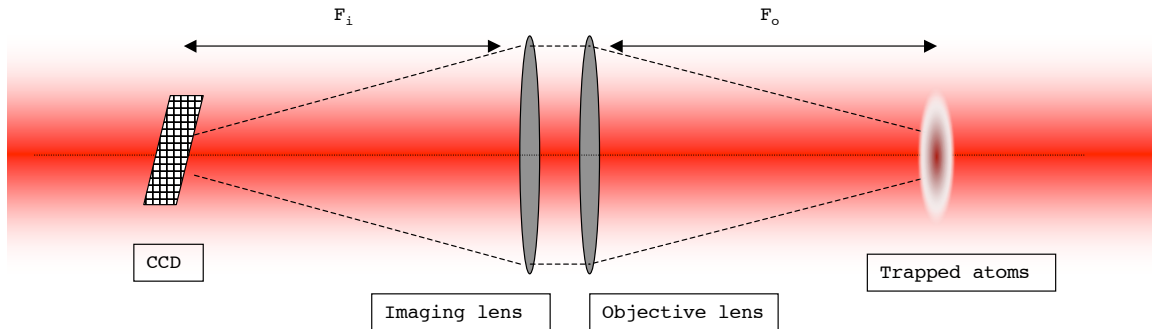


Figure 2.7: *Diagram of probe beam/absorption imaging lens setup.*

take 1/500 s exposures at near-100% duty cycle. With all resonant light shuttered no dark counts were observed in dark images taken using normal absorption timing; this was due less to particularly stringent light control, and more to the limited (8-bit) dynamic range of the camera.

2.2 Laser cooling setup

Much of our setup leading up to optical trapping involves workhorses of the laser cooling and trapping community, and features many standard techniques. Nevertheless, since this experiment was built from an empty room and has not been documented previously, we will do so in this section.

2.2.1 Vacuum

Cold atomic beam techniques developed in previous work [116] led us to appreciate the potential advantages in having an ultra-high vacuum science chamber in which to place our dipole trap. Overall background pressure could be much lower than in a vapor cell, allowing for much greater temporal tolerances in how we evaporatively cooled, as well as longer time to study and experiment with the condensate once it was created.

A schematic of our vacuum system is shown in Fig. 2.8. One side of the chamber is a rubidium vapor cell—a square glass cuvette attached via a glass-to-metal seal

to a six-way cross, itself connected to a small ion pump and a rubidium reservoir⁵. The cuvette is attached via glass-to-metal seal to a Kimball Physics spherical cube, pumped by a combination 300 l/s ion pump and titanium sublimation pump. The vapor cell and the spherical cube are separated by a 4" long copper tube (ID 4 mm) that provides considerable differential pumping⁶. Typical pressures achieved during the 2+ years of serious evaporative cooling efforts were 0.8–1.3×10⁻¹⁰ torr, as registered by an ion gauge near the central chamber. A major bottleneck in the experiment was significant pressure increases caused by the surface-mounted MOT coils, which typically dissipated 75 W in constant-current equilibrium and were usually quite hot. Pressures were observed to increase as high as 2×10⁻¹⁰ torr after sustained running, correlated with an attendant decrease in evaporative efficiency caused by a presumed higher background collision rate. Careful scheduling and cool-down periods, however, eliminated any real need for countermeasures.

2.2.2 The 2D-MOT and 3D-MOT

Several interesting cold atom sources arose out of the desire to provide a bright atomic beam for laser cooling, collision, and precision measurement applications that improved on the somewhat cumbersome Zeeman slower. The first so-called low-velocity intense source (LVIS) featured a standard vapor-cell MOT with a hole in one of the beams through which cold atoms would leak out unidirectionally [117]; versions developed at JPL and elsewhere featured a large pyramidal mirror combined with a retro-optic with a hole drilled in it to provide the ‘leak’ [116, 118–121]. The notion of two-dimensional cooling and trapping as an incubator for a cold atomic beam has existed in the form of ‘funnel’ setups as far back as 1990, leading into the development

⁵This ion pump was only necessary for bakeout; typically it shut down after several weeks post-bakeout running, due to being saturated by rubidium. After this point the faraway stronger ion pump (and the occasionally pulsed sublimation pump) took care of anything coming through from the vapor cell.

⁶In the summer 2005 vacuum reconstruction and bakeout we replaced the old 6" differential pumping tube with a new 4" version. No significant effect on MOT loading or UHV pressure was noticed.

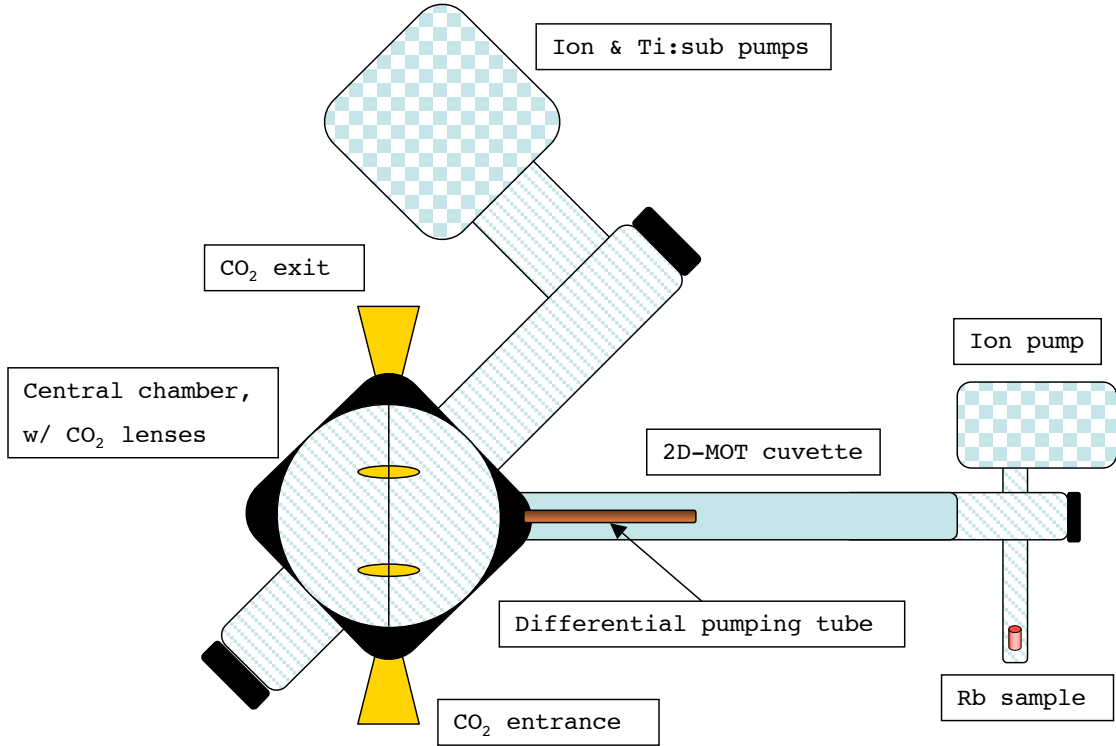


Figure 2.8: *Schematic of vacuum chamber.*

of the 2D-MOT as a viable and well-studied source of cold atoms [122–128].

Our 2D-MOT was formed by the intersection of two pairs of counterpropagating beams through the cross-sectionally square glass cuvette used as a vapor cell. Immediately adjacent to the cell were two coils forming an effective two-dimensional quadrupole field. The coils were simple loops of particularly high aspect ratio; more complicated ‘baseball’-style winding was deemed unnecessary if the coils were made long enough.

Both 2D- and 3D-MOTs rely on the laser-cooling transition: 780 nm light detuned to the red from the $|F = 2\rangle \rightarrow |F' = 3\rangle$ resonance. The 2D-MOT beams were expanded using telescopes to 2'' diameters; ideally (as suggested by [126, 128]) one wants the illuminated region of the cuvette to be as long as possible. Repump light for the 2D-MOT was combined with trapping light using polarizing beamsplitters. While it is true that the repump division was a finite-sum situation, with any increases in

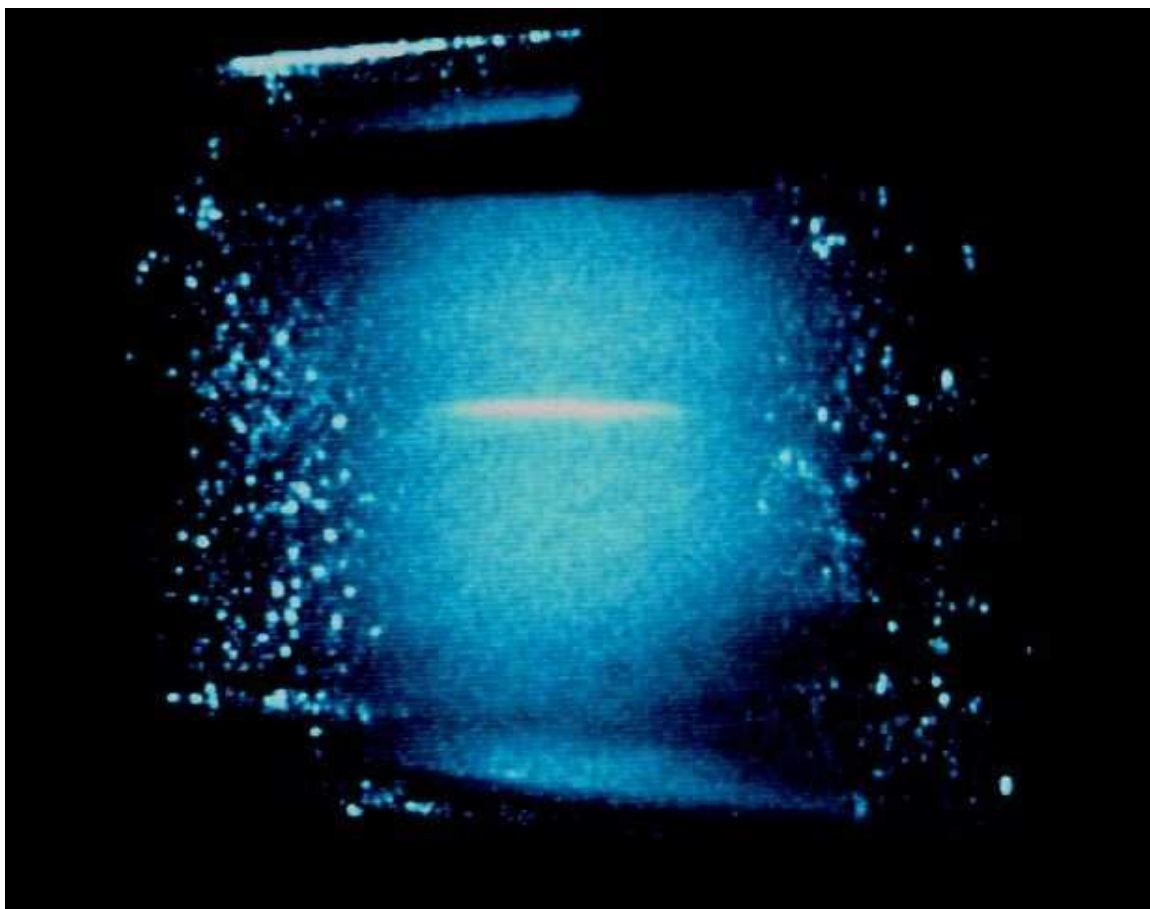


Figure 2.9: *The 2D-MOT in action*

repump intensity at the 2D-MOT resulting in corresponding losses for the 3D-MOT, it was observed that both MOTs were operating with sufficient repump light via small changes in light division as well as the negligible effect of the insertion of a OD=0.1 neutral density filter. An image of the 2D-MOT in operation is shown in Fig. 2.9. The characteristic cigar-shaped central fluorescence is immediately noticeable. The consequence of the two-dimensional cooling and trapping is a pair of cold atomic beams, one of which is directed downstream through the copper pipe into the UHV region. Transverse cooling in the beam is of course provided by the MOT action itself; beam velocity is kept low through a selection effect whereby only longitudinally slow atoms experience the cooling region long enough to be significantly affected.

The 3D-MOT is formed by six intersecting beams of specific polarization, as de-

scribed elsewhere [37, 129]. The beams originate from a nearby single-mode fiber, the coupling into which has typically been optimized such that the output power is 50–80 mW. Collimation is achieved such that clipping on 1" optics is not visibly wasteful. Repump light remains free-space, directed along two axes of the 3D-MOT at approximately $250 \mu\text{W}/\text{cm}^2$. Fluorescence from the trap was measured by a photodiode mounted outside one of the windows.

Our MOT coils were constructed of 200 turns of copper wire (each) and were arranged on the spherical cube in an approximation to anti-Helmholtz geometry. Typically 3–4 A was used for MOT loading, as well as for providing the necessary gradients for Stern-Gerlach spectroscopy of the condensate m_F distribution. We calculated that 4 A corresponded to a maximum gradient of 7 G/cm along the axis of the coils.

The laser detuning used was common to both 2D- and 3D-MOTS, which surely resulted in some inefficiency of trap loading. Optimal loading for a given alignment (as measured by frequency-corrected fluorescence from the trap) was typically found to be $\delta = -10$ MHz, or less than 2Γ ; most likely this provided optimal beam flux, but at some cost to the quality of the 3D-MOT, particularly at the high intensities used. The high intensities were necessary for good dipole trap loading, as detailed in §3.1.

Despite considerable time spent in alignment of the 2D-MOT, no general procedure was ever found that led convincingly to high-flux beams. The figure of merit, always, was maximum size of the 3D-MOT as measured relatively by the nearby photodiode and CCD camera. Most likely the largest timesink in the latter stages of this experiment was maintaining quality 3D-MOT loading; possible improvements will be suggested in §4.2.2. It was noticed, though, that an awareness of the need for care in the alignment of the front edge of the cooling region (so as to prevent strong deflection of the emerging cold atomic beam) was usually rewarded.

Periodic heating of the rubidium sample on the vapor-cell side of the chamber resulted in significant improvement of trap loading, at the temporary cost of higher

UHV pressure from straight-through atoms, observable by measurement of dark loading, whereby a small 3D-MOT formed even when no resonant light or field gradient were applied to the vapor cell region. Typically strong heating of the sample was only needed every few months; weak heating of the sample was more frequent but had inconsistent results and likely was more motivated by neurosis.

Approximate number calibration of the MOT was of the number resulting from fluorescence recorded by the CCD camera, which conveniently serves as a MOT monitor as well as the vehicle by which absorption images are recorded. This convenience stems from the fact that both procedures require lens placement such that the region at MOT center is imaged. The number of atoms is estimated via the ‘counts’ in any given image of the MOT, and is given by

$$N = \frac{8\pi}{\Gamma} \frac{1 + 4(\delta/\Gamma)^2 + 6I/I_s}{6I/I_s} \frac{N_{\text{counts}}}{t_{\text{exp}}\eta d\Omega} \quad (2.2.1)$$

where t_{exp} is the exposure time, η is the efficiency of the CCD in counts/photon, and $d\Omega$ is the solid angle subtended by the light-gathering optics. A convenient check on the MOT number calibration was made through the use of a photodiode placed near a vacuum window; the reading from this photodiode provided realtime (if relative) feedback on MOT number, whereas the CCD images were most often used to monitor MOT shape and stability.

Loading of the MOT typically followed the standard loading form $N(t) \propto 1 - e^{-t/\tau}$, and the decay of the MOT was shown even at high intensities to have a $1/e$ lifetime of 20–30 seconds. The lifetime of a large MOT in a high-intensity laser field is a more difficult case to ascribe causes to—such collisional issues are beyond the purview of this thesis but can be explored further in [130].

The MOTs that were used for high-quality BEC runs were in the range $10^8 < N < 10^9$, with the photodiode and CCD calculations agreeing within 50%. Larger MOT number unfortunately did not guarantee good dipole trap loading, and low MOT number did not prevent the same, but it appeared that having a large MOT

presented one with a larger “capture range” in parameter space when adjusting the various trap-loading parameters; see §3.1 for more detail.

2.3 The dipole trap

This apparatus was designed and built to accommodate a crossed-beam dipole trap, a decision which was largely based on the design of the groundbreaking Georgia Tech experiment [12]. As the experiment progressed, however, we decided that a single-beam trap would be sufficient to achieve condensation and the alignment difficulties of the crossed-beam trap could be left for another day. As such, unless otherwise mentioned, when discussing results from the dipole trap it can be assumed that I am referring to a single-beam setup, with the attendant cigar-shaped equipotential.

We utilized a laser provided by Coherent/DEOS—the GEM-50S, which was a scientific version of a relatively new (at the time) OEM product line. Specifications delivered with the laser claimed an output power of 67 W. Driving the laser was a manufacturer-provided RF power supply, itself supplied by approximately 20 A of DC current at 35 V, courtesy of a Hewlett-Packard 6573A supply. Both the laser module and the RF power supply were water-cooled by a ThermoNESLAB M75 chiller. The laser was free-running at 10.59 μm .

2.3.1 Beam design

As described above, the vacuum system was built with access for two CO₂ laser paths, with 1" zinc selenide (ZnSe) windows providing access. ‘Black hole’-style beam dumps with conical dampers were used as final targets outside the exit windows. The focusing system is depicted in Fig. 2.10, and the final assembly (with ZnSe window mounts) in Fig. 2.11.

Four lenses were placed within the central spherical cube using ‘groove-grabber’ tools from Kimball Physics. These lenses were 1.5" focal length ZnSe aspheres provided by II-VI. Obviously, in-vacuum lenses are not a preferred solution in an ex-

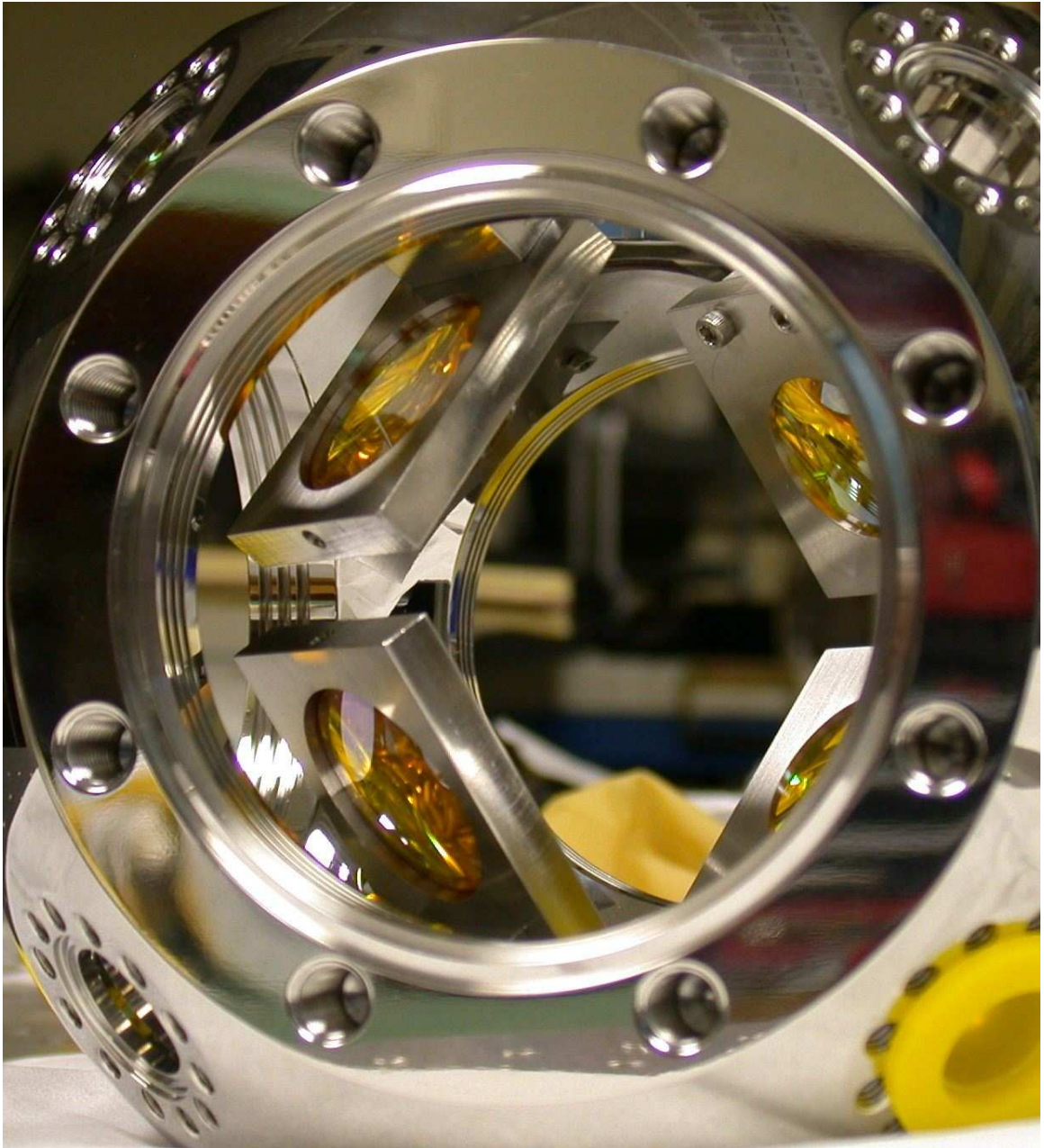


Figure 2.10: *Photograph of the 14-port (6 large, 8 small) ‘spherical cube’ and the in-vacuum focusing apparatus, prior to assembly and window-mounting. The yellow-orange lenses are $d=1''$, $f = 1.5''$ ZnSe aspheres, held by custom-built mounts aimed at locating the focus of the lenses as close as possible to the center of the chamber. Four lenses are present due to the initial desire to make a crossed-beam trap.*

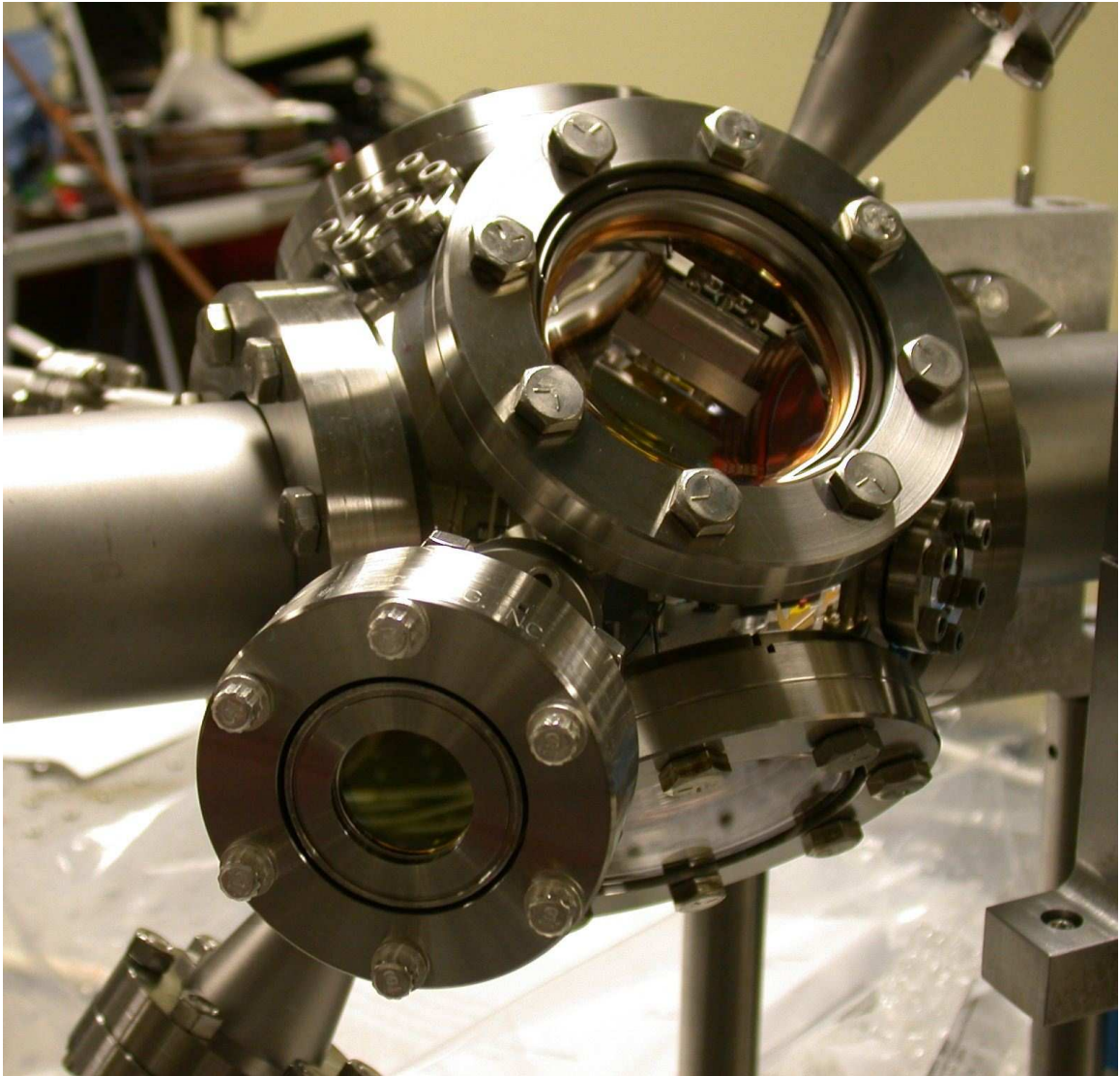


Figure 2.11: *Photograph of the assembled vacuum chamber; 3 of the 4 attached CO₂ laser access ports are visible, the frontmost being the entrance port used for the entirety of this thesis; the vertical ports were used only for brief forays into crossed-beam trapping. The 1" windows on the ports are of ZnSe, a material whose delicacy rendered the port seals bakeable to only 150° C. The larger glass windows are for MOT beams, and the smaller glass windows for probe beam traversal and general observation.*

periment that could require delicate aligning of optical path, yet the need for tight focusing trumped any concerns relating to convenience. The lens mounts were designed and machined locally with the aim of placing the relevant aspheric surfaces the proper distance from the center of the chamber, where the dipole trap would be overlapped with a MOT in order to initiate trap loading.

Aspheric lenses were chosen to allow for the strongest possible trap, i.e., the tightest focusing of incoming CO₂ laser radiation that the available geometry would allow, namely the maximum beam size that could enter our vacuum chamber, and the distance it would have to travel from entrance to the desired location. The use of aspheres was driven by the fear of spherical aberration; since we were choosing to use 1"-diameter lenses with $f = 1.5"$, we assumed (correctly) that the sought-after trap depths would require beam waists in the regime where spherical aberration would be a concern⁷.

Given that the ZnSe windows were 6" away from the trap-loading point, i.e., the center of the spherical cube and thus also the nominal center of the MOT's anti-Helmholtz field, the question of how to achieve the tightest possible focusing was addressed. It was obvious that we should use as short focal-length lenses as possible for final focusing, and it became obvious that the default beam size and divergence of the Coherent-DEOS laser at that point was extremely non-ideal.

We developed a Gaussian beam propagation [132] code in Mathematica to study the effects of an immobile external beam telescope on the resulting dipole trap characteristics. The laser manufacturer supplied reasonably trustworthy profilometry at 60cm beyond the output coupler, but only a vague estimate of beam waist at the output coupler. These values were used as inputs to the propagation code, which essentially was a 3-lens calculation, the accuracy of which was hampered by the lack of complete profile data on the laser. Measurements of the beam profile at the entrance to the vacuum chamber using a razor blade and a thermal detector were taken

⁷Ahmadi et al. explored this issue by creating dipole traps with strongly aberrated beams; in particular, they were able to create linear arrays of optical microtraps in well-separated intensity maxima [131].

to confirm Gaussian profile and that the input window was not being clipped; unfortunately, the accuracy of these measurements was not sufficient to provide useful information about aberrations.

We had 10", 4", and 3" plano-convex ZnSe lenses available for the external telescope, and through use of the propagation code we settled on a 4"-10" configuration. A third geometrical limiting factor was discovered in the optimization process: the fact that the focused beam would need to escape the vacuum chamber without significant occlusion, which when present resulted in heating of the vacuum chamber walls and significant increases in UHV pressure.

The telescope position was moved significantly from where the initial design had placed it to allow for tighter confinement, and the attendant increase in trap frequency was observed, as explained in §3. The values for w_0 predicted by the code were $20\mu\text{m}$ and $15\mu\text{m}$ for these cases, disagreeing with the waists predicted by parametric resonance measurements of the trap frequencies ($46\mu\text{m}$ and $36\mu\text{m}$ again detailed in §3), but were a good guide for the construction and initial steps of this experiment in that the code predicted significantly tighter focus through the use of the telescope. Possible culprits for this discrepancy include the fact that the telescope lenses probably introduced aberrations into the beam, the profile of which after acousto-optic modulation (see §2.3.2) was unknown, and (less likely) possible deviations from the paraxial condition near the focus of the beam.

2.3.2 Intensity measurement and control

Fast, precise, and accurate control of the intensity of the trapping beam was a fundamental concern with this experiment. Speed on the timescale of ms was required to implement evaporative cooling on timescales that exploited the high secular frequencies of the dipole trap; more importantly, speed on the timescale of μs was required to properly implement trap turnoff for ballistic expansion. Since the laser itself only was provided with a slow mechanical shutter, we utilized an acousto-optic modulator (AOM) to provide intensity control via variable intensity in the first diffracted

order. The AOM and its driver were both provided by Intra-Action (AGM-406b and GE series); the AOM crystal was of anti-reflection-coated germanium, desired for its transparency to $10.6 \mu\text{m}$ light. The driver provided up to 40W of radiofrequency power at 40MHz, dissipation of which required water-cooling of the AOMs.

Evaporative cooling was later performed using programmed rampdown of laser power. We thus required a mapping operation, first of trap depth to laser power (linear at high power but distorted at low power by gravity; see §3.3.2) and second of laser power to applied radiofrequency power. This latter mapping was simplified by the availability of amplitude modulation on the AOM driver—it thus became a matter of mapping AM voltage to diffracted power. This mapping is shown in Fig. 2.13. Evaporation was then a simple matter of taking the desired trap-depth-vs.-time profile and applying a lookup table that would output a voltage-vs.-time curve that was then input as an arbitrary waveform to a SRS DS345 synthesizer driving the modulator AM input.

The lookup table data was obtained through somewhat roundabout means. Maximum diffracted-order power was estimated beforehand to be as high as 50 W, yet available power measurement gear (a Coherent thermopile) peaked at 10W. We thus measured the profile of Fig. 2.13 in two parts: an initial exact procedure measuring power vs. voltage up to 10W, and a second procedure whereby we inserted a pickoff optic of unknown ($\sim 2\%$) reflectivity directing the majority of the light into a beam dump. This allowed the measurement of relative power over the full range of applied modulator power. The resulting two graphs were then matched up, giving us not only the reflectivity of the optic at that particular angle and polarization, but the true power vs. voltage curve.

2.3.3 Alignment

Typically the first aspect of this experiment that captures the imagination of visitors both lay and professional is the presence of a nominal 50W laser. Given that this power level needs to be directed into the heart of a conventional vacuum chamber,

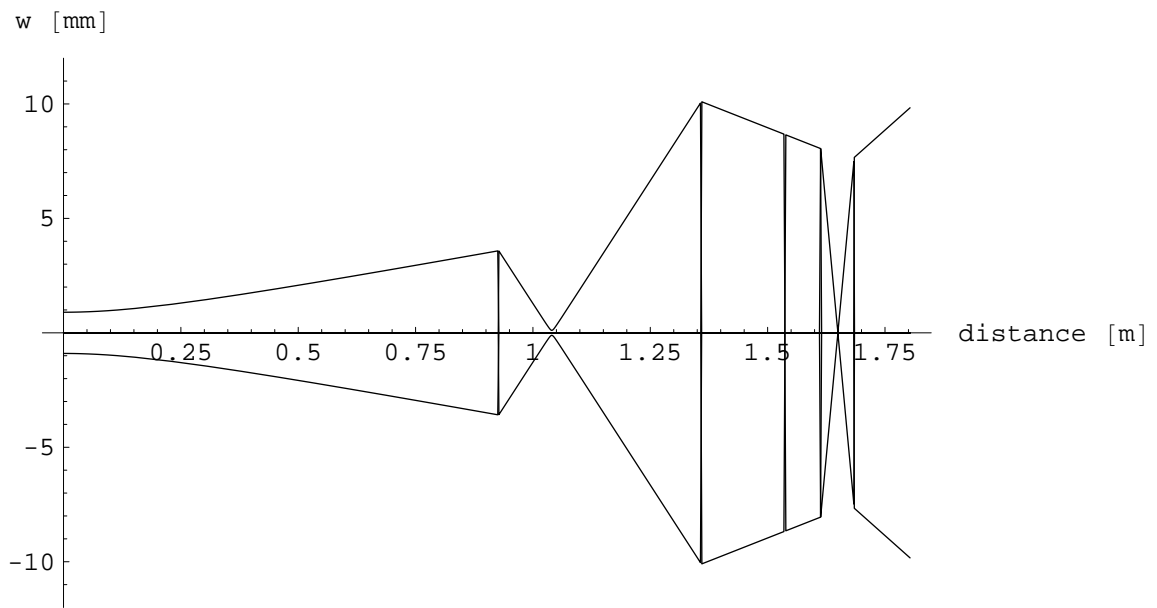
the question of alignment is an immediate concern. The strategy we adopted was to align a low-power HeNe beam such that it was co-propagating with the CO₂ beam, and thereafter align all shared optics using the visible beam. Overlapping of the two beams was effected through the use of a specialized beam-combiner optic, transparent at 10.6 μm and reflective at 633 nm, placed at 45° in between the directions of CO₂ laser and HeNe propagation.

This process had to be performed twice for any ground-up alignment, as the acousto-optic modulator detailed in §2.3.2 utilized a germanium crystal that was reflective at optical wavelengths. Since the laser operated only at full power, some care was required throughout, namely the use of carefully placed low-transmission optics as well as beam dumps to handle the unused (reflected) fraction. Actual alignment of the two beams was performed by directing the HeNe via a dogleg arrangement onto repeated burn spots at two locations along the beam path separated by approximately 50 cm. White cardstock was found to be most efficacious for this particular application, certainly more so than the infrared indicator card that had originally been purchased for alignment purposes. The overlap alignment after the AOM was rendered considerably easier through the intensity control afforded by the modulator; much more accurate burn spots could be developed using 10ms pulses at full power rather than several seconds at 1% power, which was required to align the region in front of the AOM.

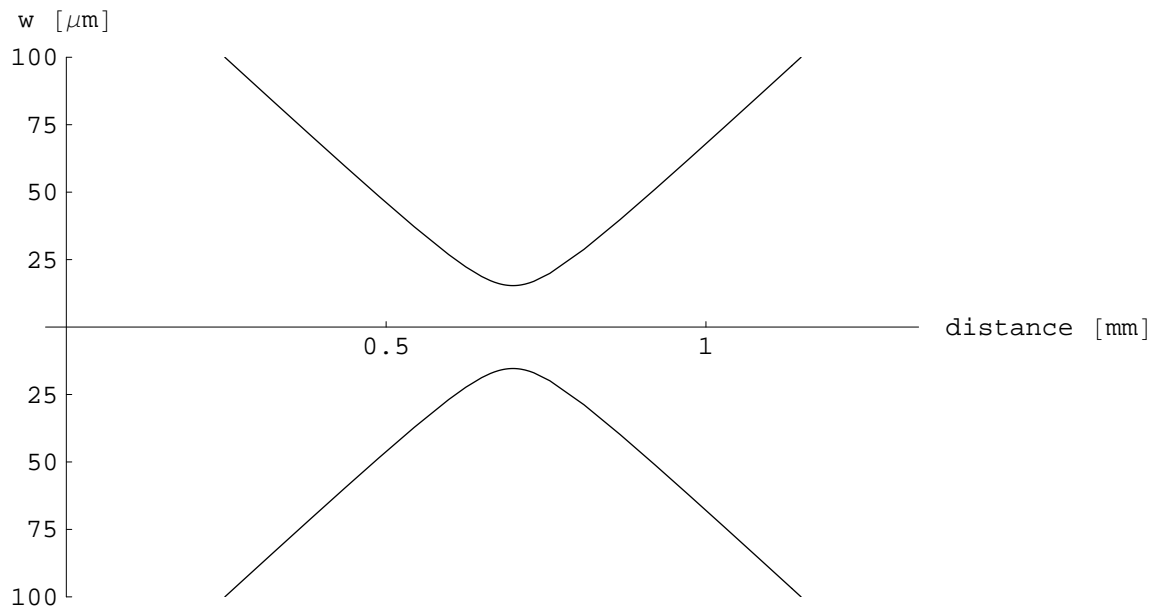
A clever technique for aligning the beam such that it arrived perpendicular to the aspheric in-vacuum lens was described in [133], whereby interference rings from the front and rear surfaces of the ZnSe lens are observed outside the vacuum system using a pinhole arrangement. We found this technique quite straightforward and used it repeatedly as the second step in the alignment after confirming proper overlap of the CO₂ laser and the HeNe.

Since there were small errors in the mounting of the in-vacuum lenses, the ultimate alignment that provided the best fringes was not necessarily associated with exact centering of the HeNe on all four relevant optics. Nevertheless, we found it

sufficient to have centered alignment on the entrance window and good fringing. No clipping-induced pressure increases occurred in such cases, although whenever beam size in-vacuum was changed (through varying the arrangement of the external telescope), some transient pressure increase was observed, ostensibly due to small amounts of rubidium gathered on the in-vacuum lenses. Running at high power for several seconds in any new arrangement typically eliminated the problem.



(a) Full picture



(b) Zoom

Figure 2.12: Results of the Gaussian-beam propagation code designed for the CO_2 laser, predicting waist location and size.

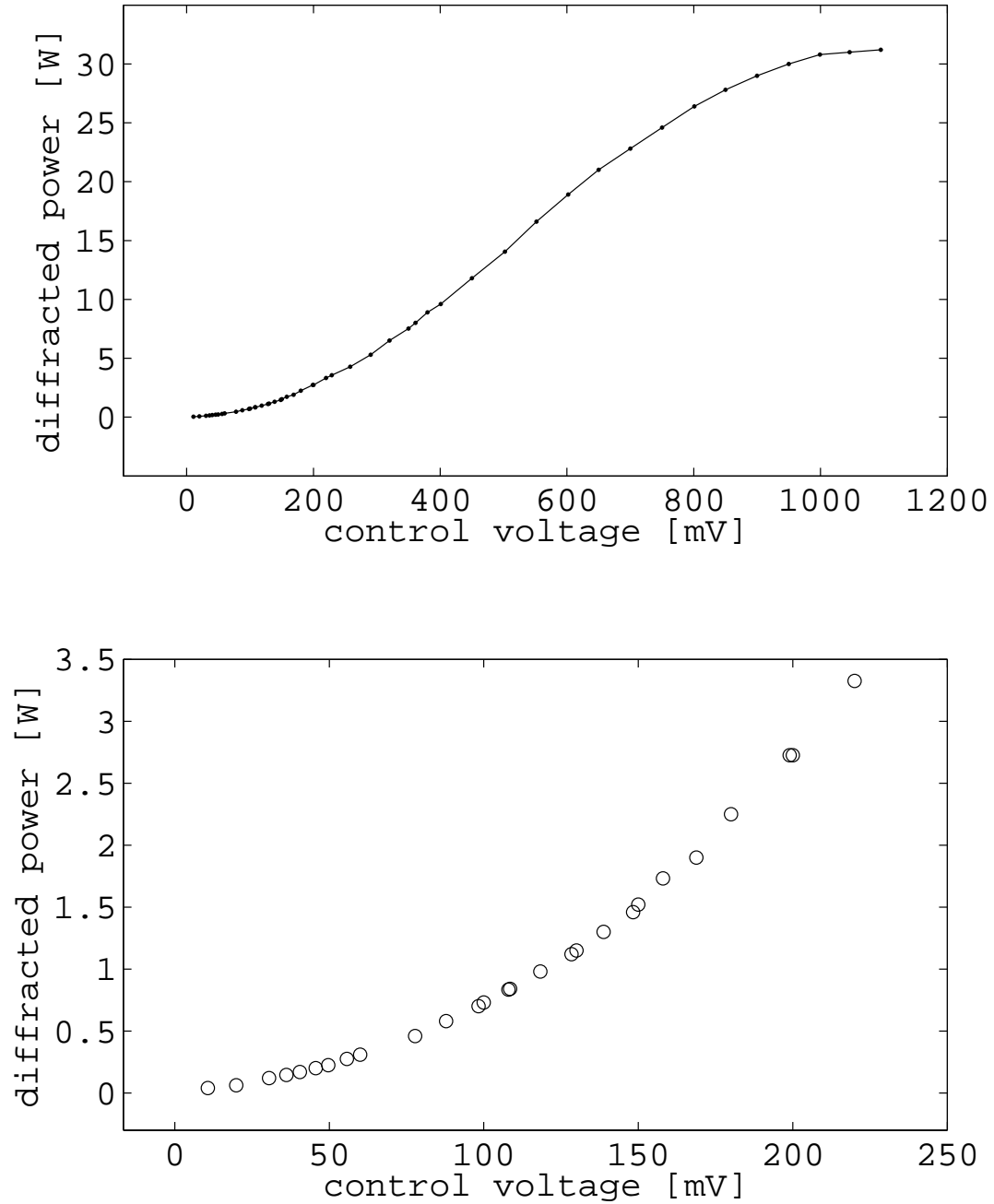


Figure 2.13: Calibration curve for the germanium acousto-optic modulator and for the design of evaporative paths. A desired path $U(t)$ was first converted into power, and then into applied RF amplifier control voltage.

Chapter 3

All-optical BEC

Data are sent like a fireball at midnight,
Numbers and images bundled up tight;
One bit of darkness lit up to posterity,
All of the instruments sleep well tonight.

JOHN M. FORD
“All Our Propagation.”

THE BULK OF THE LABOR involved in this thesis was involved in creating a generalized (spinor vs. scalar) version of a well-known state of ultracold matter using nontraditional and largely undocumented means, with all the attendant experimental cul-de-sacs and frustrations of such a venture. It succeeded through a measure of both luck and what the author would like to think was a thorough attempt at understanding what was going on in the experiment from trap loading to the onset of degeneracy and afterwards. This chapter will document the experimental steps taken to achieve single-beam all-optical BEC and (when necessary) the related theoretical justification.

3.1 Loading the dipole trap

The raw material from which the condensate is created is a thermal sample of atoms trapped at a local maximum of optical intensity far enough off-resonance such that

the atomic response can be approximated by the atoms' DC polarizability α . Atoms in the vicinity of a single-beam dipole trap oriented horizontally (along x ; z vertical) thus experience a conservative potential given by:

$$U(x, y, z) = \frac{U_0}{1 + x^2/x_R^2} e^{-2\frac{y^2+z^2}{w_0^2(1+x^2/x_R^2)}} - mgz \quad (3.1.1)$$

where x is the direction of propagation, w_0 is the beam waist, mgz is the gravitational potential energy, and x_R is the Rayleigh range:

$$x_R = \pi \frac{w_0^2}{\lambda} \quad (3.1.2)$$

and where λ is the CO₂ laser wavelength $\lambda = 10.59\mu\text{m}$. This potential is illustrated in Fig. 3.1. The well depth U_0 is given (per §1.2) by:

$$U_0 = \frac{\alpha}{2\epsilon_0 c} \frac{2\mathcal{P}}{\pi w_0^2} \quad (3.1.3)$$

Expanding Eq. 3.1.1 around the origin (ignoring gravity) yields formulae for the secular frequencies:

$$\omega_r = \sqrt{\frac{4\alpha}{\pi m \epsilon_0 c}} \frac{\sqrt{\mathcal{P}}}{w_0^2} \quad (3.1.4)$$

$$\omega_z = \sqrt{\frac{4\alpha}{\pi m \epsilon_0 c}} \frac{\lambda}{\pi \sqrt{2}} \frac{\sqrt{\mathcal{P}}}{w_0^3} \quad (3.1.5)$$

In principle the waist radius w_0 should be knowable from proper simulation of the optical system, but extremely tight focusing and imperfect external telescope lenses make this difficult. Trap-frequency measurements described in §3.8 imply a value for w_0 in our system of 36 μm , and a full-power trap depth of 1400 μK (31.2 W being the most recent maximum of the AOM calibration).

Treating the two frequency expressions as equations for two unknowns U_0 and w_0 ,

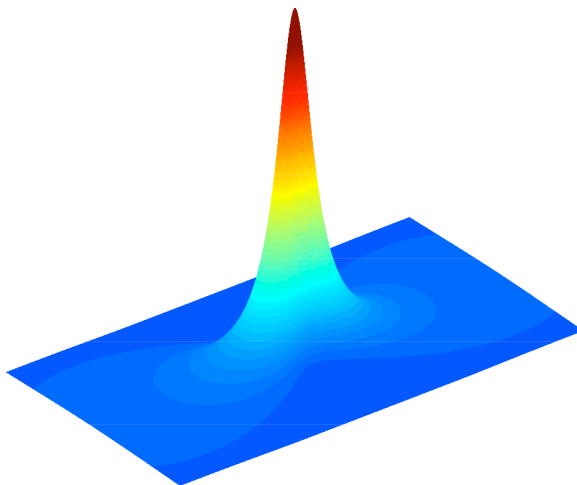


Figure 3.1: A depiction of the $z = 0$ slice through the potential energy curve given in Eq. 3.1.1. The length of the long axis is $10x_R$, and that of the short axis $10w_0$.

we solve for U_0 , resulting in a charming expression for trap depth solely dependent on trap frequency:

$$U_0 = \frac{1}{2}(\nu_r^4/\nu_z^2)m\lambda^2 \quad (3.1.6)$$

This procedure provides a convenient check, in that one can estimate the trap depth predicted by the known laser power and the predicted w_0 , and compare with the trap depth predicted by the frequencies alone. In this case, using a waist of $36 \mu\text{m}$ gives a trap depth of $1120 \mu\text{K}$ for 31.2 W of CO_2 laser power. While this is significantly different from the $1400 \mu\text{K}$ predicted from frequency measurements, it should be remembered that the fractional uncertainty in trap depth is much greater (by a factor of $\sqrt{4^2 + 2^2}$) than the fractional uncertainty in trap frequency, which is itself certainly no better than 5%. Gravity will of course affect the estimates of trap depth at low power; this will be discussed in §3.3.2.

3.1.1 Background on technique

In the magnetic trapping community, transfer from a laser-cooling stage is fairly simple and is usually a matter of ‘mode-matching’ the magnetic trap with the quadrupole

field of a compressed MOT [31, 134]. It is not unremarkable using this process to obtain highly efficient transfer from a MOT, and thus obtain large condensate numbers, easily in excess of 10^6 atoms. This luxury was not initially present in the optical trapping community due to the lack of trap *volume* for similarly deep traps; in this respect the tight confinement presented by focused off-resonant lasers was a disadvantage. The seminal 1995 optical trapping and evaporation effort started with only 5000 atoms, five orders of magnitude away from initial conditions in typical early magnetic trapping experiments [31, 134]. For a dipole trap to be a viable path to BEC, the name of the game is to obtain as efficient a transfer as possible from a precooled stage. The 1995 crossed-beam experiment [43] relied on overlapping the $U_0 \sim 1$ mK dipole trap with a sodium MOT operating at -15 MHz (1.5Γ) with a single-beam MOT intensity of 3 mW/cm². This overlapping was performed for two seconds after which the MOT beams and gradient were turned off. An order of magnitude improvement in dipole trap number (up to $N \sim 5000$) was claimed by introducing a dark SPOT phase [135] during the final 20 ms of overlap via reduction of repump power. The presumed reason behind this improvement was the reduction in density-limiting scattering forces in the MOT. The 1993 rubidium FORT took a different approach in which they chopped the MOT beams and the $U_0 \sim 6$ mK trap alternately, at 200 kHz. This was done to allow energy dissipation even in the dipole trap region, where the MOT beams would otherwise be effectively shifted above resonance due to the difference between ground- and excited-state polarizabilities. This procedure yielded 10^4 atoms in the trap [42]. The initial quasi-electrostatic experiment combined both of these thoughts—by having a period of reduced repump intensity combined with detuning of the MOT light by 20 MHz, more than 10^6 atoms were loaded [45].

The 2001 all-optical BEC perfected this line of inquiry, obtaining 2×10^6 atoms at $75 \mu\text{K}$ in a crossed dipole trap approximately $500 \mu\text{K}$ deep and with spherically symmetric trapping frequencies of $\omega/2\pi = 1.5$ kHz. This startling result corresponded to initial phase-space densities $\rho > .001$ and elastic collision rate $\gamma > 10^4 \text{ s}^{-1}$. The major step forward was a realization of a tightly confining trap with relatively large

volume ($w_0 \sim 50\mu\text{m}$), and the realization that further detuning during the loading phase (out to -140 MHz in this case) was beneficial. While the detuning and trap geometry issues were matters of experimental trial, it remained obscure how such high initial densities (beyond 10^{14} cm^{-3}) were achievable in a situation where loading occurred in equilibrium with a laser-cooling apparatus, albeit one that was dark and detuned. A secondary, serendipitous dark SPOT was proposed for this improvement in loading efficiency, whereby the light shift moved the repump out of resonance at the heart of the trap, allowing local density to surge [12]. In addition, the period of time between the extinguishing of all near-resonant light and the first observations of the trap is as large as 100 ms; it is conjectured [133] that this period witnesses strong free evaporation and reequilibration¹ (which continues out to several seconds, see §3.3.1).

3.1.2 Our approach

Our approach used a single focused CO_2 laser beam instead of a crossed pair. While we initially built the experiment to duplicate that geometry, it was thought that the combination of higher CO_2 laser power and higher MOT number (10^9 vs. 10^7) would balance the loss in mean trap frequency. This assumption turned out to be incorrect, but not disastrously so; condensation was still achieved, albeit with the evaporation process slowed down somewhat.

Fig. 3.2 shows pictures taken during a typical loading sequence, which we largely adapted from the 2001 paper. The sequence begins with the CO_2 laser being turned on using the AOM. Immediately, the MOT is first rendered ‘dark’ by strongly reducing the repump intensity. After 20 ms the MOT beams are detuned another 50 MHz beyond the default detuning of $\delta = -10$ MHz. After 40 ms of this configuration, all resonant light is shut off, as well as the quadrupole field used by the MOT. The repump field is shut off 2 ms before the cooling transition, in order to ensure optical pumping

¹This process was investigated recently in all-optical sodium BEC experiment, confirming the early onset (and importance) of free evaporation [136].

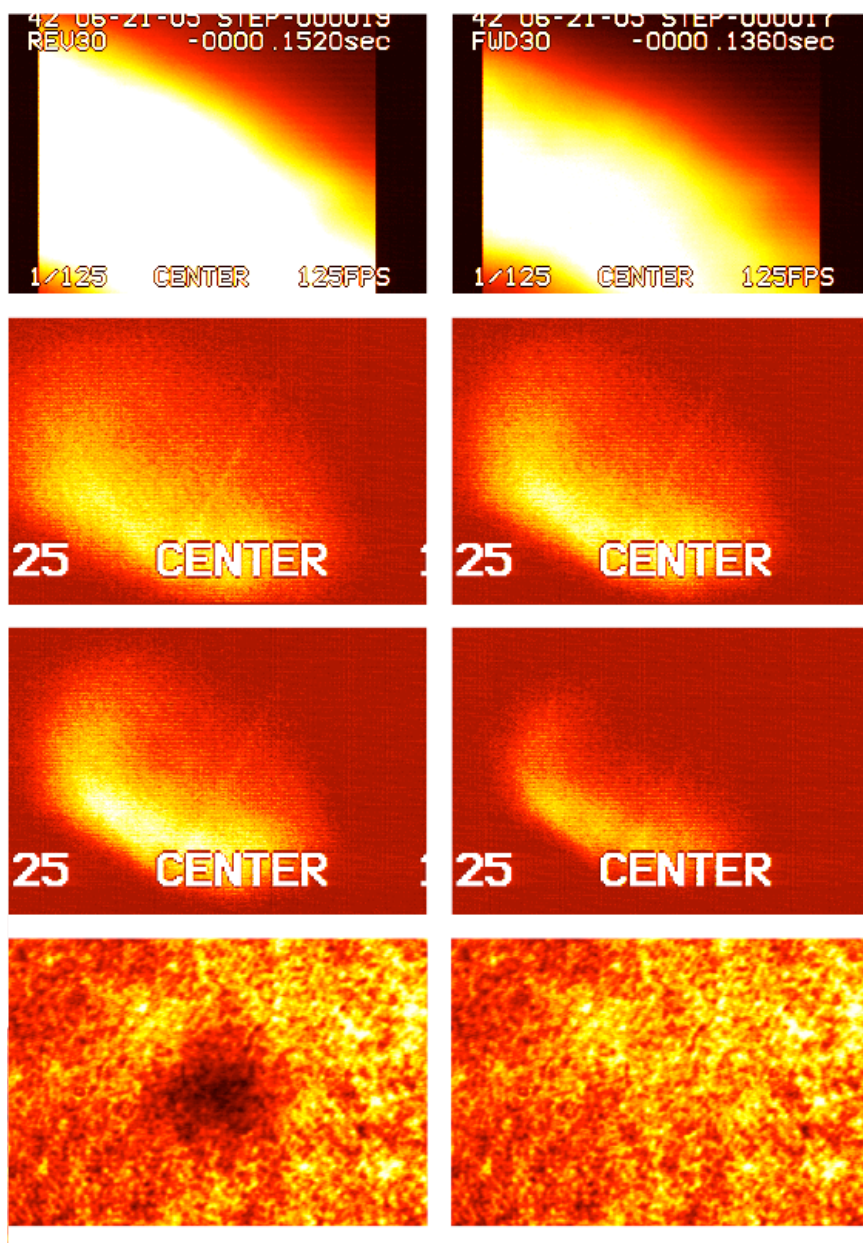


Figure 3.2: *CCD images taken of the trap loading process. Images proceed in time left-to-right and top-to-bottom. The first two images are full-screen shots of the MOT as repump intensity is reduced for a 20ms ‘dark’ phase. The trap is then detuned 60 MHz. The next four images show the presence of the dipole trap, revealed by a narrow line of fluorescence centered near the MOT. After 40 ms of detuning, all light is extinguished and untrapped atoms are left to fall away. The final two images show the two exposures of the probe beam pulses: the first in the presence of a released dipole trap that has undergone 1.5 ms of ballistic expansion, and the second image a reference shot with no atoms. The final two images are divided to obtain absorption images such as in Fig. 3.4.*

into the $F = 1$ ground state via off-resonant excitation of the $F = 2 \rightarrow F' = 2$ transition. The dipole trap is left to evolve in the dark for a period of time no less than 90 ms (in order to let untrapped atoms fall away) before being probed via absorptive imaging.

The dipole-trap loading process was the central mystery of this experiment. Obtaining enough atoms to begin confident evaporation with was the goal of many experimental diversions and proposals. It is clear, however, that for a given trap geometry, it simply does not help to have extremely large MOTs as reservoirs; the expected increase in trap loading from having access to a large MOT as reservoir was quite naïve in retrospect. The loading dynamics within the dipole trap appear to place stringent limits on trap number as a consequence of limited trap volume. The startling increase in density made available by the detuning/dark SPOT technique was deceptive in that it could not be increased arbitrarily. The obvious solution to this problem is to cool into a much larger trap. An ironic note is that our initial designs had much larger trap volume, yet our familiarity with the vicissitudes of trap loading at the time was low; we thus went as tight as possible and proceeded from there. Possible solutions to this issue will be discussed in the final section.

Given an apparent upper limit of $\sim 2.5 \times 10^6$ for our tightest trap, it was desirable (at least) to achieve that amount on a regular basis. Three factors dominated the landscape of ‘tweaking’ that determined quality of trap loading given an average MOT of several 10^8 atoms. The most sensitive degree of freedom was dark-SPOT repump (DSRP) intensity at the trap location. Typical estimates of our optimal DSRP intensity were in the 10–25 $\mu\text{W}/\text{cm}^2$ regime, although this was by no means a constant. Yet for a given sequence of runs, a 20% change in intensity in either direction would yield strong changes in trap loading, often as great as 50%. Periodically performing runs at slightly higher or lower DSRP intensity kept this variance in check, however. Secondly, since the MOT was not colocated with the dipole trap due to offsets in alignment, coil geometry, and ZnSe lens placement, some effort was needed to make sure that the MOT compressed and darkened at the correct location.

This was accomplished largely through the use of bucking fields originally in place to zero out the background field. Bucking fields of ~ 0.5 G were effective at moving the MOT around and placing it such that fluorescence from atoms colocated with the dipole trap was observed during loading (see Fig. 3.2). Unfortunately this had the rather obvious side effect of presenting a significantly nonzero field during the loading phase, which significantly affected the dynamics of the MOT cloud as it was detuned by up to 150 MHz.

Given that detuning beyond the amount needed to cancel the CO₂ laser light shift appeared to reap benefits, we expected that the efficacy would continue to improve all the way out to a detuning of $\delta \sim -140$ MHz, at which point the laser light would become more accurately described as being to the blue of the $|F = 2\rangle \rightarrow |F' = 2\rangle$ transition [137]. Indeed, details of the 2001 experiment showed that loading was completely ineffective until the light shift was cancelled, then rose sharply with further detuning, peaking beyond $\delta = 120$ MHz, but not falling off significantly beyond that [133]. Our goal was thus to detune as far as this, necessitating the construction of an offset lock circuit capable of such significant jumps without the use of AOMs. While the offset lock performed adequately, a significant problem with the loading process is that the detuning process was lossy, i.e., detuning the MOT for tens of milliseconds and then bringing it back did not come close to preserving atom number. This problem was worse for larger detunings and longer times. We initially attributed this loss to transients in the offset lock jump, but it was quickly discovered that the number loss was linear in time spent detuned. The culprit, then, was deemed to be the strong background field, which surely interferes with the health of the detuned dark SPOT. Since the fields were necessary, we found an equitable solution of not detuning particularly far, typically settling at going out to -60 MHz, or -10Γ , for optimal loading.

Finally, MOT intensity during the loading phase was critically important to break through the final factor of two in initial atom number. While quality MOTs of order 10^9 atoms were loaded using a total MOT power (in six 1" beams) of 30 mW, it was

found that running at high power, up to 80 mW, yielded strong gains in loading. Operating the MOT at these intensities (obviously far above saturation) did not change its performance significantly, but the necessity of sending enough power to the 2D-MOT placed a fundamental limit on how far we could push the MOT intensity.

In summary, loading the dipole trap to consistently high numbers was a formidable task with repeatability that (while significantly improved) remains questionable. It is the author's hope that the next generation of the experiment will have a chance to address several of these issues.

3.2 Characterization and phase space density

Obtaining Bose-Einstein condensation in a trapped atomic vapor is a process that relies on understanding what the peak phase-space density ρ of the sample is—and thus understanding how close to the phase transition one is. In principle the intuitive path is to keep track of both mean particle separation $n^{-1/3}$ and deBroglie wavelength $\lambda_{dB} = h/\sqrt{2\pi mk_B T}$. In practice density *per se* is not tracked—rather the parameters involved in calculating ρ are observed:

$$\rho = \kappa_h N \left(\frac{\hbar\bar{\omega}}{k_B T} \right)^3 \quad (3.2.1)$$

where κ_h is an estimated correction factor ($0 < \kappa_h < 1$) set by the anharmonicity of the trap and (if necessary) gravitational sag. Relative spin populations in the sample raise the requirement for reaching the phase transition up from $\rho = 1.202$; the three populations $m_F = 0, \pm 1$ condense separately, meaning if the evaporating cloud is in one spin population the correction is unity, and if it is evenly distributed among all three, the required ρ increases by a factor of three. The task at hand, then, is to accurately measure N , T , and $\bar{\omega}(\mathcal{P})$.

3.2.1 Number

Using the absorption setup introduced in §2.1.3, we measure the number of ^{87}Rb atoms by illuminating the sample (which is in the $|F = 1\rangle$ ground state) first with a pulse of repump light designed to optically pump the cloud into the upper $|F = 2\rangle$ ground state, and then with two temporally separated short pulses of probe light on the $|F = 2\rangle \rightarrow |F' = 3\rangle$ transition, typically $50\mu\text{s}$ long and 15ms apart. The first pulse is absorbed partially by the atomic cloud, and the second pulse provides a ‘background’ image for effective measurement of optical depth (all the atoms having been dispersed by the heating effects of the first pulse). Intensity control is provided by AOMs.

Light is known to propagate through an absorbing medium (such as the trapped atomic cloud) according to Beer’s law²:

$$I(\mathbf{r}_\perp) = I(\mathbf{r}_\perp, 0)e^{-D(\mathbf{r}_\perp)} \quad (3.2.2)$$

where $D(\mathbf{r}_\perp)$ is the optical depth along a line of sight parallel to the probe beam’s propagation, at a point in the plane (perpendicular to that propagation) $\mathbf{r}_\perp = \{x, y\}$.

The two images taken provide snapshots of both $I(\mathbf{r}_\perp)$ and $I(\mathbf{r}_\perp, 0)$, and due to the imaging optics provide a clear picture of the column density distribution of atoms. It is trivial to obtain the optical depth profile from the two absorption images:

$$D(\mathbf{r}_\perp) = -\log\left(\frac{I(\mathbf{r}_\perp)}{I(\mathbf{r}_\perp, 0)}\right) \quad (3.2.3)$$

Relating optical depth to atomic density information proceeds as follows. The optical depth is found by following the path of light in an absorbing medium via a column integration:

$$D(\mathbf{r}_\perp = \{x, y\}) = \sigma \int_{-\infty}^{\infty} n(x', y', z')|_{x,y} dz' \quad (3.2.4)$$

²Also known as the Beer-Lambert law or the Beer-Lambert-Bouguer law, the relevant years of proposal perversely being 1852, 1760, and 1729.

where σ is the interaction cross-section and $n(x, y, z)$ is the atomic density distribution.

To obtain the total number N we simply integrate over the image plane, and convert the equation to discrete notation featuring area elements (CCD pixels) of area A . This yields:

$$N = \frac{A}{\sigma} \sum_{ij} D_{ij} \quad (3.2.5)$$

The absorption cross-section depends on the polarization of the light used and the initial state of the atoms, and exhibits a well-understood dependence on frequency and intensity [137]:

$$\sigma = \frac{\hbar\omega\Gamma/2I_s}{1 + 4(\delta/\Gamma)^2 + I/I_s} \quad (3.2.6)$$

which reduces to the on-resonance low-intensity limit given in the numerator. Using the linear optics cross-section not only serves to simplify the algebra; the intensity also needs to be low in order that Beer's law as stated above is valid, as it assumes linear behavior. Corrections are calculable, but low intensity rendered them unnecessary [138, 139]. In addition, in general any image with any optical depth greater than 2.5 was deemed unreliable for number measurements, given the 8-bit dynamic range of the CCD, the possible 'pedestal' effect from using a diode laser, and the distortion caused by a dense cloud acting as a lens. The question of which saturation intensity to use is a somewhat thorny issue. Since the probe beam itself measures a completely redistributed population of $|F = 2, m_F\rangle$ states in an arbitrary background magnetic field, the randomly-polarized $I_s = 3.58 \text{ mW/cm}^2$ is most appropriate. Given that switching from linearly to circularly polarized probe light via a $\lambda/4$ plate produced no significant change in measured optical depth confirmed this choice. The conversion

between total optical depth and number is then simply:

$$N = 2.12 A(\mu\text{m}^2) I_s(\text{mW}/\text{cm}^2) \sum_{ij} D_{ij} \quad (3.2.7)$$

The effective area of the pixels (which will also be of paramount importance in measuring temperature) is calibrated by imaging the action of gravity on a ballistically expanding cloud; for details, see Fig. 3.3.

3.2.2 Temperature

Thermometry on a trapped Maxwell-Boltzmann gas is typically performed through the analysis of the spatial extent of the gas in the time following its release from the trapping potential. Assuming the trap is turned off quickly, one can calculate what the size of an atomic cloud at temperature T will be as a function of time. In principle, one can fit measurements of the cloud size at a series of times and extract not only the temperature but the initial sizes; for a cylindrically symmetric trap there are thus three quantities of interest, which can also be phrased in terms of temperature and the relevant trap frequencies.

We approximate the dipole trap potential (Eq. 3.1.1) as harmonic about the origin; given that the trap rapidly equilibrates to $\eta \equiv U_0/T > 10$ this approximation is largely valid. It is possible to calculate correction factors for peak density n_0 and thus peak phase-space density ρ of a Maxwell-Boltzmann gas at temperature T in a quasi-harmonic situation such as the single-beam trap. Such calculations are detailed elsewhere [133], and while the correction factors for our trap can be as significant as 20% (on the unhelpful side!), we largely assumed this worst-case scenario when searching for BEC. Any thermal density measurements quoted in this thesis use this correction factor of 0.8, which is a constant as long as η is unchanging—a fine approximation as long as free evaporation has ceased and dU/dt is slow enough for rethermalization.

The velocity distribution of a Maxwell-Boltzmann gas is well-known:

$$f(\mathbf{v}) = \frac{1}{(2\pi\sigma_v^2)^{3/2}} e^{-\mathbf{v}^2/2\sigma_v^2} \quad (3.2.8)$$

where the width of the velocity distribution is the standard thermal velocity:

$$\sigma_v = \sqrt{k_B T/m} \quad (3.2.9)$$

Conveniently, the density distribution of a Maxwell-Boltzmann gas in a harmonic potential is known to be Gaussian with widths σ_t and σ_l corresponding to the two transverse directions and one longitudinal of the dipole trap:

$$n(\mathbf{r}, t = 0) = \frac{1}{(2\pi)^{3/2}\sigma_t^2\sigma_l} e^{-(y^2+z^2)/2\sigma_t^2} e^{-x^2/2\sigma_l^2} \quad (3.2.10)$$

Ballistic expansion is achieved simply by turning off the trap on a timescale much quicker than the trap frequencies. The trap turnoff condition is simply $dU/dt \gg \omega_{max}^2$; the same condition (inverted) is encountered later as the condition for adiabatic compression or expansion of a condensate.

Obtaining the trap sizes as functions of time $\sigma_l(t)$ and $\sigma_r(t)$ is simple convolution:

$$n(\mathbf{r}, t) = \iiint_{\infty} n(\mathbf{r} - \mathbf{v}t) f(\mathbf{v}) d\mathbf{v} \quad (3.2.11)$$

This integration yields the following expression, perpetually Gaussian:

$$n(\mathbf{r}, t) = \frac{1}{(2\pi)^{3/2}\sigma_i(t)^2\sigma_l(t)} e^{-(y^2+z^2)/2\sigma_i(t)^2} e^{-x^2/2\sigma_l(t)^2} \quad (3.2.12)$$

The time-dependent widths are given by:

$$\sigma_i(t)^2 = \sigma_i(0)^2 + \frac{k_B T}{m} t^2 \quad (3.2.13)$$

What is observed, of course, is the column density along a particular line of sight:

$$n_{\text{col}} = \int_{-\infty}^{\infty} n(\mathbf{r}) dz \quad (3.2.14)$$

which results in a Gaussian image with no change in the widths along the remaining directions. In practice, we reduce the temperature measurement to a single parameter—the transverse width of the cloud at time t_0 great enough such that the temperature is simply found through the relation $\sigma_t/t = k_B T/m$. The σ_i are found through non-linear least-squares fitting of the absorption images of the expanded cloud to the ideal Gaussian form of Eq. 3.2.12, with t_0 being an easily varied experimental parameter. Conveniently, any small errors incurred through the linear expansion approximation err on the side of higher temperature, which helps avoid self-deception in the search for the BEC transition. It is also worth noting that this approximation can be more quantitatively phrased as $(\omega_{\min} t_0)^2 \gg 1$, since the radii of a Maxwell-Boltzmann gas in a harmonic trap are related to the trap frequencies via the expression $\sigma_i^2 = \sqrt{k_B T / m \omega_i^2}$. Two thermal clouds and the best-fit clouds are depicted in Fig. 3.4, and similar images from after the absorption apparatus was stabilized against vibration are shown in Fig. 3.5. In addition to providing temperature information, the fit parameters provide a nice check of atom number N via the total area under the best-fit curve. Examples of the in-situ clouds are shown in Fig. 3.6; one is shown with the absorption imaging system in focus and one without. The difference between the two is the position of the objective lens with respect to the dipole trap and the emerging ‘shadow’—the imaging lens and the camera itself remain fixed.

It should go without saying that the temperature measurement process described here ceases to have meaning in the presence of a visible condensate fraction, although forcing temperature fits of this sort tend to give lower limits to phase-space density, and can be useful. In such bimodal case one would either use the ‘wings’ alone of the absorption images for the fit, or one would truly account for both the Maxwell-Boltzmann and Thomas-Fermi profiles.

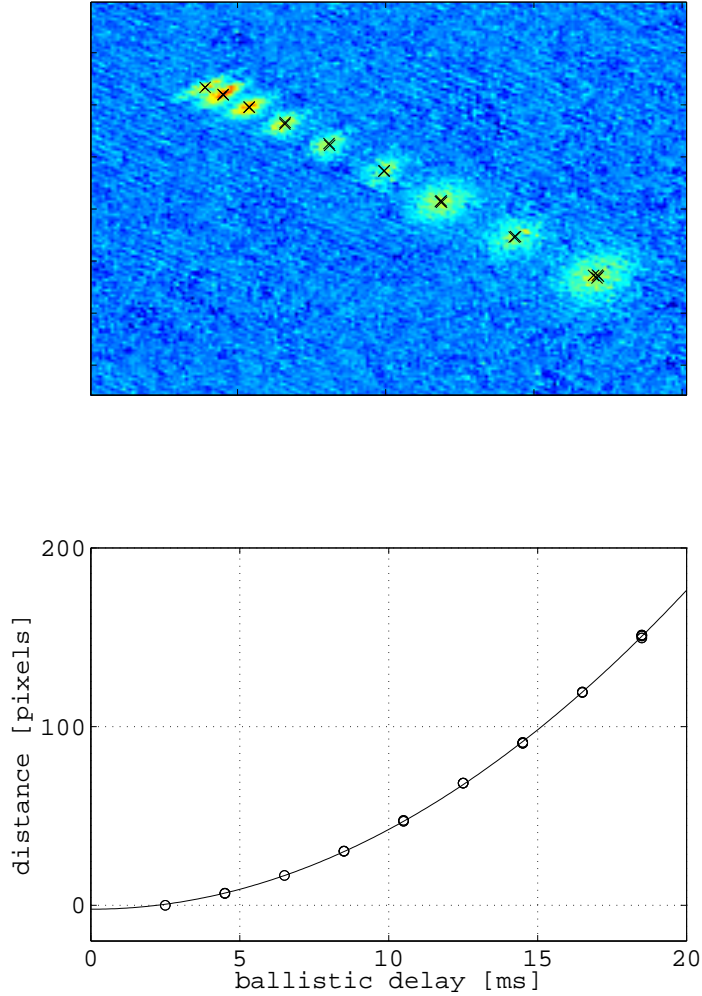


Figure 3.3: We finely calibrate the length scale of the absorption images using gravity. A trapped cloud (nominally at the focus of the imaging system) is released from the trap at $t = 0$ and falls under the influence of gravity while ballistically expanding. The centroid of the absorption image is calculated as two of the nonlinear fitting parameters described in Fig. 3.4. The distance of this centroid at time t relative to the first measured centroid ($\Delta = \sqrt{\delta x^2 + \delta y^2}$) is plotted above vs. time. Each point in the parabolic fit corresponds to one cloud on the image above; the image itself is the sum of many individual runs, superimposed for clarity. The points are fit to a parabola $y = \alpha t^2 + \beta$; the calibration number is then $\kappa(\text{pixels}/\mu\text{m}) = 4.9 \times 10^6 \sin \theta / \alpha$, where $\sin \theta$ represents the viewing angle with respect to gravity. In our case $\sin \theta$ is known from the cube geometry to be $1/\sqrt{3}$. Uncertainty in this length calibration is obviously not from the fit but rather pointing uncertainty, and possible distortions of the cloud positions as it falls out of focus. Unfortunately, since phase space density scales as the fourth power of κ , this renders it a major source of uncertainty.

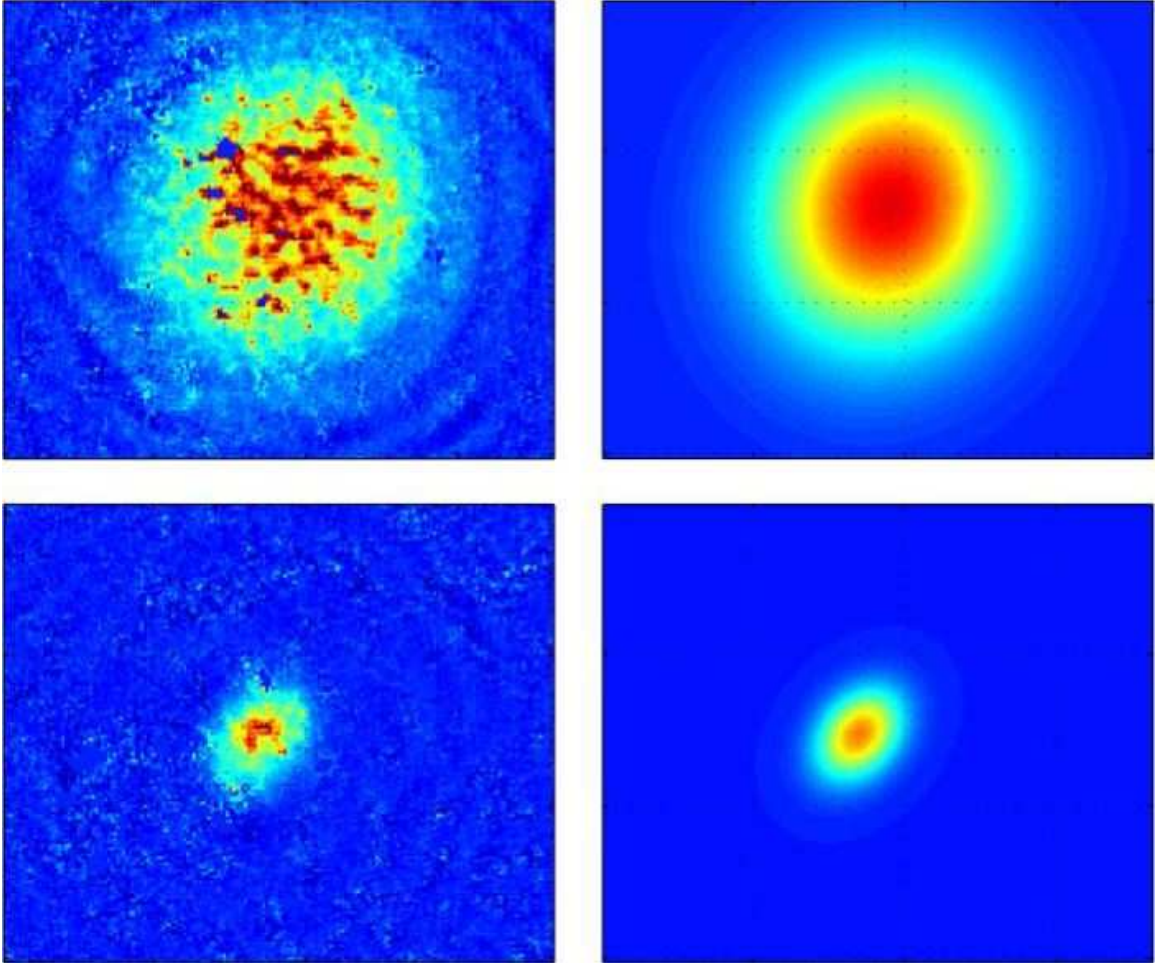


Figure 3.4: *Two thermal clouds and the nonlinear fit results yielding values for T and N . The fit includes seven parameters: amplitude, DC offset, two widths, X and Y positions on the image, and angle of rotation in the image plane. The upper image is taken immediately after trap loading, with a ballistic expansion time of 1.5 ms. The relevant parameters are $T = 200\mu\text{K}$ and $N = 2.3 \times 10^6$. The lower image is taken after an aggressive evaporation run and 17 ms of ballistic expansion. The cloud is fit to $T = 130\text{nK}$ and $N = 2 \times 10^5$. The field of view is 1.2×1.4 mm; the trap is oriented along the LL-UR diagonal as in Fig. 3.6, and gravity is directed to the lower right.*

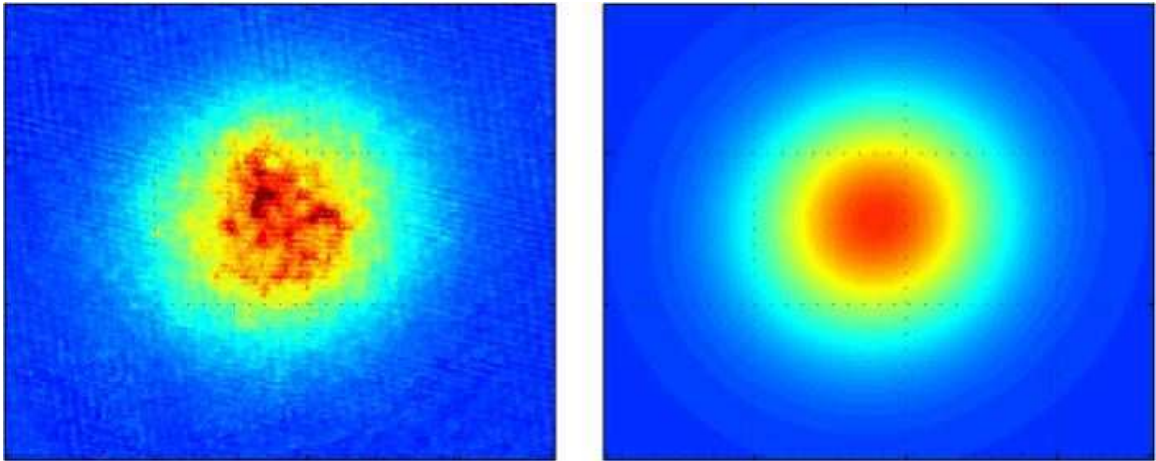


Figure 3.5: *The nonlinear fitting of thermal clouds with a vibration-stabilized imaging system. Observed temperature is $140 \mu\text{K}$; observed number 2×10^6 . The field of view is $1.2 \times 1.4 \text{ mm}$.*

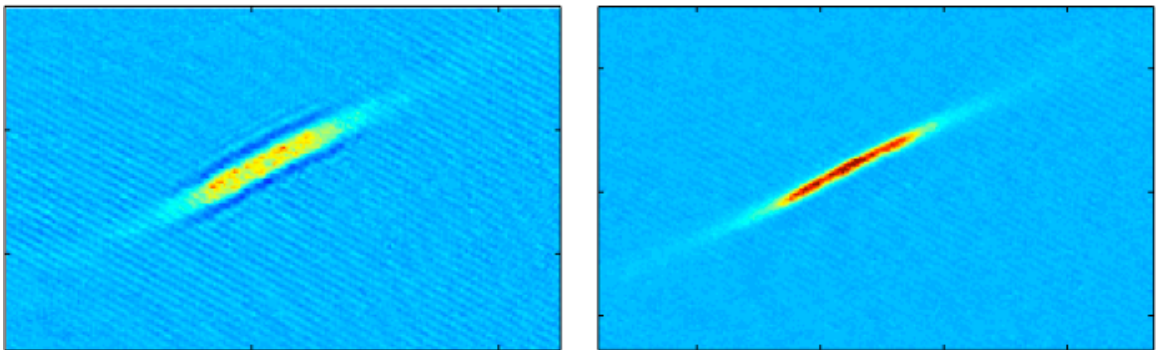


Figure 3.6: *In situ images of the optical trap, showing the difference that focusing makes. The out-of-focus image at left was taken with the objective lens approximately 2 mm farther away from the optical trap than the in-focus image at right. The field of view is $.9 \times 1.4 \text{ mm}$, and peak OD (represented by red) is 2.5.*

3.2.3 Trap frequencies

Direct measurements of the density (and for a given temperature, phase space density) of trapped atomic clouds using absorption of resonant light is simple in principle but undesirable in practice. *In situ* absorption images are difficult to interpret even if one has the resolving power necessary; the high density will saturate the optical-depth resolution of most CCDs, and a common fix, using off-resonant light, brings in the secondary problem of dispersion in the cloud, and thus the potential for considerable misdiagnosis of cloud size. Ballistic expansion allowing significantly rarefied clouds leads to considerably greater accuracy in number measurement, but density estimates then require precise knowledge of the trap geometry, which usually would come from some sort of Gaussian beam propagation code—an imprecise process, as shown in §2.3.1.

However, since there is a well-understood relationship between the secular frequencies of the confining potential and the density profile of the confined gas, either a Maxwell-Boltzmann gas or a BEC, measuring the trap frequencies becomes a powerful tool. In addition, the two unknown frequencies ω_r and ω_z transform easily into U_0 and w_0 , providing a second estimate of the former and a useful first estimate of the latter. After measuring these frequencies, we established a reference of trap frequencies for a given CO₂ laser power (or, more specifically, for a given control voltage passed to the germanium AOM). Thus for a given sample of atoms whose number and temperature we know, we can look up the relevant $\omega_i(\mathcal{P})$ in order to obtain phase space density ρ .

We measure the trap frequencies using the technique of parametric resonance [46, 140]. Given a system of particles trapped in a harmonic potential of frequency ω_0 , one can apply a periodic ‘kick’ to the system and expect to see resonant behavior similar to pushing a child on a playground swing. In this case, we apply an approximately sinusoidal variation at frequency Ω to the laser power \mathcal{P} and thus the trap depth U_0 .

The equation of motion for a particle in such a potential will then be:

$$\ddot{x}(t) + \omega_0^2[1 + b \cos \Omega t]x(t) = 0 \quad (3.2.15)$$

where $b \ll 1$. Solutions of this equation, known in mathematical physics as Mathieu's equation, are found [140] such that the displacement of the particle exponentially grows as $e^{\gamma t}$, where γ is found to be:

$$\gamma = \frac{1}{2} \sqrt{\left(\frac{b\omega_0}{2}\right)^2 - (\Omega - 2\omega_0)^2}, \quad \gamma \in \mathbb{R} \quad (3.2.16)$$

One thus expects to observe exponential heating and trap loss when the power is weakly modulated near $\Omega = 2\omega_0$. The width of this resonance should be approximately $b\omega_0$. Resonance also occurs when the frequency Ω is near to any $2\omega_0/m$, $m \in \mathbb{N}$; the width of the resonance, however, will increase as b^m , with the amplitude of the resonance decreasing [140].

We applied this technique to measure the two secular frequencies $\omega_r(\mathcal{P})$ and $\omega_z(\mathcal{P})$. Using standard loading, we obtained a trap at full power, evaporated to some variable final power, and then held that power for a fixed time, usually several seconds, while weakly modulating. A sample spectrum is shown in Fig. 3.7. Experimental convenience dictated that we modulate for a fixed number of periods rather than for the full holding time; the effect of this on the resonance shape is to presumably make heating at higher frequencies less efficacious due to shorter shaking time. A distortion of this type was visible occasionally for the low-frequency measurement (ω_z) but not in a consistent fashion.

The minimum for each curve represents twice the trap frequency, $2\omega_r$ or $2\omega_z$, at a particular power. The scaling of the measured ω_0 is depicted in Fig. 3.8, along with the associated $\sqrt{\mathcal{P}}$ curve for each. For low power measurements of phase-space density we simply scaled the known trap frequencies depicted, making small corrections for trap anharmonicity as well as gravitational sag.

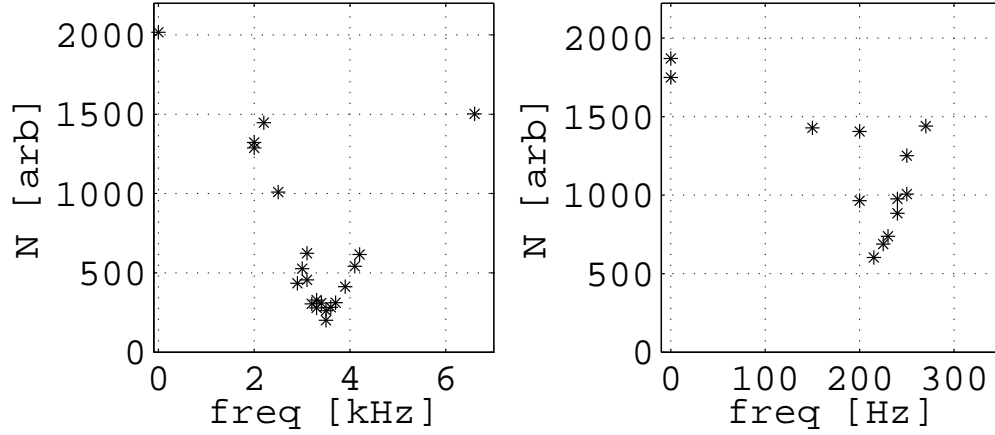


Figure 3.7: Sample trap-frequency resonance data; these graphs represent trap frequencies at laser power of 8.5 W. Standard trap-loading procedure is performed, followed by evaporative cooling to the test power, at which point power is held constant while a fixed number of periods of modulation are applied. The remaining atom number is measured after modulation; zero frequency represents no modulation. The curve at left shows the tight frequency resonance $2\omega_r$, taken with 3000τ of $b = .05$ modulation; the curve at right shows the longitudinal trapping frequency $2\omega_z$, taken with 150τ of $b = .10$ modulation.

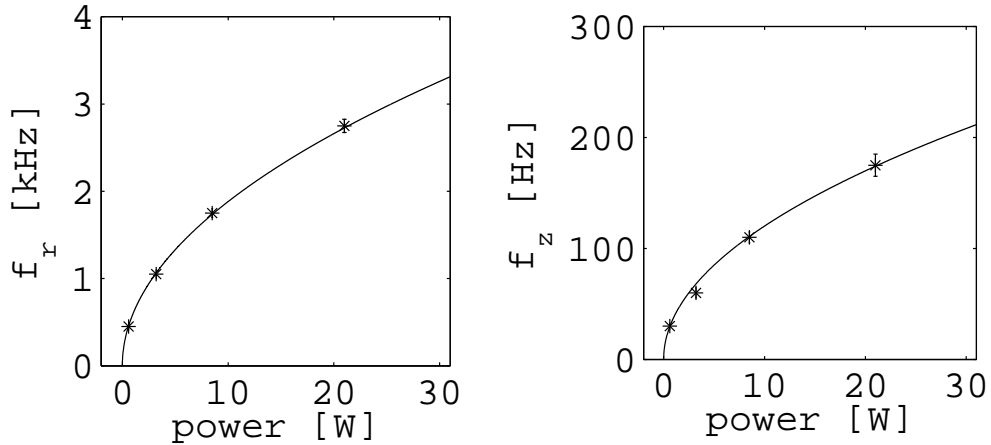


Figure 3.8: Trap frequency scaling vs. power; here we show results of many runs like those depicted in Fig. 3.7. The radial frequency is at left and the longitudinal frequency is at right; the error bars represent judgment of minima location in particular resonance curves. The fits to \sqrt{P} are also depicted. These fits were used to infer phase-space density at powers lower than 500mW where parametric resonance was not an accurate technique. The radial frequency becomes nondegenerate at low powers where gravity begins to significantly affect the trap; this correction is much smaller, however, than the associated correction to expected trap depth.

Pre-correction thermal density and collision rate in the traps were calculated using the following formulae:

$$n(\mathbf{r}) = N \left(m \frac{2\pi\bar{v}^2}{k_B T} \right)^{3/2} \quad (3.2.17)$$

$$\gamma = 8\pi m\sigma\sqrt{2} \frac{N\bar{v}^3}{k_B T} \quad (3.2.18)$$

For example, the typical initial density in the trap is $\sim 4 \times 10^{13} \text{ cm}^{-3}$; the initial collision rate is $\sim 8 \times 10^3 \text{ s}^{-1}$. These startlingly high values are central to the features and interest of this route to BEC; for example, our initial phase-space density here is thus 1.8×10^{-4} , significantly higher than traditional magnetic-trap starting points; the collision rate is a boon as well, allowing initial evaporation rates unthinkable in magnetic-trap experiments.

3.3 First observations of condensation

The path from first optical trapping to observation of BEC was a long and often puzzling one. Broadly stated, we sought to implement an evaporative path that would both exploit the high initial elastic collision rate and avoid inefficient lowering. For a given path, we examined final conditions using estimates of number and temperature and the measured trap frequency vs. power relation, and made essentially *ad hoc* adjustments to the path to reach higher phase-space density. Eliminating systematic errors in N and T played a role, but the largest single contribution to achieving condensation came from various improvements to the experiment that improved the initial conditions as well as the shot-to-shot repeatability.

3.3.1 Free evaporation

The typical result of the loading procedure was a sample of ^{87}Rb atoms in a harmonic potential whose secular frequencies were 3.2 kHz transversely and 220 Hz longitudinally. As discussed above, the earliest we were able to make number and temperature measurements of the trap contents was ~ 100 ms after the shuttering of all resonant light, as well as turnoff of the MOT coils; earlier attempts at profiling were hampered by the presence of untrapped dark-SPOT atoms that had yet to fall away under the influence of gravity. In the intervening time unknown changes occurred in the density and temperature of the trapped cloud. Nevertheless, initial observations revealed typical temperatures of 150 μK and around 2×10^6 atoms, implying densities around $5 \times 10^{13} \text{ cm}^{-3}$. Repeated runs were performed with longer hold times post-loading in order to probe the evolution of the temperature and number. Evidently, free evaporation is a significant factor in the first few seconds of our trap, as the ratio $\eta = U_0/T$ evolves to an effective equilibrium. We speculate that this free evolution is even more important in the first 100 ms of the dark phase, as the trap evolves from being near-equilibrium with the dark SPOT. It is well-known that this free evaporation will stagnate as $e^{-\eta}$, where $\eta = U_0/k_B T$ —in our case this results in equilibrium around $\eta = 12$. Later versions of the experiment had lower CO_2 laser powers available for use, most likely from aging of the laser itself, and lower initial temperatures were observed as a result—in addition, observations showed that initial temperature was proportional to trap depth.

3.3.2 Evaporative paths and gravity correction

It is conventional wisdom in the magnetic trap BEC community that all the finer points of what sort of evaporative path to take (i.e., what the rf-knife frequency vs. time curve should look like) are made irrelevant by the presence of large atom number N and decent vacuum. Since our setup begins with only $1\text{--}2 \times 10^6$ atoms, which is the *final* size of some quasi-pure magnetic trap condensates, significantly

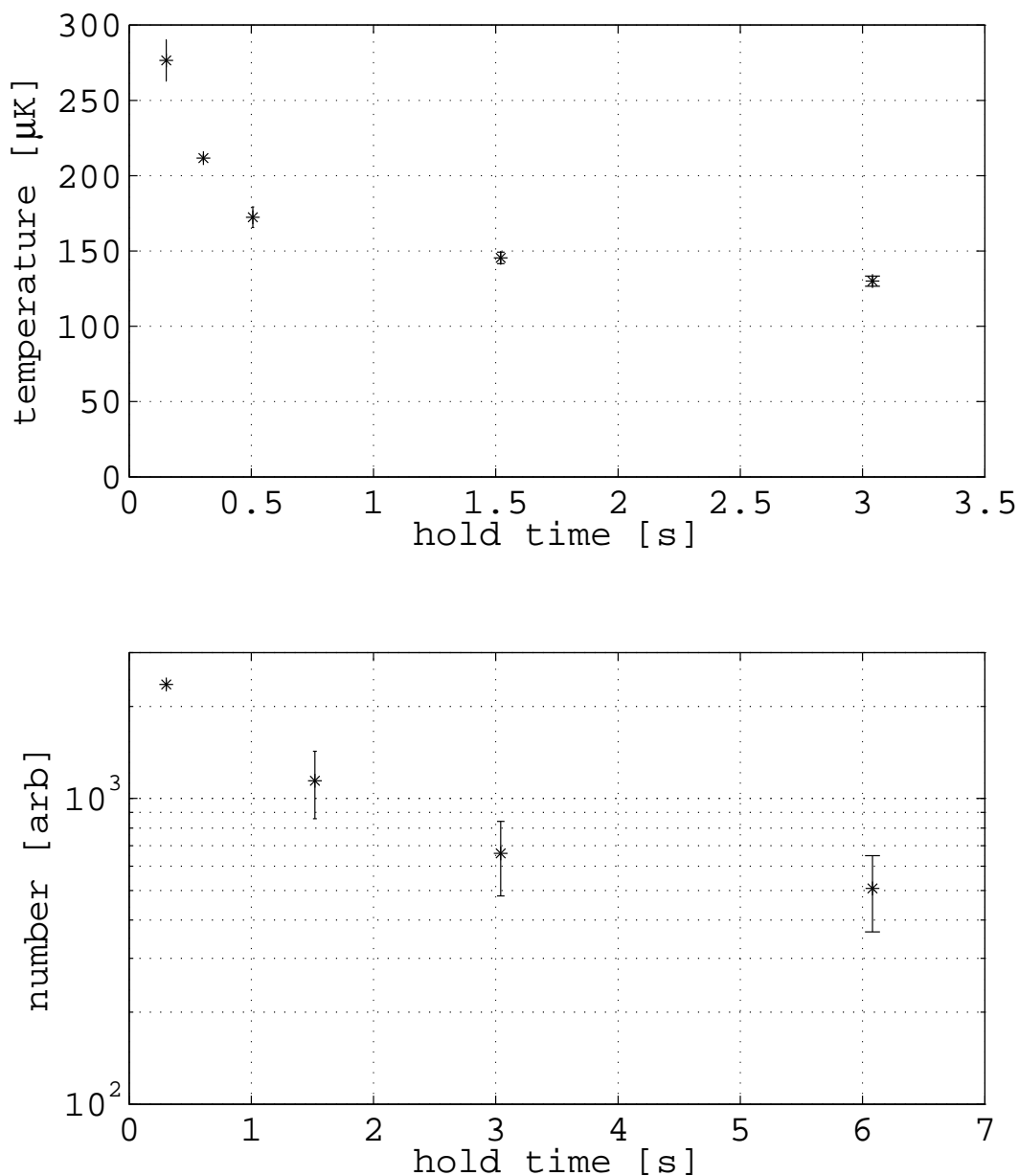


Figure 3.9: *Free evaporation demonstrated via measurements of number and temperature in the dipole trap after a variable hold time at full power (at the time > 40 W). It should be noted that the initial temperatures $> 200\mu\text{K}$ were more typically $\sim 150\mu\text{K}$ in later versions of the experiments chronicled here, due to decreases in available CO_2 laser power. In the upper plot we see free evaporation stagnating over the course of several seconds; in the lower plot, we see number loss correlated with the free evaporation, with the loss rate approaching the background-gas limited lifetime of > 10 s.*

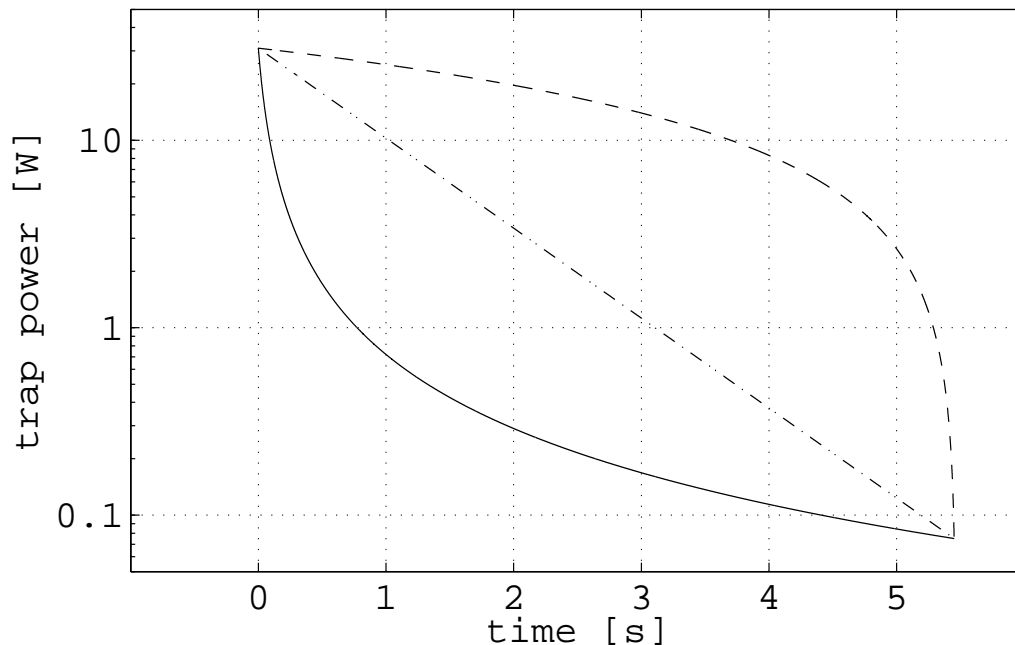


Figure 3.10: *Conceptual depiction of evaporative paths. The uppermost curve is a linear ramp; the middle curve is a simple exponential ramp. Both suffer from the same flaw: they are too slow at the beginning and too fast at the end, squandering the high collision rates available at high power, and not accounting for the drop in trap frequencies at later time. The custom path follows the functional form of Eq. 3.3.3, with $\beta = 1.38$ and $\tau = .07$. The nonlinear mapping of trap depth onto laser power due to gravitational sag is accounted for.*

more care is required to extract the most cooling potential out of the initially dense state and to treat the near-critical period with the care that it demands. Fig. 3.10 depicts three paths: an obviously unsuitable linear ramp of trap depth—proceeding much too slowly early on and much too quickly later on—an exponential path that suffers from a slightly ameliorated version of same problem, and a custom path that is astonishingly fast at first but quite gentle below powers of several W.

The functional form for this custom path was derived for optical traps using the Boltzmann equation [50, 141]. Assuming a time-changing potential of the form $U(\mathbf{r}, t) = U_0(t)g(\mathbf{r})$, where $0 \ll g \ll 1$ and a sample of atoms perpetually at $k_B T = U_0(t)/\eta$, it is shown that the total number of atoms in the trap scales with trap depth

as:

$$\frac{N(t)}{N(0)} = \left(\frac{U(t)}{U(0)} \right)^{\frac{3}{2(\eta'-3)}} \quad (3.3.1)$$

where η' is approximately $\eta + 1$. Thus for $\eta \sim 10$, $N \propto U^{1/5}$. The phase space density ρ scales with number as:

$$\frac{\rho(t)}{\rho(0)} = \left(\frac{N(0)}{N(t)} \right)^{\eta'-4} \quad (3.3.2)$$

implying that for $\eta \sim 10$, $\rho \propto N^{-7} \propto U^{1.3}$. These scaling laws are useful for estimates of the efficacy of a given attempt at condensation and reveal two points worth mentioning. First, a modest decrease in number via ideal evaporative cooling can yield startling increases in phase space density. Given typical starting values for ρ of 10^{-4} , changing the trap depth by a factor of 200 suffices to bring the trap near to degeneracy. Second, as suspected, runaway evaporation is not possible, as the collision rate $\gamma \propto NU^{3/2}/T$ becomes weaker with evaporation, assuming an energy-independent elastic cross section; for $\eta = 10$, $\gamma \propto U^{0.7}$.

Forcing the ratio η to remain constant specifies an evaporative path $U(t)$; this is sensible, as if η grows during evaporation, then one is not proceeding as quickly as one could, and if η becomes smaller, one is evaporating inefficiently. This constraint yields the path:

$$U(t) = U(0) \left(1 + \frac{t}{\tau} \right)^{-\beta} \quad (3.3.3)$$

where β is a number weakly dependent on η and the timescale τ is set by:

$$\frac{1}{\tau} \propto e^{-\eta} \gamma(0) \quad (3.3.4)$$

This timescale is intuitively related to the initial collision rate, as well as the likelihood of trap escape. This formula also requires modification for the presence of a

background loss rate; details for this and other calculations are found in Ref. [50]. It is a function of precisely this form that is found in Fig. 3.10, using $\beta = 1.38$ and $\tau = .07$ s .

An additional factor complicating the creation of the evaporative path is that trap depth in the vertical direction z is affected by the gravitational potential energy z . The consequence of this is that the control voltage \rightarrow rf power \rightarrow laser power \rightarrow trap depth mapping needs to be modified, since the final step is no longer linear. To do this we calculate a correction factor $C(\mathcal{P})$ that represents the trap depth in the vertical direction as compared to the horizontal, or, equivalently, the vertical direction in the absence of gravity. A plot of this ratio is found in Fig. 3.11. Of note is the inability of the trap to support atoms below a power of about 70 mW, necessitating the discarding of any path that recommends weaker confinement. This ratio was essentially used as a lookup table in the conversion of desired trap depth $U(t)$ into laser power. The simplifying assumption was made that evaporative dynamics would not be affected by this gravitational shift in any fashion beyond this mapping, an assumption whose quality will later be shown to be in need of inspection. Evaporative paths made in the absence of this correction proceeded far too fast, as they presumed tighter confinement at any given power than was actually present. At any given power and trap depth we usually desired to calculate the phase space density given an observation of number and temperature. This requires an input of trap frequencies $\omega_i(\mathcal{P})$, of which the vertically oriented one presumably changes more drastically as the trap is weakened. This effect is not significant, however, as the atoms lie far at the bottom of the trap as implied by a value of $\eta > 10$. So while at a laser power \mathcal{P} where the trap depth is half its zero-g value, per Fig. 3.11, the ω_r is corrected by perhaps ten percent. In estimates of ρ this shift was usually taken into account, although as a factor it was much smaller than any related experimental errors.

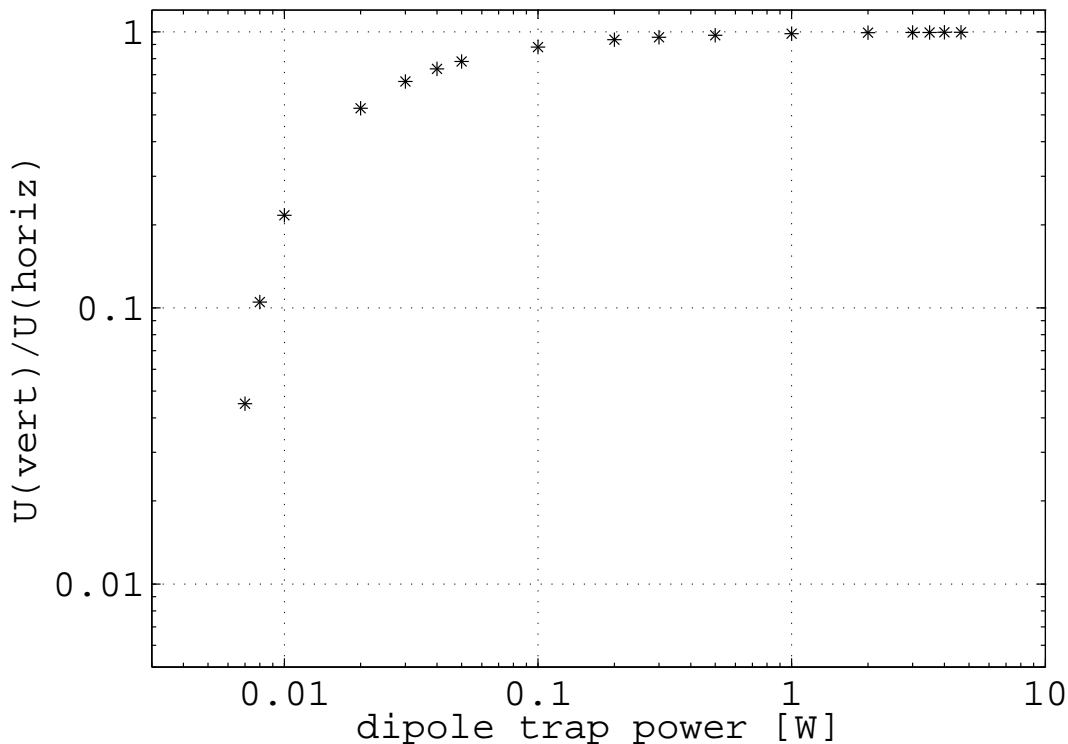


Figure 3.11: Gravity correction for trap depth, represented as a ratio; at a given power, what the trap depth U_0 is versus what it would be without gravity. Thus at high power, the ratio is approximately 1, and at some low power (~ 70 mW), the trap can no longer support atoms against gravity.

3.3.3 Condensation

Interestingly, free evaporation was available as a tool to judge if a given evaporative path proceeded too quickly, i.e., outpaced proper thermalization. Intentionally quick evaporation was used to show this, whereby trap depth was drastically lowered to some small level in less than a second, and then held at that power while the remaining atoms equilibrated. Free evaporation down to $\eta = 12$ was observed in such cases and was absent in properly paced evaporation. This was a subtle effect, however, and cumbersome to employ, and in most cases a path's worthiness was judged relatively, as follows: a series of evaporative runs was made using a particular path, with note made of the typical number and temperature at the end of the run. To adjust the path, rather than creating an entirely new one with slightly different values of β or τ ,

small changes on the mV level were made to the offset control of the AOM driver's AM. Such a change would not have a significant effect on $U(t)$ at high or intermediate powers, but would effectively make the low-power tail a trifle more or less aggressive.

If a path did not appear promising over a significant range of voltage offsets, changes were made to β or τ , or, more frequently, to the duration of the evaporative run. This latter tactic was difficult to express in what it did to the true β or τ of the path, but was efficacious in an intuitive manner. Editing of the path itself to incorporate a larger voltage offset was also used, as doing it too aggressively 'on the fly' technically affected the strength of the trap when it was supposedly turned off for ballistic expansion. Judgment of what constituted 'promising' from run to run was simply a matter of calculating what the new phase-space density achieved was, and whether it was consistent with the power-law increase that was necessary to beat the influences of gravity, background gas, and the inescapable weakening of the trap itself at lower powers.

Our final approach to condensation is illustrated in Fig. 3.12. Several evaporative paths were used at constant path duration, with attendant temperature and ρ calculations. These attempts were followed soon after by our first observation of condensation, depicted in Fig. 3.14. In a profound illustration of the significance of the initial conditions, the series of images depicted were taken using the identical evaporative path, but with significantly drifting initial N . In this case we were lucky to have an upward-drifting N at the time of a well-chosen path. The path at this time was chosen to be a little over seven seconds long; all later condensates (including all work in §4) were achieved using paths around five seconds long.

The emergence of a clear bimodal density distribution was the sign of condensation that had been sought after. Somewhat disconcerting was the absence of a strong asymmetry in the aspect of the cloud, as is traditionally expected for the condensate due to the release of mean-field interaction³. The trap is weak enough at that point,

³This effect was more strikingly observed later, after BEC density and thus mean-field energy had been increased through compression.

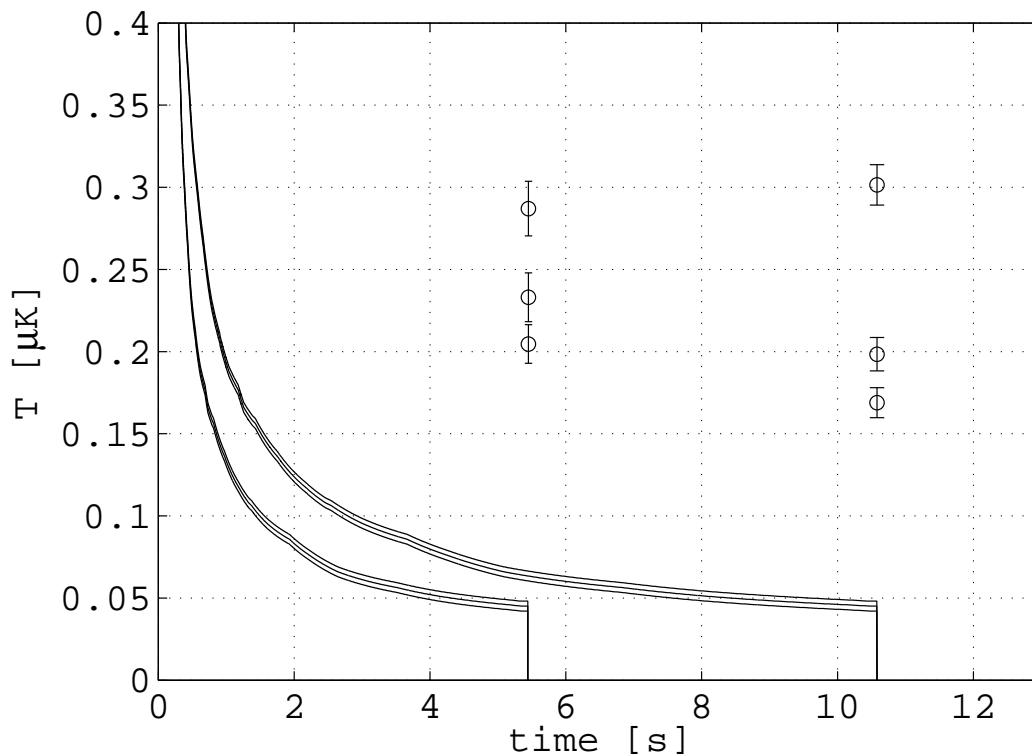


Figure 3.12: *Approaching condensation, with atom number in the range $1.3\text{--}2.4 \times 10^5$. The curves are present for intuitive guidance—they are plots of control voltage, which approximately mirrors laser power and thus trap depth. The three curves at each time are linked to the three temperature measurements at each time.*

however, that even 17.5 ms of ballistic expansion is only expected to yield a 1:1 aspect ratio of the cloud, rather than the strong inversion that a tighter trap would produce.

Absolute notions of condensate number and condensate fraction would require nonlinear fits to the absorption images incorporating both thermal and density profiles:

$$n(\mathbf{r}) = n_{MB}(\mathbf{r}) + n_{TF}(\mathbf{r}) \quad (3.3.5)$$

Signal-to-noise issues with our absorption images prevented these fits from being helpful. Nevertheless, the visually obvious distinction between the behavior of thermal clouds and condensed clouds allowed for evaporation to situations where it was likely that the condensate fraction was $> 50\%$.

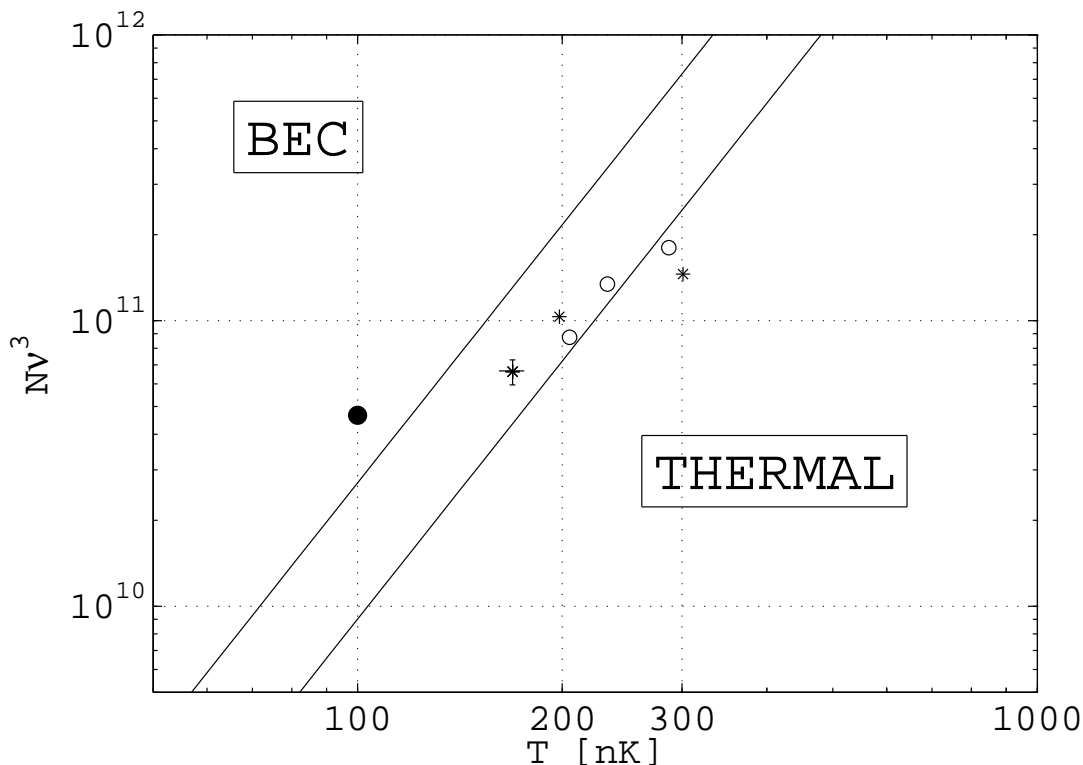


Figure 3.13: A figure representing the path to condensation. The circles represent paths over 5 s; the stars represent paths taken over 10 s. Error bars on the leftmost point are representative of statistical spread. The upper line represents $\rho = 3$, the lower $\rho = 1$. None of the clouds in any of these cases have hints of condensation. The solid dot represents a cloud that we believe was just on the BEC side of the transition, such that run-to-run fluctuations would yield significantly bimodal distributions.

3.4 BEC palette

Figs. 3.15, 3.16, and 3.17 summarize the various types of dipole-trap BECs available to us in the current configuration. Typical evaporation yields a condensate with all three components visible, shown in Fig. 3.15; the ratio of these three populations appears to be a constant of the experiment. It has been speculated that this initial population is set by the particular location of the dipole trap within the MOT reservoir during trap loading [136]. By convention we label the lower left of these three the $m_F = +1$ component and the upper right $m_F = -1$. Determining these accurately would require more knowledge of our MOT coil geometry with respect to trap center

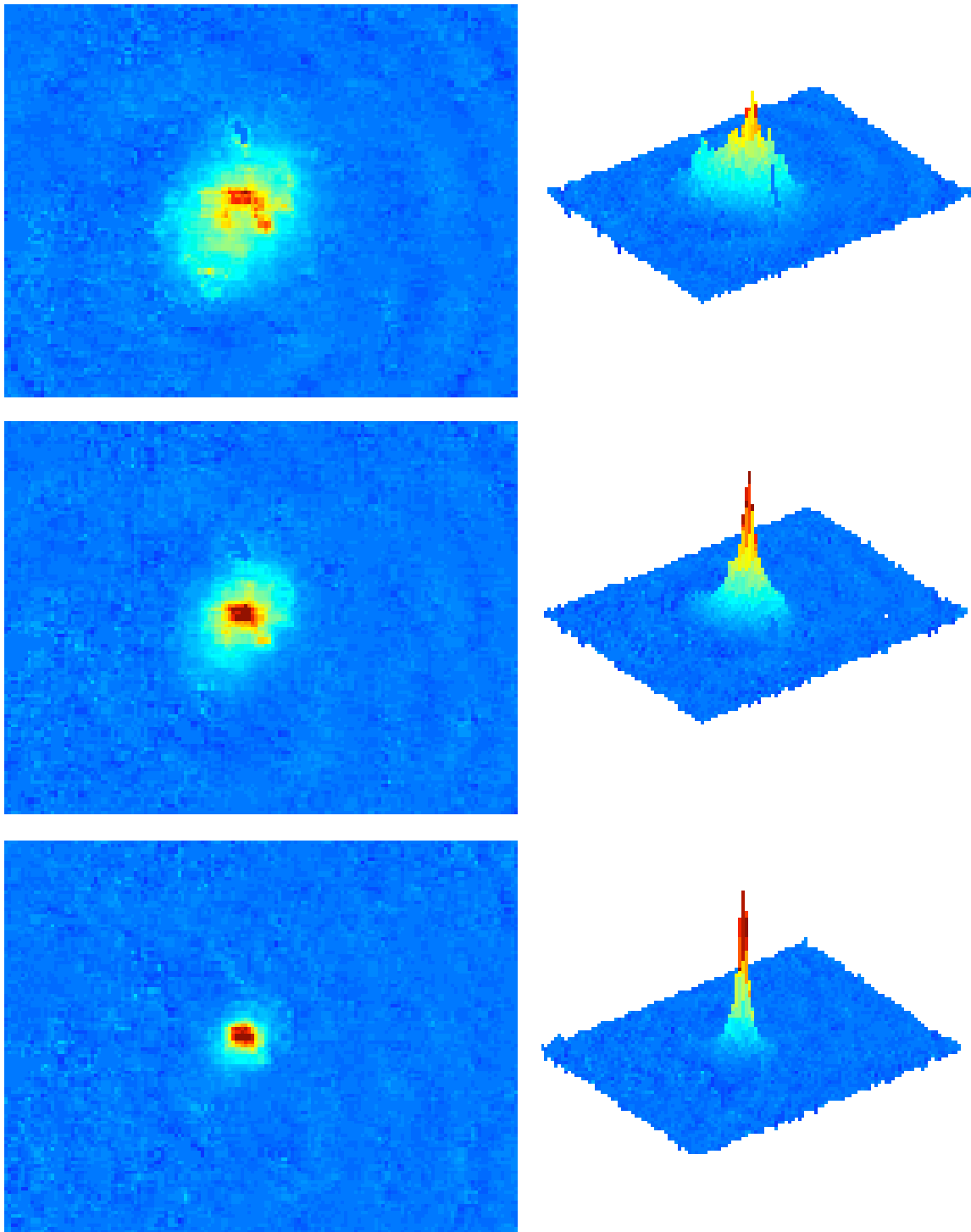


Figure 3.14: *Our first condensate. Total number in each image: $(2.0, 1.2, 0.4) \times 10^5$; images were taken after 17 ms of ballistic expansion. The temperature of the thermal cloud at top is 130 nK. The difference between each image is a slightly deeper cut corresponding to approximately 20 mW of laser power. Images are $450\mu\text{m}$ square.*

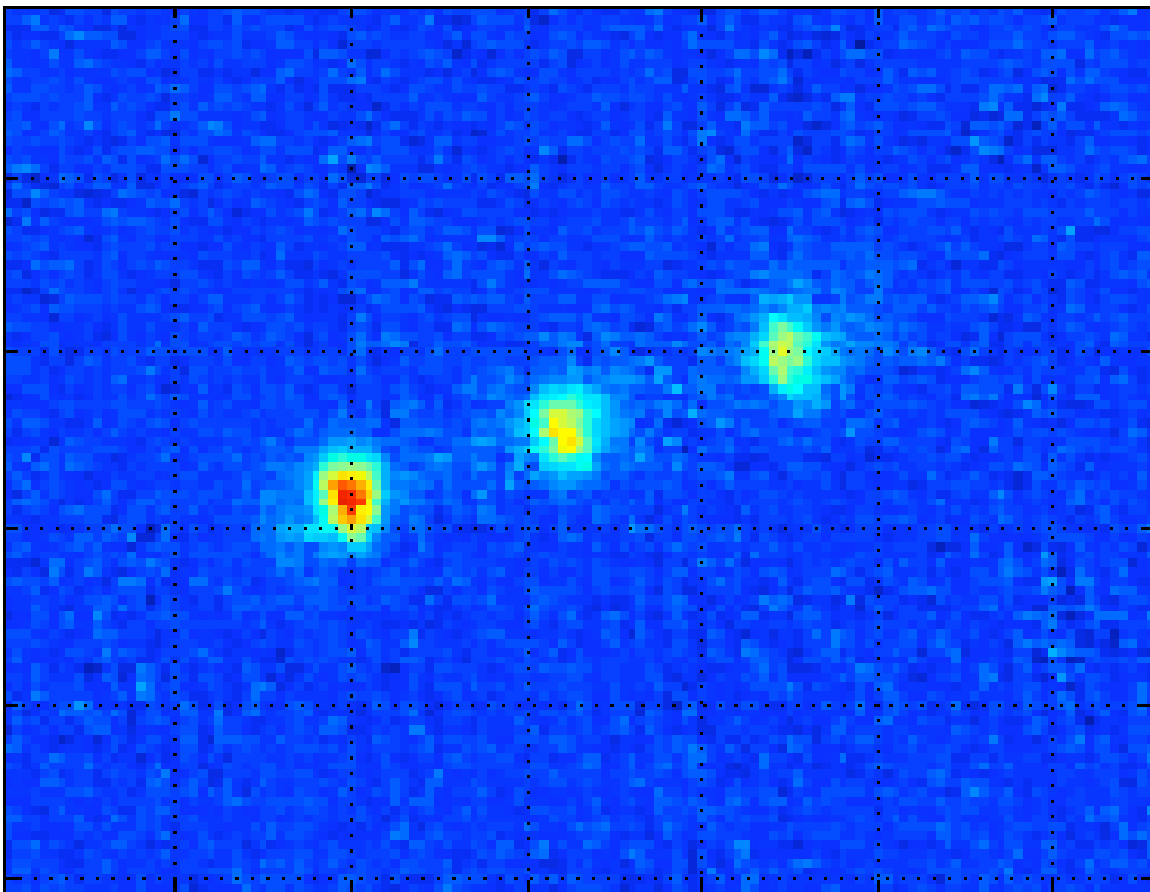


Figure 3.15: *The default spinor nature of our formed condensate, showing $m_F = +1$, $m_F = 0$, and $m_F = -1$ from left to right as revealed by Stern-Gerlach spectroscopy. The field of view is $.63 \times .8$ mm, and the total condensate number is 4×10^4 .*

than we possess; for all our applications it is nothing more than a labeling convention.

Application of a magnetic field gradient along the weak axis of the trap during the first few seconds of evaporation preferentially biases out the $m_F = \pm 1$ components, resulting in a BEC solely occupying the field-insensitive $m_F = 0$ projection, as shown in Fig. 3.16. It should be noted that this process results in nearly the same number of condensed atoms as the gradient-free process, implying a sympathetic cooling process whereby the polarized components remove more than their average share of thermal energy. The ability to create this state is particularly rewarding, as it provides a useful initial condition for studies of spinor dynamics, as detailed in the next section. The gradient applied is simply the MOT field at a particular current.

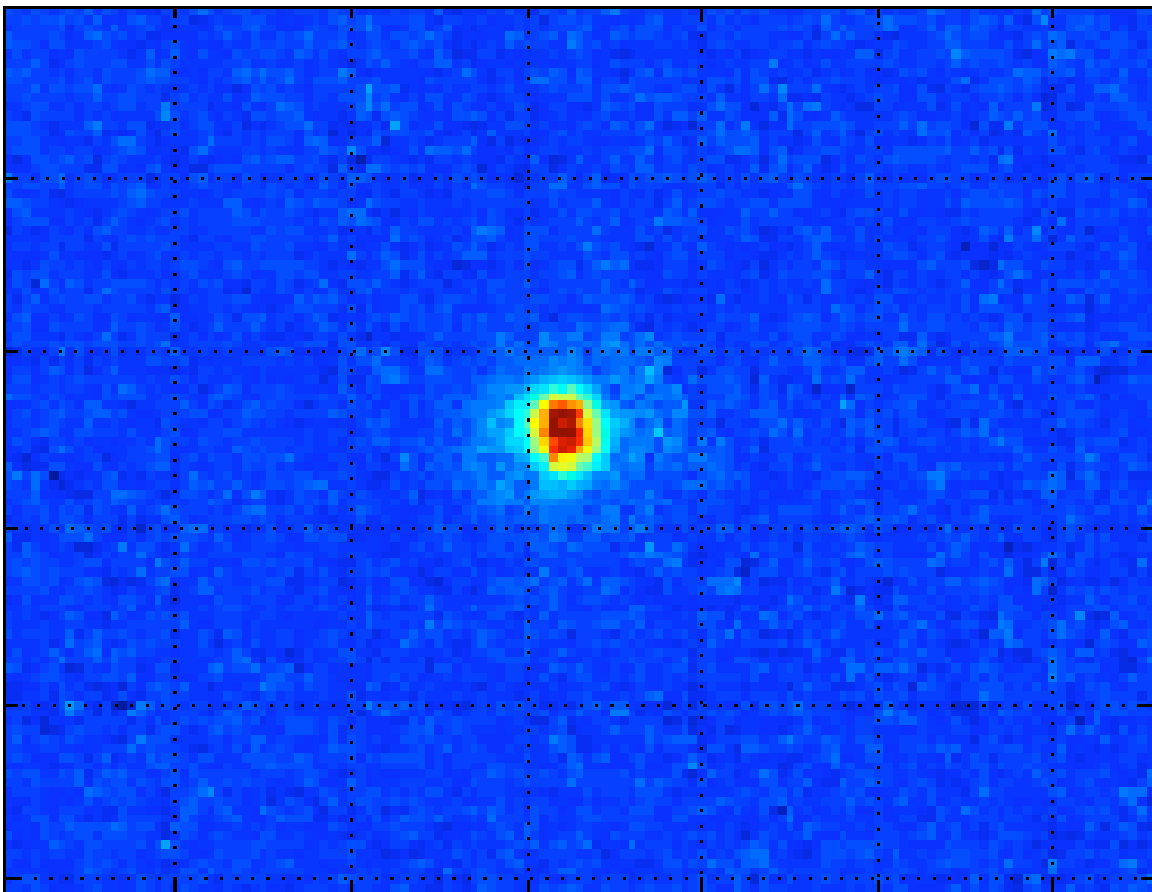


Figure 3.16: *The pure $m_F = 0$ condensate, created by application of a magnetic field gradient along the weak axis of the trap during evaporative cooling. Total condensate number is $N = 3 \times 10^4$.*

3.4.1 The supported condensate

It was noticed that when the current of the applied gradient was significantly lower (and more importantly in a different direction at trap center due to the slightly offset position of the MOT coils), and this gradient was left on throughout evaporation, a condensate would form that was significantly different than previously achieved in our apparatus. As shown in Fig. 3.17, application of a small magnetic field gradient with a component of order a few G/cm in the vertical direction provides a bias for the $m_F = +1$ component. If this supportive gradient is only on for the first few seconds of evaporation, we obtain polarized condensates of number similar to the other options. However, if this gradient is maintained through condensate formation

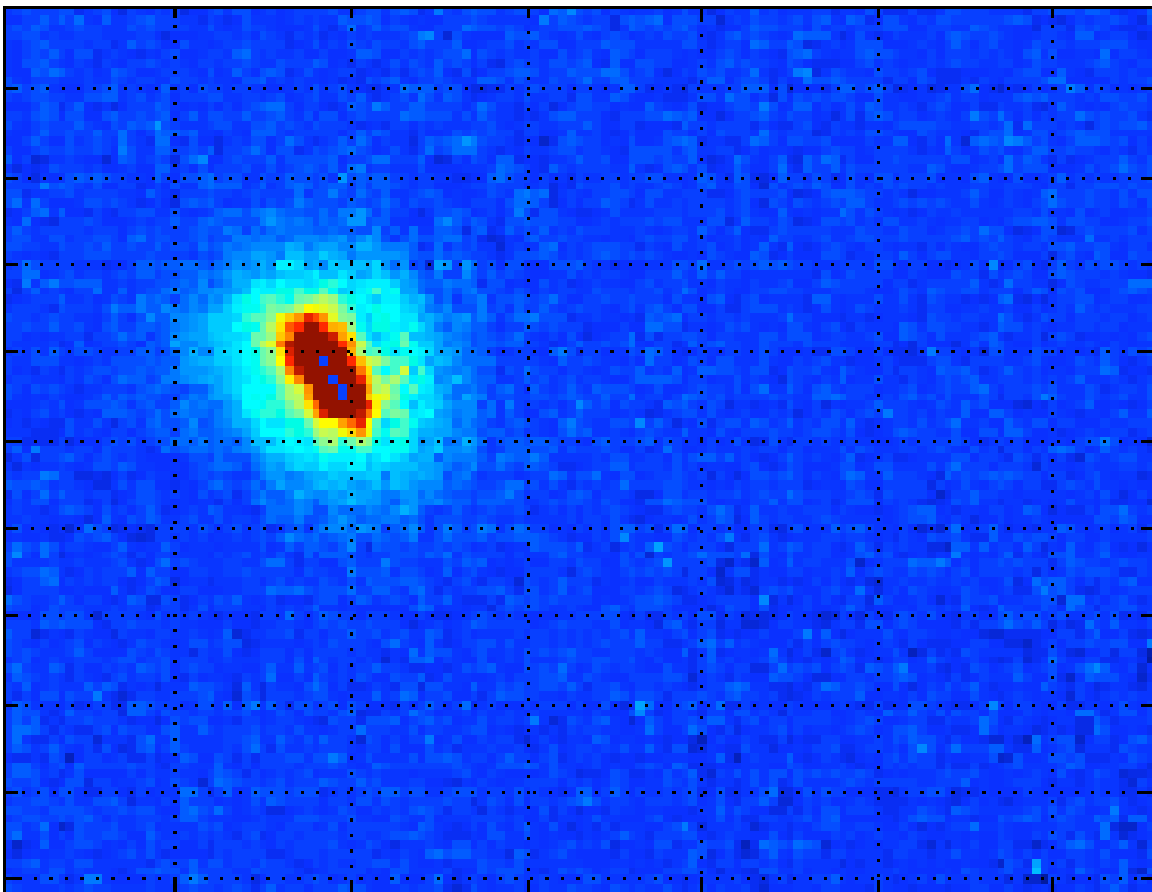


Figure 3.17: The ‘supported’ $m_F = +1$ condensate. A gradient is applied with a significant component in the vertical direction, supporting the evaporating cloud against gravity. Note the shift to the upper left (against gravity) caused by slightly weaker downward force during ballistic expansion. Total number is $N = 10^5$, including a significant thermal fraction.

and through ballistic expansion, we observe significant enhancement in condensate number of order 100%; we attribute this to the fact that the trap depth is strongly perturbed by gravity near criticality (up to 90% of its zero-G value), and even a gradient small with respect to gravity allows for much more efficient near-critical evaporation. This increased number allows better inspection of the phase transition; we see nice growth of the condensate fraction from the thermal cloud in Fig. 3.18. Also of note is the increased aspect ratio of the cloud, indicating higher mean-field energy as one would expect from increased number.

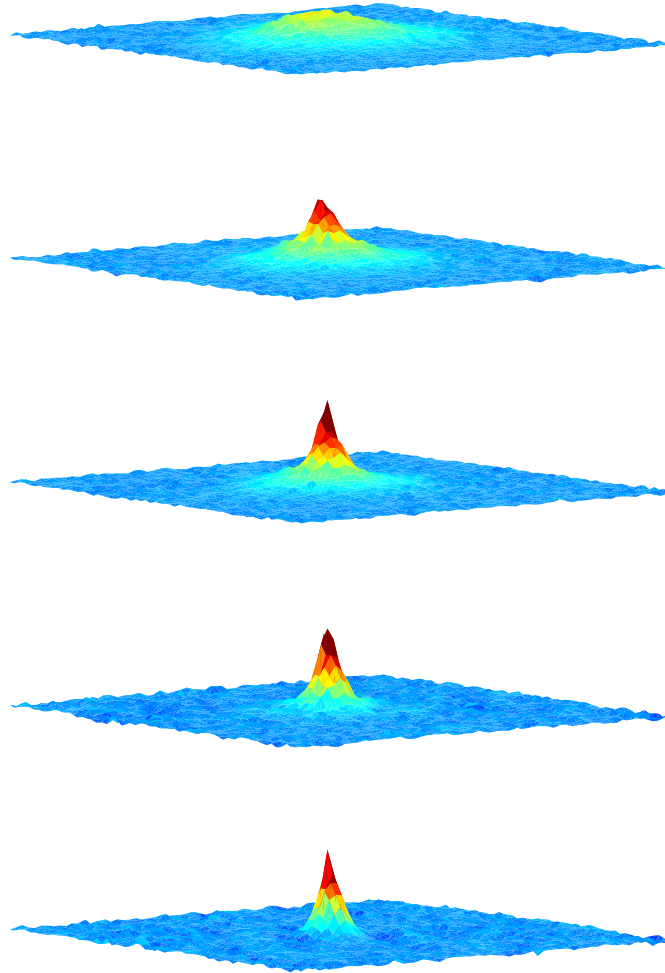


Figure 3.18: *The growth of the supported condensate. The field of view is .4 mm square; the top (thermal cloud) image has $N = 10^5$, and the bottom (mostly pure condensate) has $N = 2 \times 10^4$.*

3.4.2 The downward-directed atom laser

We observe a downward-directed atom laser in the case of the aforementioned ‘supported’ condensate, depicted in Figs. 3.19 and 3.20, outcoupled simply by removing the support in the last few ms before ballistic expansion. This effect is unrelated to the physics of spin mixing or number-correlated dual-beam atom lasers and is essentially analogous to the Tübingen experiment in which the confining optical potential was carefully ramped down in order to ‘leak’ out the condensate [13]. This process is not entirely satisfying in the sense of an atom laser, as there is neither a coherent process converting atoms into outcoupled states nor a pumping process of any kind. It is useful, however, to consider the particularly well-collimated nature of the outcoupled beam and to add this matter-wave manipulation technology to the toolbox of the optically trapped condensate.

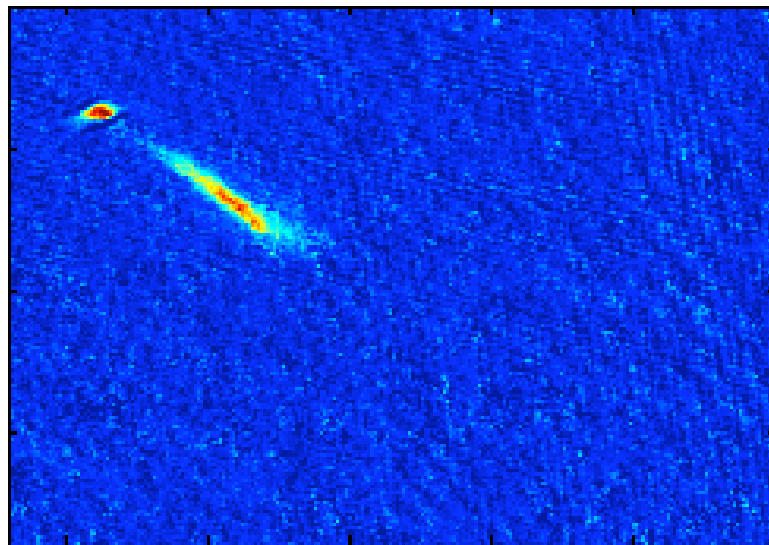
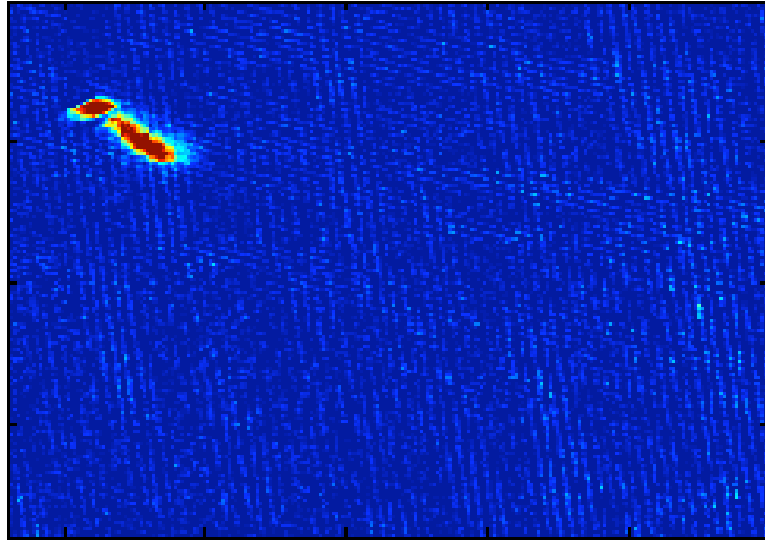


Figure 3.19: *The downward-directed atom laser, part I; at top is 10 ms after outcoupling, at bottom 15 ms. The field of view is 1.2×1.7 mm.*

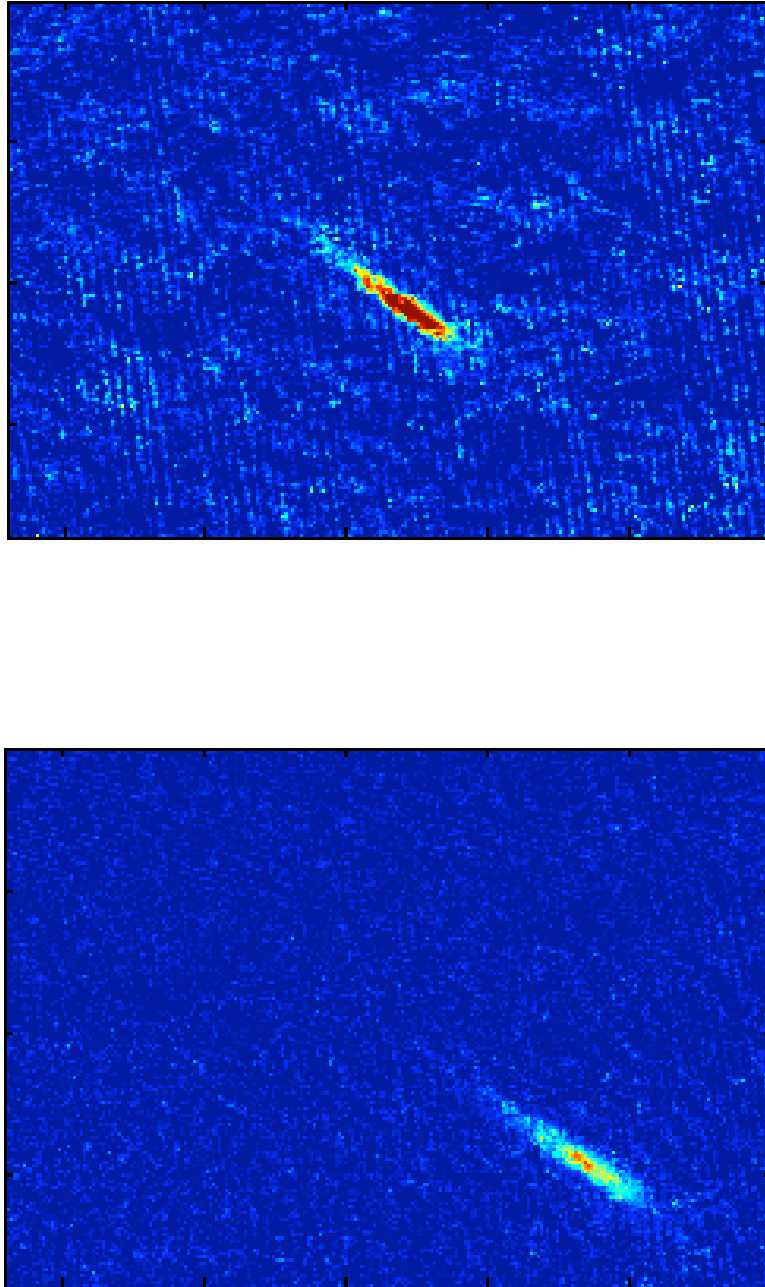


Figure 3.20: *The downward-directed atom laser, part II; at top is 20 ms after outcoupling, at bottom 30 ms. The field of view is 1.2×1.7 mm.*

Chapter 4

Spinor dynamics and the dual-beam atom laser

“The world was young and I was young and the experiment was beautiful. . . These atoms in spatially quantized states—analyze them in one field, turn your focus back, and there it is. Count them! It was wonderful. There I really, really believed in the spin. There are the states—count them!”

ISIDOR ISAAC RABI
John S. Rigden, biographer.

THE CREATION OF AN ALL-OPTICAL CONDENSATE with resulting spinor properties was the first major goal of the research described in this thesis. The second, as documented in this chapter, was the exploration of some of the phenomena made accessible through the liberation of the spin degree of freedom. The dynamics of this new system are quite rich, and the field is quite fast-moving, as documented in §1.4. Here we chronicle some of the efforts made in the past year to illuminate some of the features of the spinor condensate.

4.1 Observations of spin mixing

As detailed in §1.4, an initially out-of-equilibrium spin population will evolve via two-body spin-relaxation collisions (Eq. 1.4.1) to some ground state determined by the

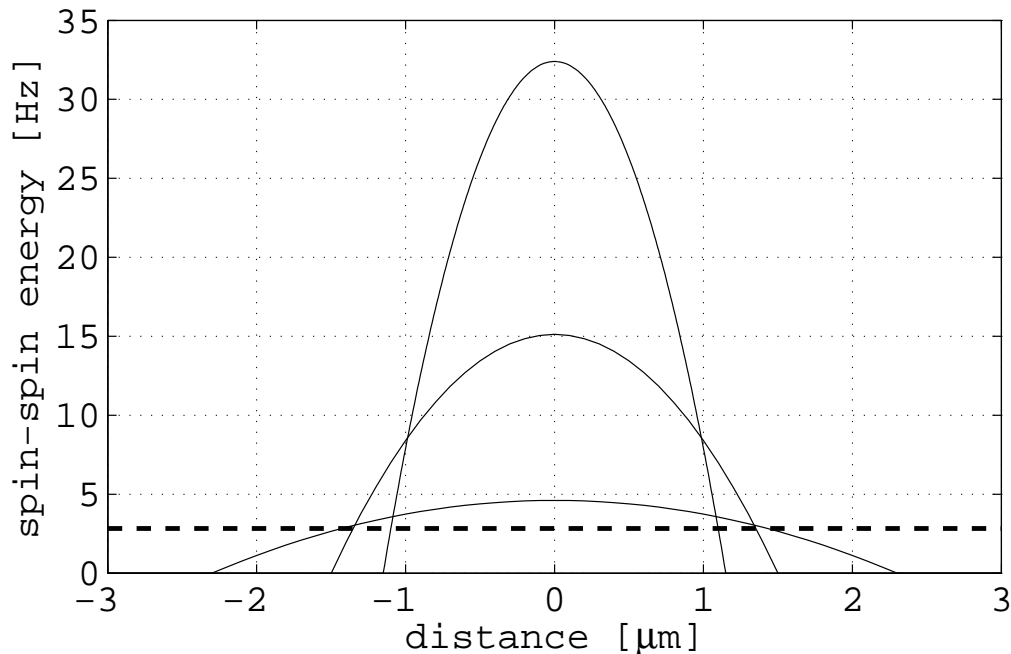


Figure 4.1: *The spin-spin energy scale. The horizontal dashed line represents the typical quadratic Zeeman shift, and the parabolas represent the spin-spin energy scale $2c_2n$. The densities chosen are typical values at a) default power (80 mW) b) 500 mW of adiabatic compression, and c) 1.8 W.*

magnetic field and the conserved magnetization \mathcal{M} . While we made some cursory observations of the evolution of a mixed state at low densities, the majority of the spin-mixing results presented in this thesis were obtained using the technique that revealed spin mixing most clearly, namely adiabatic compression of a pure $m_F = 0$ condensate.

4.1.1 Magnetic field issues

The quadratic Zeeman shift in ^{87}Rb ($F = 1$), 350 Hz/G^2 [78], plays a strong role in the expected spin dynamics in that it sets the energy of the $m_F = \pm 1$ states higher than the planned initial condition for mixing. This implies that if this shift is larger than the spin-spin energy scale the spin-relaxation collision will be energetically forbidden and no departure from the $m_F = 0$ initial state will be observed. This concept is illustrated in more detail in Fig. 4.1.

The experimental situation is complicated by the fact that a naturally well-zeroed field was not desirable for the crucial dipole trap-loading phase; in fact, as discussed in §3, strong fields of at least the size of the earth’s field were required to properly locate the MOT such that a maximum number of atoms were transferred to the dipole trap. We thus arranged for the fields to jump from the loading values to new values after the state-preparation phase of the evaporation had finished, so that the final stages of evaporation, condensation, and later adiabatic compression could all occur at a known (low) field.

Given density estimates for our $m_F = 0$ condensates of $4\text{--}8 \times 10^{13} \text{ cm}^{-3}$, a magnetic field well below 100 mG was desired ($2c_2n \sim 4\text{Hz} \sim \nu_{B^2}$). Absolute zeroing was not desired due to reports of rapid ($< 100 \text{ ms}$) Zeeman sublevel population redistribution due to stray AC magnetic fields at main fields of order 10 mG [78].

To measure magnetic fields we implemented a simple radiofrequency spectroscopy experiment, whereby condensed or near-condensed $m_F = 0$ clouds were exposed to radiation from a simple loop antenna placed outside the vacuum chamber; this occurred after the current values in the bucking coils had been shifted away from the trap-loading values to the low-field values.

The Zeeman resonance of the $|F = 1, m_F = 0, \pm 1\rangle$ manifold is known to be 700 kHz/G [137]; the typical signals sent through the loop through the calibration process were in the range $\omega_{\text{rf}} = 50\text{--}500\text{kHz}$. The measurement itself was a comparison of the fractional population of the various m_F states at the end of runs where ω_{rf} had been applied for the duration of the low-field/final evaporation phase; near resonance, the Stern-Gerlach separation technique would reveal redistribution of the m_F states away from the low-power/off-resonant limit of the pure $m_F = 0$ state. This redistribution was of course a brute-force approach, as the radiation was present for up to a second and the resonance appeared quite power-broadened. We used a HP3325A synthesizer to drive the shorted loop, which while crude by radiofrequency engineering standards was sufficient for our needs. Typical powers used were 30 dBm, although when searching for low magnetic fields lower powers were used in an attempt to reduce

the linewidth of the Zeeman redistribution. The technique yielded final resonance frequencies around 60 kHz, corresponding to a field of around 85 ± 10 mG, with the spread caused by inherent linewidth and signal-to-noise from low atom number. It should be noted that while we were satisfied with this range (due to concern that stray AC magnetic noise would cause trouble at lower fields) further zeroing proved difficult, as the linewidth of the process combined with possible issues with the antenna efficiency appeared to limit the technique's calibration potential. An obviously better path to take would be microwave spectroscopy at 6.8 GHz, which would yield the same observables [78]. This resonance process was repeated several times between spin-mixing experiments—in some cases merely for confirmation, and in others to actively troubleshoot for reasons why spin mixing was not occurring at a particular time, which usually was the fault of the switching electronics. Regardless, even when the fields were totally reset, the 60 kHz resonances were readily achievable.

4.1.2 Density, adiabatic compression, and spin mixing

As shown in §1.1.2, the peak condensate density is determined by the chemical potential, itself found in Eq. 1.1.13, as $n_{c,0} = \mu m / 4\pi \hbar^2 a$. This yields an expression of the peak density in term of the trap frequencies:

$$n_{c,0} = \frac{15^{2/5} \hbar^{4/5} m^{1/5} a^{2/5}}{2} N_c^{2/5} \bar{\omega}^{6/5} \quad (4.1.1)$$

If we wish to increase this peak density, the parameter we have access to is the mean trap frequency, controlled via laser power as $\bar{\omega} \propto \sqrt{\mathcal{P}}$. Thus, more succinctly, we have the simple relation that peak condensate density is simply related to condensate number and trap depth as $n_{c,0} \propto N_c^{2/5} U_0^{2/5}$.

Visually pure $m_F = 0$ states were first created using techniques described in §3. Adiabatic compression was then performed using power-vs.-time paths such as shown in Fig. 4.2. Adiabaticity was ensured through the use of a gentle quadratic

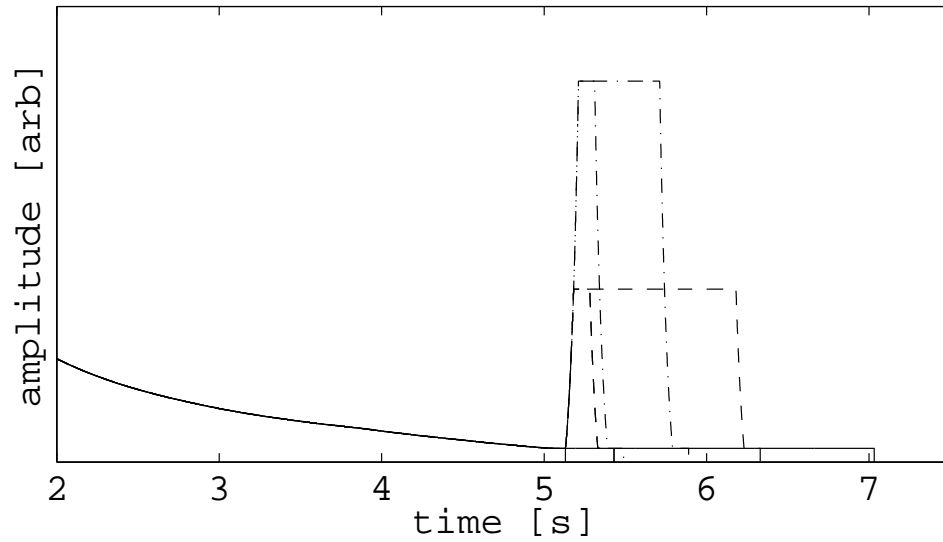


Figure 4.2: Representative adiabatic compression paths, showing compression to 520 mW and 1.8 W. The times illustrated are representative and are correlated with the data points in Fig. 4.4.

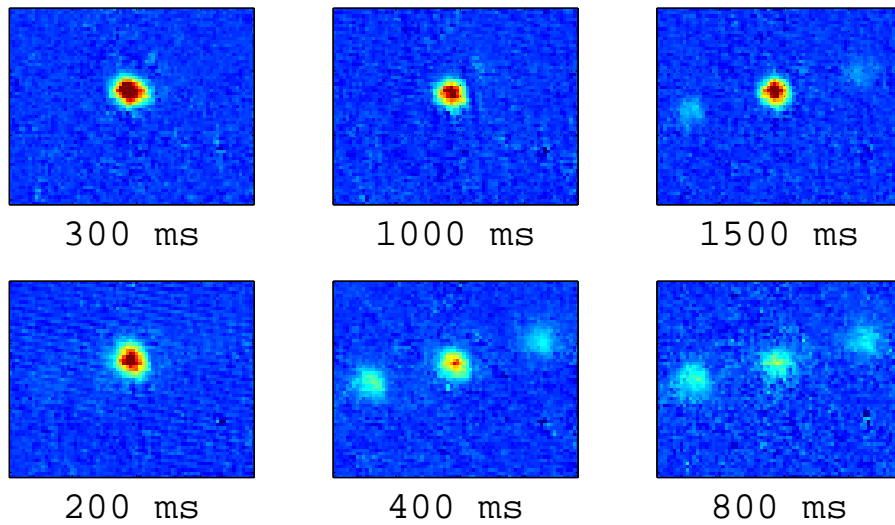


Figure 4.3: Spin mixing as driven by adiabatic compression. The top row has absorption images of an uncompressed $m_F = 0$ BEC evolving for over a second and only barely showing hints of spin mixing. The bottom row is performed at a compression of 520 mW; mixing occurs quite quickly, settling to a steady (fractional) state after several hundred ms.

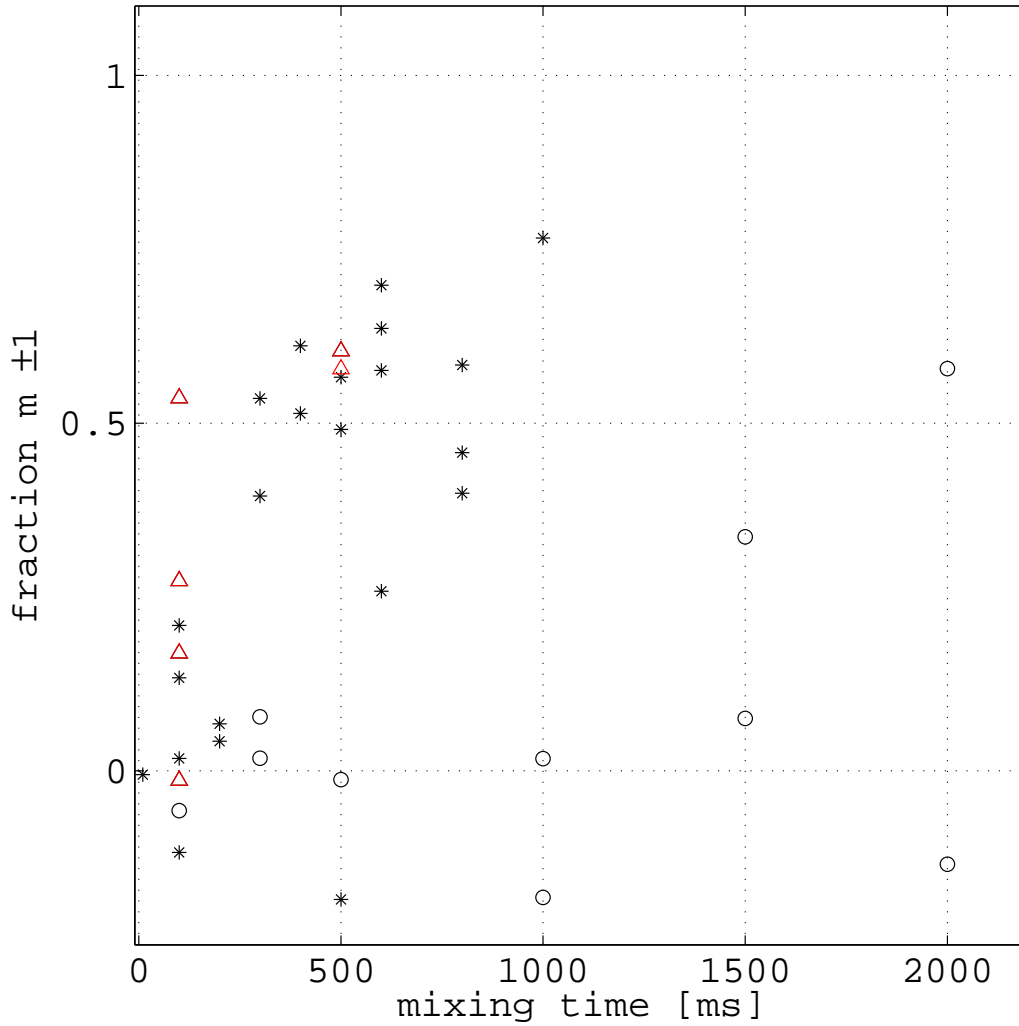


Figure 4.4: Quantitative information about the spin mixing process is depicted here. For three paths (depicted, e.g., in Fig. 4.2) the relative fraction of condensate population in the $m_F = \pm 1$ states at the end of the path is shown. Circles \circ represent the evolution of an uncompressed trap; no evolution occurs at all for at least a second, and when it finally does it is slow to occur. The large shot-to-shot variation was typical for uncompressed traps. Stars $*$ represent the evolution of a trap compressed to 520 mW and show evolution to a 50% steady state in ~ 250 ms. Triangles \triangle show a high-power compression of 1.8 W; steady state is reached very quickly, sometimes as quickly as 100ms. Powers much higher than this suffered from losses caused by three-body recombination.

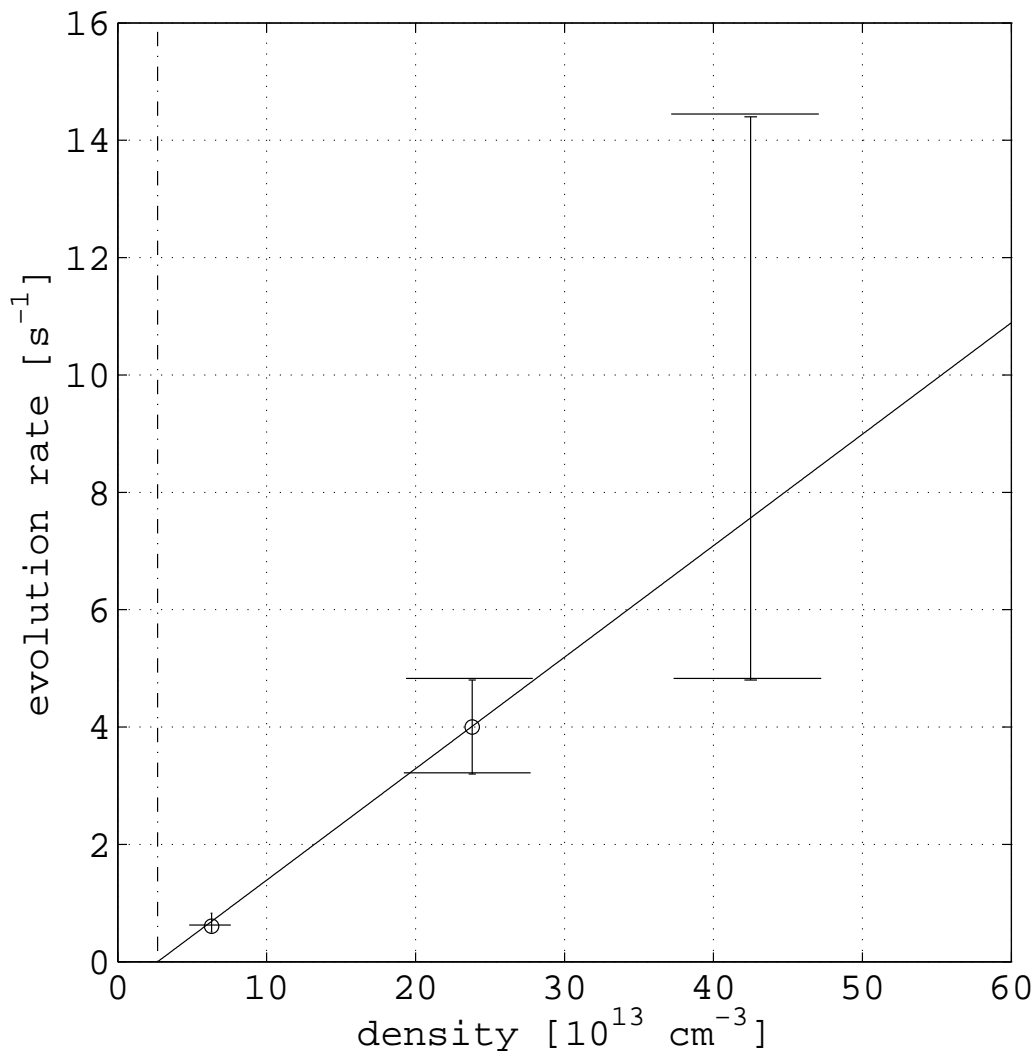


Figure 4.5: Measured spin-mixing rate vs. density. Rates are simple inverses of crudely measured times from Fig. 4.4, picking the approximate time for the cloud to proceed halfway to a steady state. Density measurements represent the average and statistical spread of Thomas-Fermi peak density in all the runs at each compression power in Fig. 4.4. The slope is a direct measurement of the spin-spin energy scale c_2 , and the x-intercept a direct measurement of the quadratic Zeeman shift, which inhibits spin mixing; at that particular density, the spin-spin energy will be insufficient to overcome the quadratic Zeeman shift, and the condensate remains in its initial state of $m_F = 0$. The data are insufficient to firmly establish this intercept, however.

increase in power to the desired value over times up to 100 ms, such that at all times $d\omega_z/dt \ll \omega_z^2$. Once at full power, the trap was held for a variable time up to two seconds before adiabatic decompression and ballistic expansion. The rampdown was necessary mostly as a cosmetic device, as ballistic expansion of the compressed traps yielded violent asymmetric mean-field expansion, which we wished to avoid. The m_F population was determined as before via an applied Stern-Gerlach gradient during ballistic expansion; individual populations were simply determined via the total optical depth in that specific region of the image. The effects of adiabatic compression (and images of mixed condensates) are depicted in Fig. 4.3, which shows relevant absorption images, and Fig. 4.4, which shows the relative fraction of the $m_F = \pm 1$ populations as a function of compression strength and mixing time. Of particular interest is the saturation of the mixing at a fraction of $n_{\pm 1} = n_0 = 50\%$, as predicted in §1.4 for a situation such as this where $\mathcal{M} = 0$. Disappointingly, the oscillations in spin population that we expected to see are not present—the signal-to-noise issues presented by the low condensate number obscure whatever oscillation might be occurring. These issues also obscure the expected correlation effects first observed in 2004 that are so evocative of the entangled nature of the evolved components.

The limits placed on using the compression process to drive spin mixing are placed by three-body recombination. The lifetime of any high-density trap will switch over to a regime dominated by three-body collisions once the density passes a point such that the parameter $K^3 n_0^2$ becomes significant compared to the background-vapor trap loss rate. K^3 is known for both thermal and condensed clouds—we use the values $K_{nc}^3 = 43 \times 10^{-30} \text{ cm}^6/\text{s}$ and $K_c^3 = 5.8 \times 10^{-30} \text{ cm}^6/\text{s}$, the latter being approximately a factor of $3!$ smaller due to the higher-order coherence of Bose-condensed vapor [142]. At a fixed compression time of 100 ms (in addition to the 100 ms taken to adiabatically ramp up) we observe significant loss ($> 50\%$) at powers above 3.5 W, which for typical condensate numbers of 2×10^4 we infer densities of $7 \times 10^{14} \text{ cm}^{-3}$ and three-body loss rates greater than 2×10^4 atoms/s. At normal hold powers of ~ 100 mW the corresponding loss rate is around 10^2 atoms/s. In addition, a spin-mixing experiment

reported in the literature that was performed at $4 \times 10^{14} \text{cm}^{-3}$ in a single optical lattice site made no report of three-body losses; we observe these densities at powers near 1.8 W with no significant loss. At three-body-‘safe’ powers we see a condensate lifetime of greater than 2 s, which, while much less than the background gas lifetime of > 10 s is still more than sufficient to perform any number of experiments.

If we plot estimated values of the spin evolution rate (obtained via crude inspection of Fig. 4.4) versus estimates of peak condensate density, as seen in Fig. 4.5, we observe a slope of $(1.9 \pm .2) \times 10^{-14} \text{cm}^3/\text{s}$, giving only the barest of credence to the high-power point. This slope is an independent measurement of the spin-spin interaction energy scale c_2 , although exactly quantifying the proportionality constant between the essentially arbitrary inverse ‘time’ from Fig. 4.4 and $c_2 n$ would require a detailed understanding of the evolution. Given, though, that the energy of the scale of the system is $c_2 n$, it is satisfying to note that the slope is indeed of order $c_2 = 3.6 \times 10^{-14} \text{cm}^3/\text{s}$. The x-intercept of this graph should reflect the density below which the spin-spin energy is insufficiently strong to overcome the quadratic Zeeman effect at the given field of (80 ± 10) mG, and where no mixing should be observed no matter how long the trap is held. The fit x-intercept is $(5 \pm 2) \times 10^{13} \text{cm}^{-3}$, corresponding to a field of (70 ± 20) mG, which is again satisfactory given our efforts at calibration. The data are obviously insufficient at this point to firmly establish this intercept, however.

These spin-mixing data were taken in order to confirm that the system behaved as expected from the experience of the few other similar experiments. Repeatability issues presumably stemming from high variance in shot-to-shot atom number obscured any oscillations in spin population, yet the general behavior of the system—a tendency to a spin-population equilibrium—was observed. We believe this relatively crude technique is nevertheless a direct measurement of the spin-spin energy scale, which along with coherence measurements in [84] confirm the indirect measurements of c_2 presented elsewhere via studies of the relevant scattering lengths [74, 75].

4.2 The dual-beam atom laser

As discussed in §1.4, the creation of spinor condensates and the prediction of coherent spin mixing stimulated further theoretical discussion regarding the possibility of creating a dual-beam atom laser whereby the $m_F = \pm 1$ components coherently evolved from an $m_F = 0$ initial state are outcouple into ballistic flight. Using the BEC apparatus described here, we implemented a version of this proposal, depicted in Fig. 4.6 and explained here.

Given an $m_F = 0$ condensate, we drove spin mixing using a long pulse (typically 800ms) of 520 mW compression—long enough such that saturation of the spin-mixing process into the approximate ground state $n_0 = 0.5$ would have occurred. We then adiabatically decompressed and held the trap at constant (low) power, such that all three components coexisted in a very shallow optical potential; at this point the spin populations were ‘frozen’ at their new values. We then implemented magnetic outcoupling, similar in principle to the downward-directed atom laser, but applied to a multi-state condensate in a state-selective fashion. Field gradients were applied nonadiabatically in order to distort the trapping potential and provide a velocity kick for spin-polarized atoms to escape. The gradient alone in some cases was tilted enough such that escape would have happened regardless of turn-on speed, but quick turn-on allowed us to ensure escape over a wide range of gradients. Fig. 4.7 illustrates a typical run; here, a magnetic field gradient dominantly directed along the weak axis of the optical trap (toward the upper right) is turned on quickly (over several ms) at a variable delay (5-50 ms) before the optical trap is turned off. In this case ballistic expansion is limited to a minimum time of 100 μs (nonzero so as to allow for optical pumping) and is thus effectively *in situ*. This outcoupling is not quite as ambitious as that of the original proposals [102, 103], but is an important first step. What one has, then, is two samples of Bose-condensed atoms correlated to each other propagating separately of one another, a situation we refer to as the dual-beam spinor dynamics-driven atom laser.

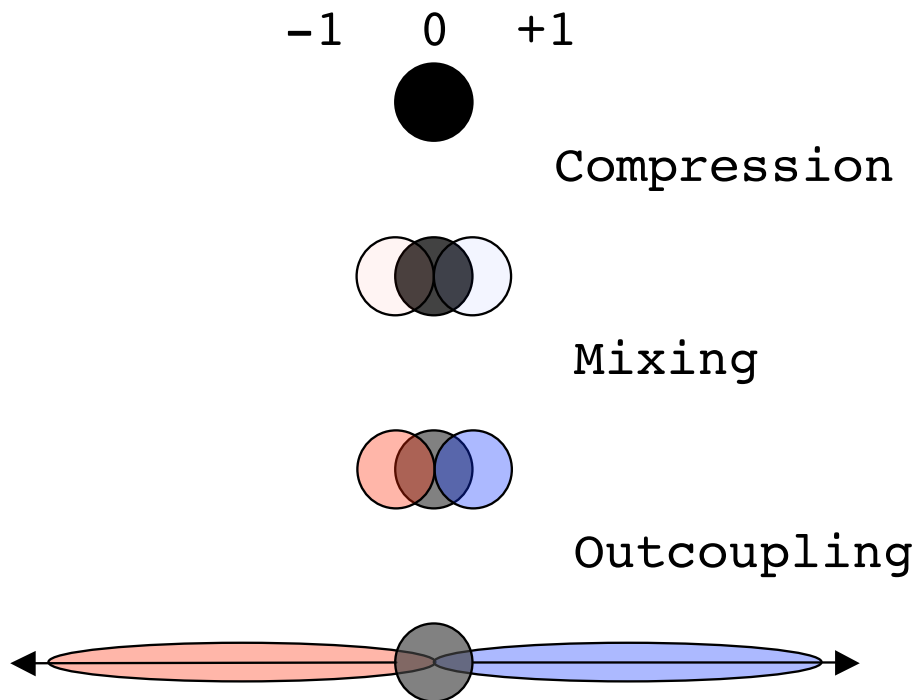


Figure 4.6: *The proposed scheme for a novel atom laser. We begin with a properly prepared initial condition of a pure $m_F = 0$ condensate. We then adiabatically compress to drive coherent spin mixing, settling at a ground state of approximately $n_0 = 0.5$. Outcoupling gradients are then applied, resulting in the $m_F = \pm 1$ components being released from the optical potential along the long axis of the trap. These number-correlated beams then propagate oppositely away from the trap due to the opposite sign of their respective magnetic moments.*

4.2.1 Varieties

Using slightly different velocity kicks (implemented through magnitude of the turn-on gradients) we observe several variants of the dual-beam atom laser. Most commonly, we observe immediate outcoupling and ballistic flight of the $m_F = -1$ component while the $m_F = +1$ component first propagates in the opposite direction (as expected), reverses its motion, passes through the parent $m_F = 0$ condensate, and finally escapes, as depicted in Fig. 4.7. It is this asymmetry between m -state behavior that prevents usage of the perhaps more tantalizing phrase ‘twin-beam.’ With greater velocity kicks, we also observe the more intuitive case of both polarized com-

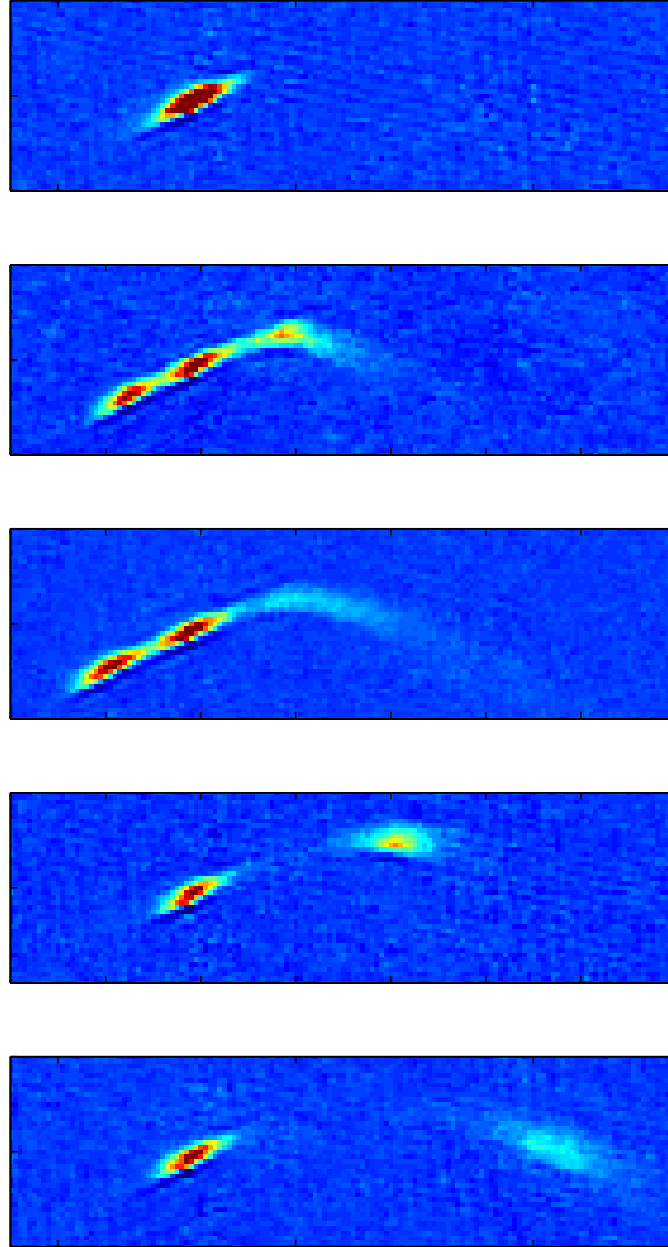


Figure 4.7: A typical outcoupling run of the spinor dynamics-driven dual beam atom laser. a) 0 ms: the full condensate, in situ. b) + 20 ms: soon after outcoupling. The $m_F = -1$ component (at right) immediately passes beyond the reach of the dipole trap and experiences ballistic flight and mean-field expansion. The $m_F = +1$ component remains confined in an effective guide and travels in the opposite direction. c) +25 ms: the $m_F = -1$ beam continues to propagate while the $m_F = +1$ beam is turned around and returned toward the origin. d) +45 ms: the $m_F = +1$ beam now falls freely and experiences mean-field expansion, like the $m_F = -1$ component before it. Note a slightly different path than $m_F = -1$. e) +50 ms: continued $m_F = +1$ propagation; note that the $m_F = -1$ component has traveled out of the field of view by this point. Images are $.38 \times .88$ mm; gravity is directed toward the lower right, and the trapping laser is directed toward the upper right.

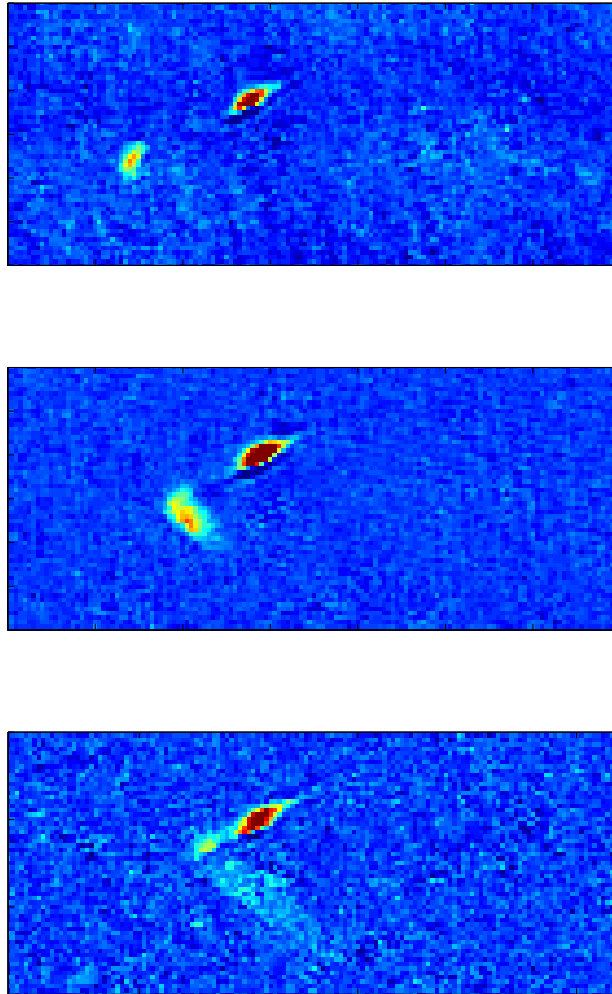


Figure 4.8: *Several other varieties of the dual-beam atom laser. In all three of the above pictures the $m_F = -1$ component has departed to the right already. At top we observe the $m_F = +1$ component traveling relatively far from trap center. At middle we observe the same component making a sharp turn and propagating downwards. At bottom we observe the interesting phenomenon of partial outcoupling; one can think of the gradient as being only partially sufficient to tilt the potential enough such that the entire condensate escapes—the energy scale of the condensate being the chemical potential μ . The field of view is $.38 \times .88$ mm.*

ponents escaping into ballistic flight from opposite ends of the cigar-shaped trap. Rarely, we observe partial exit of an evolved fraction due to insufficient magnetic field tilt compared to the condensate chemical potential μ , which illustrates the fine control of output coupling possible using this scheme. Both of these variants are depicted in Fig. 4.8. Slight deviation from true horizontal of the trap itself is also assumed to bias the exit paths of the evolved components.

4.2.2 Modeling

The immediate broadening of the outcoupled spinor atom laser pulse compared to the downward-directed one is perhaps counterintuitive, but can be explained in terms of the nature of the condensate and the path it takes via the long axis of the trap, rather than the more traditional transverse outcoupling. The horizontally outcoupled beam experiences preferred mean-field expansion perpendicular to the direction of travel, and thus does not exhibit the tight collimation characteristic of our downward-directed $m_F = +1$ pulse, which is also characteristic of other typical atom lasers. We have duplicated this new behavior using simple simulations combining center-of-mass motion and standard mean-field expansion theory. Fig. 4.9 shows a simple simulation combining mean-field expansion and center-of-mass motion of an outcoupled condensate. Notable is the preservation of condensate tightness until it escapes the optical trap. It then begins to expand radially, perpendicular to the direction of its motion. This is similar to the behavior of the outcoupled fractions in the observation runs. Of course, in the experiment the condensate is not expelled all at once; ideally there is a finite time gradient ramping that results in an atom laser ‘beam,’ hints of which were indeed seen, rather than a single cloud. The turnoff of trap tightness that the expelled BEC ‘sees’ is quite quick and is approximated in the simulation as adiabatic only down to about half the initial trap frequency. Fig. 4.10 shows the center-of-mass motion taken in the outcoupling potential seen by the $m_F = \pm 1$ states. Counterintuitive behavior is explained by initial velocity kicks provided by nonadiabatic turn-on of the fields; we select arbitrary initial velocity kicks (of order a few cm/s) to du-

plicate the observed behavior in the simulation. These pictures are not intended as exact replicas of the physical situation; rather, they should help provide a guide to what is going on in the experiment. The similarities between Figs. 4.7 and 4.8 and the simulation pictures are quite promising, in that the broadening behavior and the occasional sharp turn are duplicated.

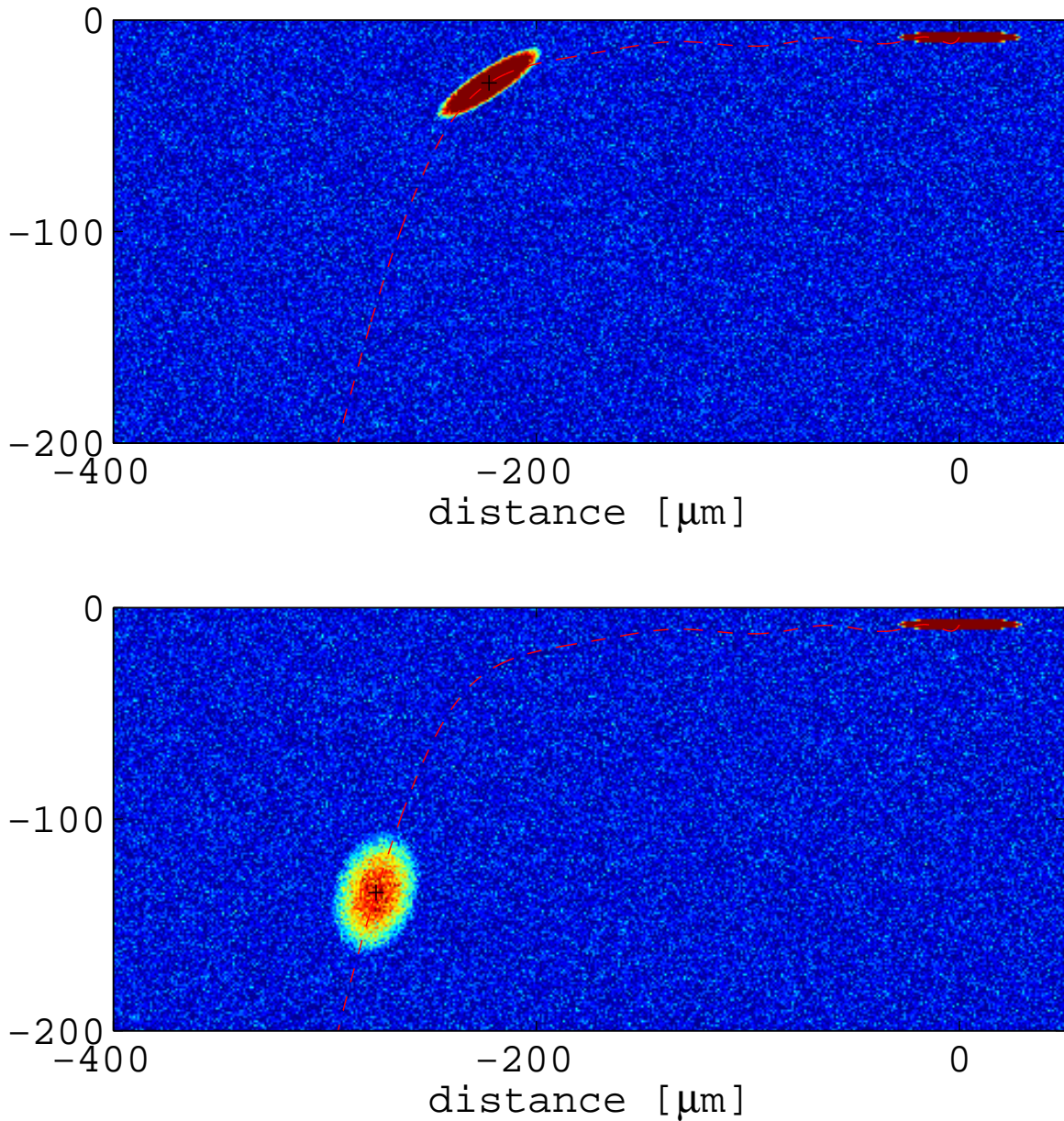


Figure 4.9: Modeling outcoupling and mean-field expansion. The displayed clouds show the asymmetric mean-field expansion of an outcoupled condensate component. The top picture is 28 ms after the application of outcoupling gradients, the bottom after 34ms. What is notable is the relatively slow escape from the optical trap region compared to the rapid flight away, once out. Nevertheless, mean-field energy causes significant spread perpendicular to the motion, duplicating the spreads seen in Fig. 4.7.

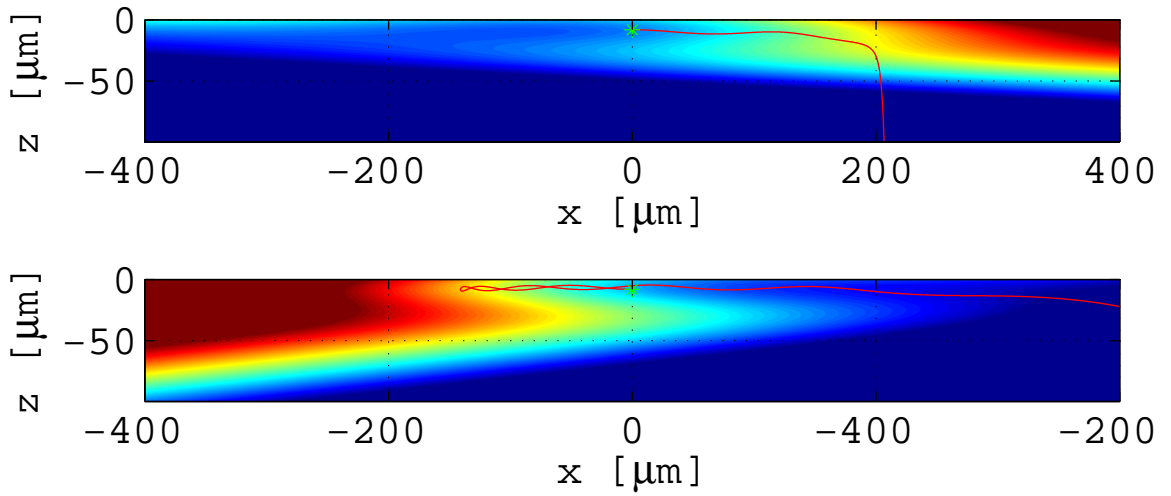


Figure 4.10: *The motion of $m_F = \pm 1$ condensates in the outcoupling potential. At top, an initial velocity kick propels the cloud up the local potential and over the hill, out of the optical trap region and then down. At bottom, the velocity kick (in the opposite direction) results in a reversal of motion. These velocity kicks were chosen to qualitatively match Fig. 4.7; of note are the sharp turn taken by the top cloud and the significantly different exit path taken by the bottom cloud. The potential was taken with applied gradients of 5 G/cm in the vertical (z) direction and 2.2 G/cm in the horizontal/beam direction x . The velocity kicks chosen were of order 2 cm/s, and the colormap represents an energy change of 6 μ K, with red being high.*

Concluding Remarks

When they were thus met, happy was the Man that could find out a new Star in the Firmament; discover a wry Step in the Sun's Progress; assign a new Reason for the Spots of the Moon. . . or, indeed, impart any crooked Secret to the learned Society, that might puzzle their Brains, and disturb their Rest for a Month afterwards, in consulting upon their Pillows how to straiten the Project, that it might appear upright to the Eye of Reason, and the knotty Difficulty to be rectify'd, as to bring Honour to themselves, and Advantage to the Public.

EDWARD 'NED' WARD
The Virtuoso's Club.

SPINOR DYNAMICS IN OPTICALLY TRAPPED BEC is a very young field of inquiry. When the research described in this thesis was initiated, the only relevant experimental work was the study of spinor dynamics in sodium at MIT and the creation of the first all-optical condensate in rubidium at Georgia Tech. Now, five years later, there are ~ 10 groups worldwide explicitly studying spinor dynamics or (more generally) BEC in optical traps, and even more just now switching or developing the capability. Given the fast growth of the field and the current excitement about the future, in this section I would like to discuss the current status of our experiment and what possibly lies ahead.

In many respects the work on this experiment has just begun. A major milestone was reached in the creation of the condensate itself; all-optical condensation was completely novel at the inception of this thesis work, and we were among the

first few to achieve it. We have accomplished a proof-of-principle of dual atom lasers generated by spinor dynamics and shown that we have precise control over the rate of spin dynamics. These results are tantalizing in that they represent the first significant steps to the realization of long-standing proposals—the generation of twin number-correlated/massively entangled/squeezed atom lasers. Given that we have shown that we can not only control the coherent conversion of pairs of $m_F = 0$ into the correlated pair $m_F = \pm 1$, the next step is to measure this correlation. Hints of this behavior were observed in [78], whereby the fluctuations in the relative populations n_{\pm} were suppressed compared to the shot-to-shot individual species jitter. Doing this with significantly propagated atom lasers would be the next logical step. One could also imagine capturing the outcoupled atoms using adjacent dipole traps, or performing the experiment with a dipole trap at 1560 nm, where the Rayleigh range for a given trap depth would be much longer, allowing waveguide-like propagation. An obvious difference between our setup and the 2000 proposals is that our outcoupling is state-dependent; the $m_F = +1$ beam propagates differently than the $m_F = -1$ beam. The original proposal suggested an outcoupling scheme that sent the atoms in opposite (but unknown) directions through the use of a not-so-far off-resonant dipole trap that lowered the energy of the $m_F = \pm 1$ states equally such that conservation of energy forced them to escape the (quasi-one-dimensional) trap. Current magnetic-gradient outcoupling will preserve the number correlations between the two outcoupled populations, but creation of a true massive matter-wave EPR pair will require a state-ignorant process. Given this abundance of possibilities and apparent routes, it should be made clear that this thesis is presented at a logical pause in the development of this line of research, as the limits of the first-generation apparatus in terms of condensate number and repeatability have become apparent.

The central challenge emerging from the original creation of all-optical BEC was that of increasing condensate size from $N \sim 10^4$ to levels that permitted more flexibility and experimental ambition. What has become clear over the last several years is that a single- or crossed-beam setup, static in the sense of a fixed beam waist and trap

depth and directly loaded from a dark MOT, has a maximum loading capability in the several millions, which is too low if large condensates are to be obtained. While large numbers are not absolutely necessary for the study of condensate physics (as demonstrated in this thesis), they make it much easier to observe more delicate effects with an imaging system of particular signal-to-noise (also a path of improvement). This large-number barrier has been breached by several groups, and the author hopes that the next generation of this experiment will incorporate some version of these ideas. The general idea is that of dynamic trap volume. The trap-loading period requires as large a trap volume as possible consistent with the ability of the loading process to cool atoms into the conservative potential, yet efficient evaporation and the eventual onset of degeneracy require much tighter traps. The best of both worlds can simply be achieved through the use of a ‘zoom’ lens—moving the external telescope in real time such that the waist of the focused CO₂ laser becomes significantly smaller [78]. Trap depth scales as the square of this waist, so this process obviously cannot be used to generate arbitrarily large volumes; the limiting factor again is the trap depth into which the precooling stage (in our case, a detuned dark SPOT) would be able to place atoms. A more complicated path involving dynamic trap volume involves a crossed-beam trap. ‘Zooming’ is efficiently accomplished by starting the trap with the two beams overlapped, but not at their individual waists. Overlap of the beams is effected at up to several Rayleigh lengths away from center, providing a large trap volume for loading. The beams are then translated perpendicularly to their pointing direction such that the trap center becomes waist-on-waist; this provides the requisite tightening. Techniques such as this can be complemented by more exotic precooling stages, such as far-off resonant optical lattices [14]. It is also possible to generate large trap volume by using a so-called optical TOP trap, whereby a rapidly orbiting optical potential is created through the frequency modulation of the controlling AOM—angle deviations in the trapping beam before focusing yield a quickly oscillating spatial profile of the trap itself. High-amplitude modulation, then, is correlated with large trap volume [143].

Other avenues of investigation have recently become apparent. First, the so-called ‘clock transition’ in ^{87}Rb , $|F = 1, m_F = 0\rangle \rightarrow |F = 2, m_F = 0\rangle$, is available in all-optical condensates due to the spin-independent nature of the trapping potential. Atomic clocks operating on this transition are limited by the velocity spread of the test sample, namely laser-cooled clouds in atomic fountains. The extremely low residual energy of a BEC makes it seemingly an ideal testbed. However, this is made difficult by the high density of BEC; atomic clocks using laser-cooled atoms prefer to operate in as low a density regime as possible, due to a shift in resonance frequency proportional to density. Nevertheless, the possibility suggests the need for at least preliminary investigation, which to the author’s knowledge has only been performed using a ^{87}Rb clock-like transition in a magnetic trap. The clock-transition collision shift in a sodium BEC was measured in sodium in 2003 [144]; such an experiment should be within the reach of our present capabilities.

Secondly, the ability to control the interactions between individual atoms has become easily variable in recent years due to the tuning capability of Feshbach resonances in the interatomic collision channels. While magnetically trapped ^{87}Rb has not been found to possess any resonances, optical traps have opened up a new set of resonances: over 40 were measured in the $|F = 1, m_F = +1\rangle$ spin channel [145], and a low-field resonance in the mixed spin channel $|F = 1, m_F = -1\rangle \rightarrow |F = 2, m_F = -1\rangle$ [146] was found in 2004. The use of these resonances to tune the ^{87}Rb interaction energy in real time is an interesting tool that bears exploration.

A notable feature of our dual-beam correlated atom laser scheme that in principle it can be turned into a quasi-continuous source of correlated matter waves. Since not all of the initial reservoir of $m_F = 0$ condensate fraction is used up in the creation of the dual-beam atom laser (the ground state of the system is helpfully $n_0 \sim 1/2$), the compression and outcoupling process could be repeated as long as a population of $m_F = 0$ remained. We envision a compression cycle, tuned to produce a dual-beam atom laser of particular size, followed by outcoupling, followed by a second compression cycle (at higher power or for longer time to achieve equivalent coherent

mixing), then a second outcoupling, *ad infinitum*. In the limit of extremely large condensate numbers, this process could reach the limit of 50% duty cycle, where the output laser pulse is as long as the coherent mixing process between pulses.

Finally, it is worth noting the potential of the scheme for precision measurement applications. One somewhat exotic notion suggests that if a measurement is made on only one of the outcoupled beams, the number squeezing inherent to the system results in the possibility of the second (untouched) atom laser beam being forced into an undisturbed number state. Normally such a number state would be created by the direct interaction of destructive absorption imaging, or less destructive but imperfect phase-contrast imaging. Such a state would be useful for Heisenberg-limited precision phase measurements, as suggested elsewhere [147].

The next few years should see the continual rapid development of optically trapped condensate experiments focusing on the attendant spinor order parameter; such apparatus might become as commonplace as magnetic traps and (in the author's opinion) more straightforwardly accomplished. The complexity added to an already rich system should result in exciting many-body physics for years to come, as the properties of the spinor condensate are more fully explored.

Appendix A

Rubidium energy levels

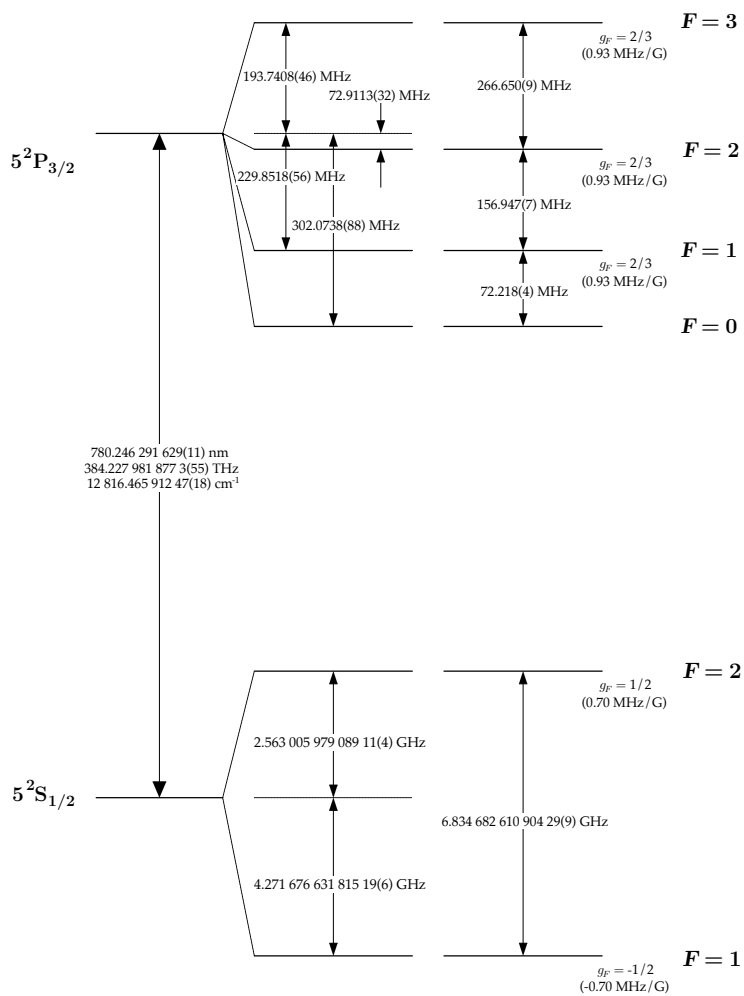


Figure A.1: ^{87}Rb D_2 energy levels, courtesy of D. Steck [137].

Appendix B

Offset lock circuit diagram

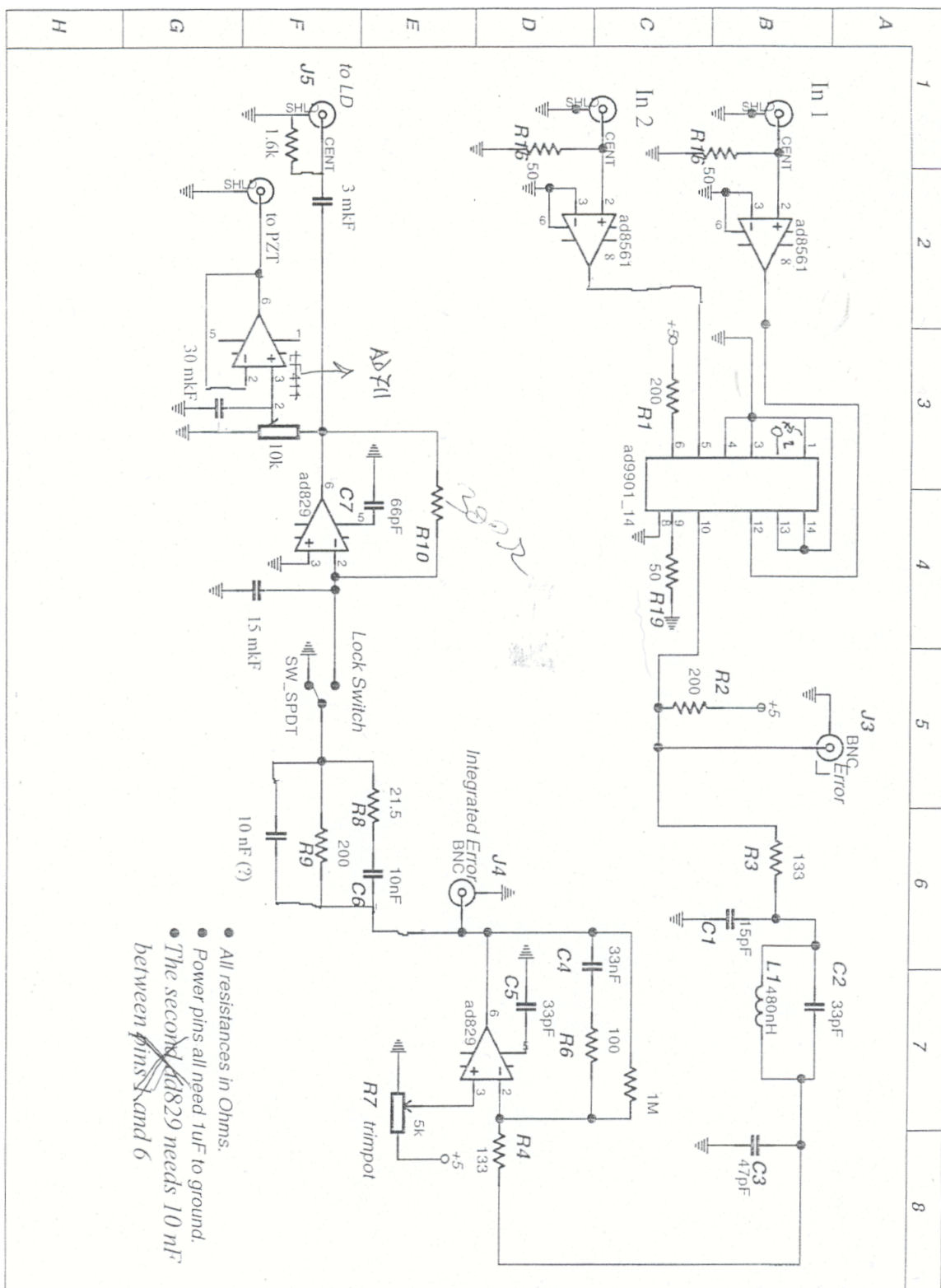


Figure B.1: Offset lock circuit diagram, courtesy of D. Strelkov.

Appendix C

Two-species cold atomic beam

PRIOR TO BEGINNING CONSTRUCTION IN EARNEST on the all-optical BEC effort, the author participated in a project utilizing an extant LVIS apparatus (depicted in Fig. C.1) to study two-species atomic beams and cold collisions. A cold atomic beam of ^{87}Rb and ^{133}Cs was created and used to load a dual-species UHV MOT. The associated trap-loss and trap-loading curves lent insight into Rb-Cs inelastic collisions. The paper resulting from these efforts is duplicated in the following pages; the LVIS apparatus itself is described in more detail elsewhere [118].

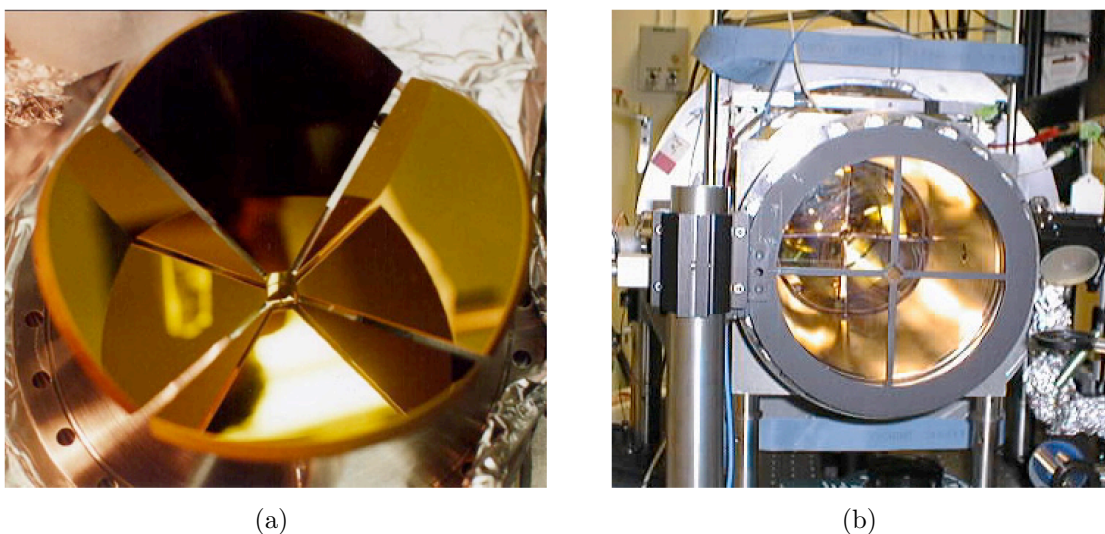


Figure C.1: (a) The pyramidal LVIS mirror. Diameter is ~ 15 cm. Note gap for retro-optic at center. (b) The LVIS chamber. Note particularly large input window and mask to control scattered light from pyramid segment edges.

Two-species cold atomic beam

Nathan Lundblad,* David C. Aveline, Robert J. Thompson, James M. Kohel, Jaime Ramirez-Serrano, William M. Klipstein, Daphna G. Enzer, Nan Yu, and Lute Maleki

Jet Propulsion Laboratory, California Institute of Technology, 4800 Oak Grove Drive, Pasadena, California 91109-8099

Received February 27, 2003; revised manuscript received August 8, 2003; accepted September 2, 2003

We generate a bright atomic beam containing laser-cooled rubidium and cesium, and we use this beam to load a mixed-species ultrahigh-vacuum (UHV) magneto-optical trap. We have characterized our two-species atomic beam over a range of operating conditions, and we obtain similar atom fluxes for each species. Within the UHV trap, interspecies inelastic collisions are observed in the form of enhanced decay rates of a given species in the presence of a second trapped species. We analyze the trap decays to obtain a loss rate due to heteronuclear cold collisions, and we compare our result to similar measurements in vapor-cell traps [Phys. Rev. A **63**, 033406 (2001)]. © 2004 Optical Society of America
OCIS codes: 140.3320, 020.7010, 020.2070.

1. INTRODUCTION

In recent years there has been increasing interest in the physics of ultracold gases composed of two or more distinct atomic species. Cold collisions in mixed-species magneto-optical traps (MOTs) have been studied for a number of alkali gases.^{1–8} Sympathetic cooling in two-species magnetic traps has allowed exploration of quantum degeneracy in a number of fermionic species,^{9–11} as well as studies of mixtures of quantum degenerate fluids.^{12,13} In addition, colocating cold atomic samples of two species under nearly identical conditions is desirable for a number of precision measurements, including electric dipole moment searches¹⁴ and tests of local Lorentz invariance¹⁵ and the equivalence principle.

Many of these experiments could be enhanced with a bright two-species cold atomic beam (CAB) source. For studies of quantum degenerate systems, such an apparatus is useful simply as a beam source of cold atoms, allowing high numbers of atoms to be trapped under ultrahigh vacuum (UHV) with a relatively compact apparatus. For studies of heteronuclear cold collisions in a UHV MOT, such a source offers capabilities that are not possible in a vapor-cell apparatus, which all other investigations to date have employed. Most importantly, the two-species beam allows the loading of each individual species to be independently controlled. Furthermore, as studies can be carried out in a UHV environment, the effects of background collisions can be effectively neglected. A bright two-species cold atomic beam would also open the door to studies of light-assisted cold heteronuclear collisions within the beam itself. Such an experiment allows one to control both the polarization of the light and the orientation of the atoms with respect to the collision axis, information that cannot be obtained from experiments conducted within a MOT.¹⁶

In this paper, we present a novel and simple two-species (¹³³Cs + ⁸⁷Rb) atomic beam source, and we utilize this beam source to perform a preliminary study of cold collisions in a separate mixed-species trap under UHV

conditions. The present experiment allows independent control of the cesium and rubidium traps; in this way we observe trap loading and decay rates for each species with and without the presence of the second species. Simple modeling of these observed differences allows measurements of the heteronuclear cold collision rate, which we compare to results from recent experiments in vapor-cell traps.⁷

2. EXPERIMENTAL DESCRIPTION

Our cold atomic beam is generated with a modified pyramidal MOT¹⁷; this apparatus has been described in a recent report.¹⁸ In brief, our pyramidal trap consists of a large four-sided pyramidal mirror assembly that is truncated just before the apex. At the truncated apex, a separate retro-optic (consisting of a $\lambda/4$ plate with a high-reflectance gold coating on the second surface) contains a 1-mm aperture. A slow beam of cold atoms is extracted through this aperture via the resulting radiation pressure imbalance.¹⁹ A detailed characterization of the single-species cesium CAB can be found in Ref. 18.

To operate our pyramidal trap as a two-species CAB source, four optical frequencies are required for laser trapping and cooling the two alkali species, as illustrated in Fig. 1. The Cs and Rb trapping lasers are combined on a nonpolarizing beam splitter (NBS). One-half the power in each beam is directed to the pyramidal MOT, and a portion of the remaining half is directed to a UHV ($P_{\text{tot}} < 10^{-10}$ Torr) MOT located 36 cm downstream from the center of the pyramidal trap in an uncoated glass cuvette. Circular polarization is approximated in the 852-nm and 780-nm trapping lasers by sending the linearly polarized beams through a single wave plate (QWP). This wave plate, with a nominal retardance of $\lambda/4$ at 850 nm, is rotated to simultaneously optimize the flux in the Cs and Rb atomic beams. Similarly, a single wave plate creates near-circular polarization in the overlapped trap ping beams for the UHV MOT. The combined beams for the pyramidal MOT are expanded by a factor of 30 to ap-

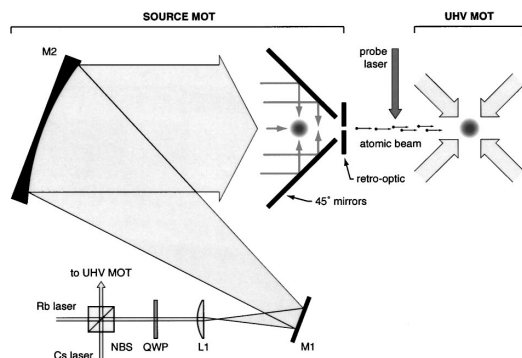


Fig. 1. Schematic diagram of the experimental apparatus, including the two-species cold atomic beam source and UHV MOT. The distance from the source to the UHV MOT is 36 cm.

proximately 15 cm in diameter and aligned into the pyramidal trap along the longitudinal (z) axis.

The lasers used for the two-species traps include a Ti:sapphire ring laser and three diode-laser systems. The trapping light for ^{87}Rb is generated by the Ti:sapphire laser, which delivers up to 200 mW of power at 780 nm to each of the two Rb traps. The repumping frequency for Rb is provided by an external-cavity diode laser (ECDL) that produces up to 15 mW at 780 nm. The trapping frequency for Cs is generated via an ECDL, which is further amplified by a tapered-cavity diode amplifier. The amplified output is coupled to the experiment via a polarization-maintaining optical fiber, so that the total Cs trapping power available to the experiment is 300–350 mW at 852 nm. Another ECDL serves as the Cs repumping laser. The Rb repumping laser is combined with the trapping lasers, while the Cs repumping laser is delivered separately via optical fibers to the source and UHV trap regions. By shuttering the repumping beams to either trap, the loading of the Cs source and UHV MOTs can be independently controlled.

3. CHARACTERIZING THE DUAL-BEAM SOURCE

We detect the atomic beams via resonance fluorescence detection with a pair of overlapping frequency-modulated

Table 1. Typical Parameters for the Cold Atomic Beam (CAB) Source and UHV MOT

	CAB Source		UHV MOT		Notes
	Cs	^{87}Rb	Cs	^{87}Rb	
I_0/I_{sat}	0.9	0.7	18	15	^a
Δ/Γ	-2.1	-2.3	-2.1	-2.3	^b
$\tilde{\Phi}$ (atoms/s)	2×10^8	1×10^8	^c
N (atoms)	6×10^8	2×10^8	

^aThe laser intensities I_0 are specified for each trapping beam, so that the total laser intensity incident on atoms in the UHV MOT is given by $I_{\text{tot}} = 6I_0$. These intensities are normalized by I_{sat} , the saturation intensity of the cycling transitions, where $I_{\text{sat}} = 1.1 \text{ mW/cm}^2$ (1.7 mW/cm^2) for Cs (^{87}Rb).

^bThe laser detunings Δ are normalized by the natural linewidths Γ , where $\Gamma = 5.2 \text{ MHz}$ (6.1 MHz) for Cs (^{87}Rb).

^cThe atom flux $\tilde{\Phi}$ is a lower bound derived from the UHV MOT loading rates and assuming a unit capture efficiency.

probe beams tuned to the $^{87}\text{Rb } 5S_{1/2}, F = 2 \rightarrow 5P_{3/2}, F' = 3$ and Cs $6S_{1/2}, F = 4 \rightarrow 6P_{3/2}, F' = 5$ transitions. A detuning of -11 MHz ($-2.1\Gamma_{\text{Cs}}$, where $\Gamma_{\text{Cs}} = 5.2 \text{ MHz}$) for the Cs trapping laser was found to optimize the flux of the Cs beam; for Rb, the optimum detuning was found at $\Delta \approx -14 \text{ MHz}$ ($-2.3\Gamma_{\text{Rb}}$, where $\Gamma_{\text{Rb}} = 6.1 \text{ MHz}$). A magnetic-field gradient of approximately 3 G/cm was found to simultaneously optimize the flux of the Cs and Rb atomic beams. By varying the angle of the probe with respect to the atomic beams, we determine the mean velocity of each atomic species from the resulting Doppler shift. The mean velocity of the Rb beam was measured to be 10 m/s for typical operating conditions (cf. Table 1); the Cs beam velocity, measured at a much higher laser intensity ($I = 3I_{\text{sat}}$), was 15 m/s .¹⁸ The divergence of the CAB is geometrically limited, and this divergence was previously measured to be 15 mrad for the Cs beam in the current apparatus.¹⁸

The UHV MOT was characterized by employing two calibrated CCD cameras with narrow-band optical filters to selectively image the trapped Cs and Rb atom clouds. The calibrated imaging system allows us to determine the atom number as well as the loading and decay rates for the UHV trap. Our reported values for the atom flux (cf. Table 1) are determined from the loading rates observed in the UHV MOT and assuming a capture efficiency of unity²⁰; these values should be taken as lower bounds on the atomic beam flux. We note, however, that the fluxes reported here are still an order of magnitude lower than what we have measured previously in the single-species Cs CAB generated in this same apparatus.¹⁸ Much of this difference can be attributed to the lower optical powers (one third to one fourth) available to the pyramidal source MOT in the present study. This dual-species beam performance could be enhanced, however, by simply employing the appropriate dichroic beam splitter and wave plates to allow a greater fraction of the available laser powers at 780 nm and 852 nm to be simultaneously directed to the source MOT. The current experimental parameters and performance figures for the CAB and UHV MOT are summarized in Table 1.

Typical loading curves for the Rb and Cs UHV MOTs are shown in Fig. 2, where both species are present in the CAB but not in the UHV MOT. Here we are suddenly switching ($< 2 \text{ ms}$) on the repumper light for one species in both the source and UHV MOT regions, allowing us to study the dynamics of the combined system of source MOT, propagating beam, and UHV MOT. The gradual onset of the MOT loading curves in Fig. 2 results from the time of formation of the CAB, including the time of flight of atoms from the source to the UHV trap. We attribute the faster onset for loading into the Cs UHV MOT to the higher Cs vapor pressure in the source region, and thus a faster time of formation for the Cs beam.

4. STUDYING HETERONUCLEAR COLD COLLISIONS WITH THE TWO-SPECIES BEAM

We observe no measurable change in the flux of the Rb beam when the Cs beam is present, and vice versa; from this we conclude that heteronuclear cold collisions are not

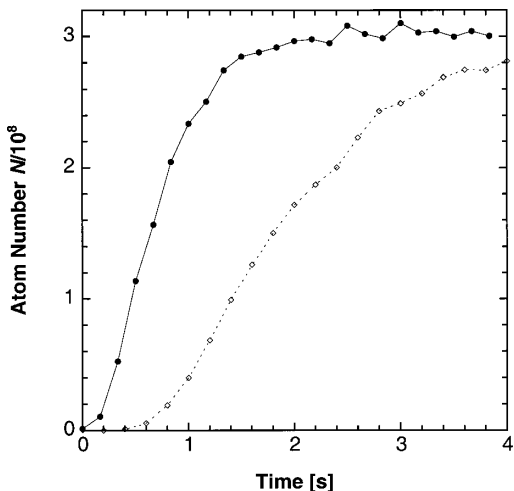


Fig. 2. Loading curves for the Cs (dots) and Rb (diamonds) UHV traps after switching on the cold atomic beam source.

a significant loss mechanism in the pyramidal trap or within the freely propagating beam. This is not unexpected, as the loss rate due to trapped atoms being extracted into the CAB dominates over all other loss mechanisms within the pyramidal MOT, and the densities within the atomic beam ($< 2 \times 10^7$ atom/cm³) are still an order of magnitude too low for these cold collisions to be observed.^{16,21,22}

The effect of heteronuclear cold collisions is readily apparent within the mixed-species UHV MOT, however. We observe decreased trap lifetimes for the Cs MOT in the presence of simultaneously trapped Rb, and vice versa. This behavior is illustrated in Fig. 3. From analysis of the observed Cs MOT decay rates with and without the cold Rb background, we obtain a measure of the loss rate due to heteronuclear cold collisions as detailed below.

Following the approach of Telles *et al.*,⁷ we describe the general time dependence of our Cs UHV MOT using the rate equation¹⁶

$$\frac{dN_{Cs}}{dt} = L - \gamma N_{Cs} - \beta \int_V n_{Cs}^2 d\mathbf{r} - \beta' \int_V n_{Cs} n_{Rb} d\mathbf{r}, \quad (1)$$

where L is the loading rate (from the atomic beam), γ is the loss rate due to collisions between the trapped cesium atoms and the thermal background gas, β is the loss rate due to cold collisions among trapped cesium atoms, β' is the cesium loss rate due to cold collisions with trapped rubidium atoms, N_{Cs} is the number of trapped cesium atoms, and n_{Cs} and n_{Rb} are the density profiles of cesium and rubidium atoms in the UHV MOT. We observe the decay of the Cs MOT by switching off the Cs loading beam ($L \rightarrow 0$) while leaving the Rb beam and MOT in steady state. All of our data were taken in the density-limited regime, where both n_{Rb} and n_{Cs} are constant within the trap. In this regime, Eq. (1) can be expressed as the decay rate equation

$$\frac{dN_{Cs}}{dt} = -(\beta n_{Cs} + \beta' n_{Rb} F) N_{Cs}, \quad (2)$$

where the loading rate L is zero and we have also taken the loss rate γ to be zero for the UHV trap. The factor F represents the relative overlap of the Rb and Cs trapped atoms; from fluorescence images of the UHV MOT, we estimate $F \approx 0.8$ immediately after Cs loading is switched off, and this factor approaches unity within 0.5 s of decay. We fit the MOT decay curves with single exponential functions, as in Fig. 3. The initial points in which the overlap F between the two trapped species may be varying are not included in fits to the “two-species” decays (although these points typically affect the result by less than one percent). From fits to the single-species Cs MOT decays and using the measured trap density n_{Cs} , we determine a collisional loss rate $\beta = 5 \times 10^{-11}$ cm³/s. This result is consistent with previous work,²³ although we note that the current measurement is at a significantly higher laser intensity. The cross-species collisional loss rate β' is determined from the difference in decay rates for the Cs MOT with and without the cold Rb atom background, yielding a value of

$$\beta'_{Cs-Rb} = \eta(0.7 \pm 0.2) \times 10^{-11} \text{ cm}^3/\text{s}, \quad (3)$$

where the uncertainty results from the scatter in the single exponential fits to six pairs of decays (each similar to those in Fig. 3), and the factor $\eta = 1.0 \pm 0.2$ represents the error due to uncertainties in the atomic densities. This loss rate is comparable to the rates measured by Telles *et al.*⁷ for Rb trap losses due to collisions with cold Cs atoms (β'_{Rb-Cs}) at similar laser intensities, although, as noted by these authors, there is no *a priori* reason to expect the reciprocal loss rates to be equal.²⁴

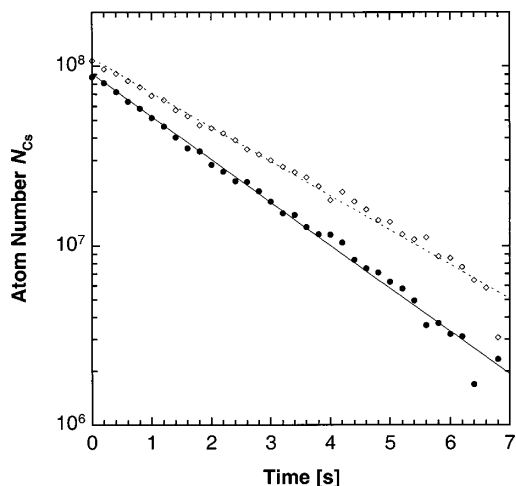


Fig. 3. Typical decay of the Cs UHV MOT with (dots) and without (diamonds) the presence of cold Rb atoms. The solid and dotted curves are least-squares fits of the data to single exponential decays with and without the cold Rb background, respectively. The fit to the “two-species” decay (solid curve) omits the first three data points, as discussed in the text.

5. SUMMARY AND CONCLUSIONS

To our best knowledge, this is the first demonstration of a two-species continuous cold atomic beam based on three-dimensional laser cooling. Recently, a high-flux two-species Zeeman-slowed atomic beam was demonstrated by Hadzibabic *et al.*¹² The relative advantages and disadvantages of MOT-based atomic beam sources versus other beam sources have been discussed previously.^{18,19}

We have utilized our two-species beam to load a mixed-species UHV MOT, and cross-species interaction effects were observed via the measured decay rates in the UHV trap. The current experiment allows independent control of the loading and decay of each species within the UHV trap, and the effects of cold collisions in the UHV MOT are isolated from the usual losses due to thermal gas backgrounds. These initial measurements hint at the broad utility of this two-species atomic beam plus UHV MOT system in the nascent field of heteronuclear cold-collision studies.

This simple and robust two-species atomic beam source may also prove useful in future experiments requiring comparison between two or more atomic species, including a proposed test of the equivalence principle that has been selected for development as a future National Aeronautics and Space Administration Microgravity Research Program flight experiment.²⁵ Further work is underway to optimize performance of this source while minimizing the size and power requirements for flight applications.

ACKNOWLEDGMENTS

We would like to acknowledge helpful discussions with Eric Burt. This research was carried out at the Jet Propulsion Laboratory, California Institute of Technology, under a contract with the National Aeronautics and Space Administration, and was supported by the Jet Propulsion Laboratory Director's Research and Development Fund. One of the authors (N. Lundblad) is partially supported by a California Institute of Technology Robert Andrews Millikan Graduate Fellowship.

*Also at Department of Physics, California Institute of Technology, Pasadena, California 91125. Electronic address: lundblad@caltech.edu.

REFERENCES AND NOTES

- M. S. Santos, P. Nussenzveig, L. G. Marcassa, K. Helmer, J. Flemming, S. C. Zilio, and V. S. Bagnato, "Simultaneous trapping of two different atomic species in a vapor-cell magneto-optical trap," *Phys. Rev. A* **52**, R4340–R4343 (1995).
- G. D. Telles, L. G. Marcassa, S. R. Muniz, S. G. Miranda, A. Antunes, C. Westbrook, and V. S. Bagnato, "Inelastic cold collisions of a Na/Rb mixture in a magneto-optical trap," *Phys. Rev. A* **59**, R23–R26 (1999).
- J. P. Shaffer, W. Chalupczak, and N. P. Bigelow, "Trap loss in a two-species Na–Cs magneto-optical trap: Intramultiplet mixing in heteronuclear ultracold collisions," *Phys. Rev. A* **60**, R3365–R3368 (1999).
- U. Schlöder, H. Engler, U. Schünemann, R. Grimm, and M. Weidemüller, "Cold inelastic collisions between lithium and cesium in a two-species magneto-optical trap," *Eur. Phys. J. D* **7**, 331–340 (1999).
- Y. E. Young, R. Ejnisman, J. P. Shaffer, and N. P. Bigelow, "Heteronuclear hyperfine-state-changing cold collisions," *Phys. Rev. A* **62**, 055403 (2000).
- L. G. Marcassa, G. D. Telles, S. R. Muniz, and V. S. Bagnato, "Collisional losses in a K-Rb cold mixture," *Phys. Rev. A* **63**, 013413 (2001).
- G. D. Telles, W. Garcia, L. G. Marcassa, V. S. Bagnato, D. Ciampini, M. Fazzi, J. H. Müller, D. Wilkowski, and E. Arimondo, "Trap loss in a two-species Rb-Cs magneto-optical trap," *Phys. Rev. A* **63**, 033406 (2001).
- J. Goldwin, S. B. Papp, B. DeMarco, and D. S. Jin, "Two-species magneto-optical trap with ⁴⁰K and ⁸⁷Rb," *Phys. Rev. A* **65**, 021402(R) (2002).
- A. G. Truscott, K. E. Strecker, W. I. McAlexander, G. B. Partridge, and R. G. Hulet, "Observation of Fermi pressure in a gas of trapped atoms," *Science* **291**, 2570–2572 (2001).
- B. DeMarco and D. S. Jin, "Onset of Fermi degeneracy in a trapped atomic gas," *Science* **285**, 1703–1706 (1999).
- R. Onofrio and C. Presilla, "Reaching Fermi degeneracy in two-species optical dipole traps," *Phys. Rev. Lett.* **89**, 100401 (2002).
- Z. Hadzibabic, C. A. Stan, K. Dieckmann, S. Gupta, M. W. Zwierlein, A. Görlitz, and W. Ketterle, "Two-species mixture of quantum degenerate Bose and Fermi gases," *Phys. Rev. Lett.* **88**, 160401 (2002).
- G. Modugno, G. Roati, F. Riboli, F. Ferlaino, R. J. Brecha, and M. Inguscio, "Collapse of a degenerate Fermi gas," *Science* **297**, 2240–2243 (2002).
- B. C. Regan, E. D. Commins, C. J. Schmidt, and D. DeMille, "New limit on the electron electric dipole moment," *Phys. Rev. Lett.* **88**, 071805 (2002).
- D. Bear, R. E. Stoner, R. L. Walsworth, V. A. Kostelecký, and C. D. Lane, "Limit on Lorentz and CPT violation of the neutron using a two-species noble-gas maser," *Phys. Rev. Lett.* **85**, 5038–5041 (2000).
- J. Weiner, V. S. Bagnato, S. Zilio, and P. S. Julienne, "Experiments and theory in cold and ultracold collisions," *Rev. Mod. Phys.* **71**, 1–85 (1999).
- K. I. Lee, J. A. Kim, H. R. Noh, and W. Jhe, "Single beam atom trap in a pyramidal and conical hollow mirror," *Opt. Lett.* **21**, 1177–1179 (1996).
- J. Kohel, J. Ramirez-Serrano, R. J. Thompson, L. Maleki, J. L. Bliss, and K. G. Libbrecht, "Generation of an intense cold atom beam from a pyramidal magneto-optical trap: Experiment and simulation," *J. Opt. Soc. Am. B* **20**, 1161–1168 (2003).
- Z. T. Lu, K. L. Corwin, M. J. Renn, M. H. Anderson, E. A. Cornell, and C. E. Wieman, "Low-velocity intense source of atoms from a magneto-optical trap," *Phys. Rev. Lett.* **77**, 3331–3334 (1996).
- Detailed Monte-Carlo simulations of the CAB-loaded UHV MOT predict that the capture efficiency of cold atoms from the atomic beam by the UHV MOT is approximately 70 percent; this efficiency is limited primarily by the small (1 cm) diameter for the trapping laser beams.
- J. Ramirez-Serrano, W. DeGraffenreid, and J. Weiner, "Polarization-dependent spectra in the photoassociative ionization of cold atoms in a bright sodium beam," *Phys. Rev. A* **65**, 052719 (2002).
- J. Ramirez-Serrano, W. DeGraffenreid, J. Weiner, E. Tiesinga, and P. Julienne, "Beamless spectroscopy of cold collisions in a bright sodium beam," *Phys. Rev. A* (to be published).
- D. Sesko, T. Walker, C. Monroe, A. Gallagher, and C. Wieman, "Collisional losses from a light-force atom trap," *Phys. Rev. Lett.* **63**, 961–964 (1989).
- While the primary focus of Ref. 7 was the study of Rb trap losses from cold collisions with Cs, the authors mention that they also measured a value for $\beta'_{\text{Cs-Rb}}$ that was twenty times lower than the corresponding value for $\beta'_{\text{Rb-Cs}}$. We are uncertain as to whether this result is actually inconsistent with ours, as the trap parameters were not specified for their measurement.
- See <http://funphysics.jpl.nasa.gov/technical/library/pilist.html>.

Appendix D

High power frequency doubling

A publication regarding the doubled 1560 nm fiber laser is attached as this Appendix, as is a photograph of the doubling apparatus in its current state.

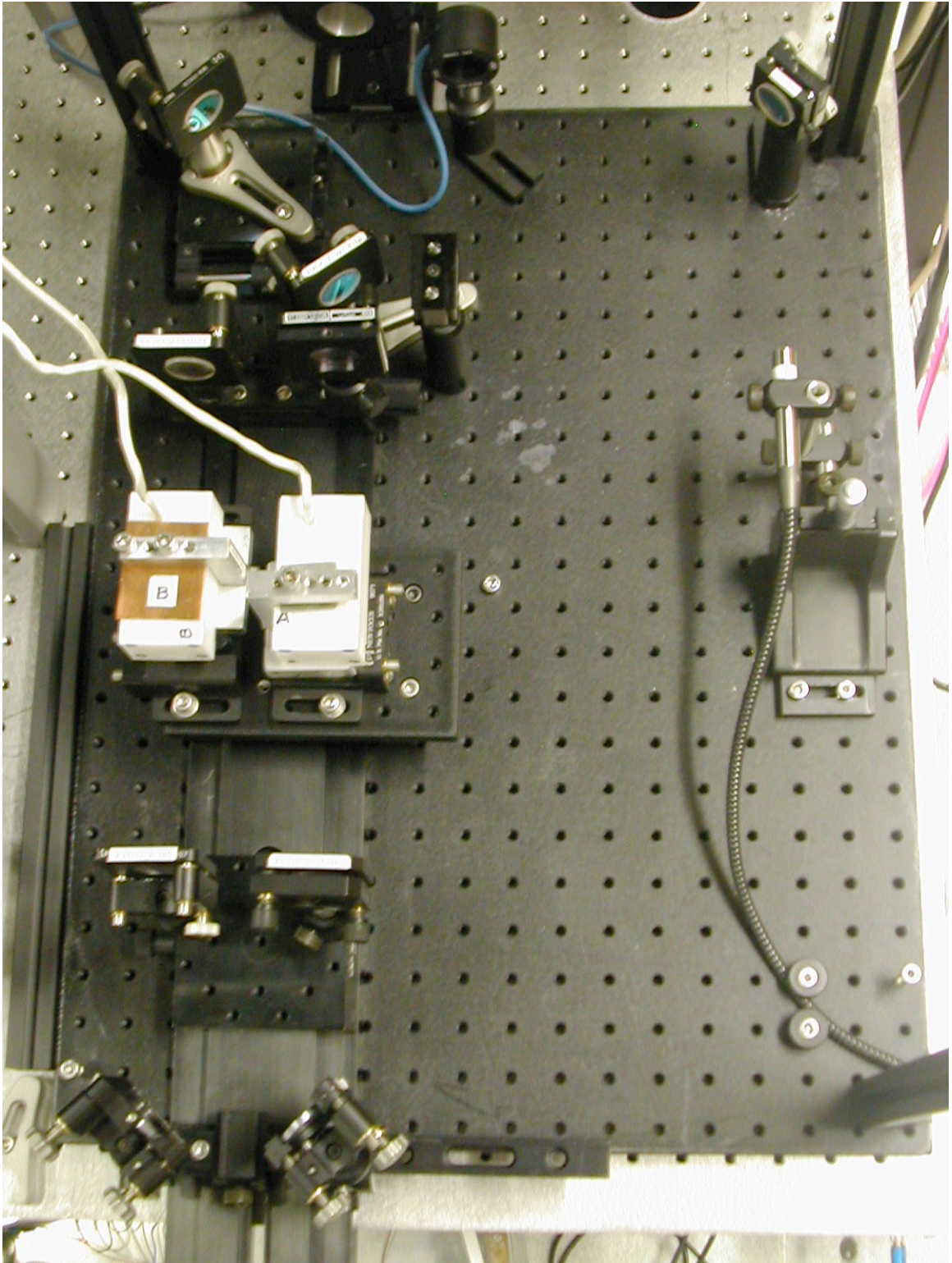


Figure D.1: *Photograph of the doubling setup. The displayed area is usually enclosed to keep dust out and the 5 W of 1560 nm laser light in.*

High power single frequency 780nm laser source generated from frequency doubling of a seeded fiber amplifier in a cascade of PPLN crystals

R. J. Thompson, M. Tu, D. C. Aveline, N. Lundblad, L. Maleki

Jet Propulsion Laboratory, California Institute of Technology, 4800 Oak Grove Drive, Pasadena, California 91109
Robert.J.Thompson@JPL.nasa.gov

Abstract: We report on the generation of over 900 mW of tunable cw light at 780 nm by single pass frequency doubling of a high power fiber amplifier in a cascade of two periodically poled Lithium Niobate (PPLN) crystals. Over 500 mW is generated in the first crystal. In the limit of low pump power, we observe an efficiency of 4.6 mW/W²-cm for a single crystal, and 5.6 mW/W²-cm for a combination of two crystals, with an enhancement of the doubling efficiency observed with two crystals due to the presence of second harmonic light from the first crystal acting as a seed for the second. We have frequency locked this laser source relative to a rubidium D2 hyperfine line and demonstrated its utility in a sophisticated laser cooling apparatus.

©2003 Optical Society of America

OCIS codes: (190.2620) Frequency conversion; (140.3510) Lasers, fiber; 020.7010 Trapping

References and Links

1. G. D. Miller, R.G. Batchko, W. M. Tulloch, M.M. Fejer, and R.L. Byer, "42%-efficient single-pass cw second-harmonic generation in periodically poled lithium niobate," *Opt. Lett.* **22**, 1834-1836 (1997).
 2. P.A. Champert, S.V. Popov, and J.R. Taylor, "Power scalability to 6W of 770 nm source based on seeded fibre amplifier and PPKTP," *Electron. Lett.* **37**, 1127-1129 (2001).
 3. D. Fluck, and P. Gunter, "Efficient second-harmonic generation by lens wave-guiding in KNbO₃ crystals," *Opt. Comm.* **147**, 305-308 (1998).
 4. K. Dieckmann, R.J.C. Spreeuw, M.Weidemuller, and J.T.M. Walraven, "Two-dimensional magneto-optical trap as a source of slow atoms," *Phys. Rev. A* **58**, 3891-3895 (1998).
 5. C. Wieman, G. Flowers, and S. Gilbert, "A narrow-band tunable diode laser system with grating feedback, and a saturated absorption spectrometer for Cs and Rb," *Am. J. Phys.* **63**, 317 (1995).
 6. S. Peil, S. Crane, and C.R. Ekstrom, "High power frequency doubling for the production of 780 nm light," to appear in Proceedings of the Joint Meeting of the European Frequency and Time Forum and IEEE International Frequency Control Symposium (2003).
-

1. Introduction

Rubidium has rapidly become the workhorse of atomic vapor based instruments used for sensing and metrology. The unique properties of this atom at cold temperatures also make it a favorite species for laser cooling, and in particular for Bose-Einstein condensation experiments. Most of these applications, nevertheless, require as much as a Watt of laser power at 780 nm (the resonance frequency of the D2 line of rubidium) for cooling and internal state preparation. In particular, NASA is interested in performing a series of laser cooling experiments on the International Space Station over the coming decade which will involve rubidium atoms. A significant technical challenge for such missions is developing a robust, efficient, high power laser system. There have, however, been no convenient means for generating this much power with a single source, with the required narrow linewidths. The recent commercial availability of very high power (over 10 watt) fiber amplifiers at a wide

variety of wavelengths in the near infrared, coupled with highly efficient frequency doubling using periodically poled nonlinear crystals [1,2], has the potential of dramatically altering the landscape of laser sources for atomic physics.

In this letter, we report on a 780 nm source suitable for atomic physics experiments involving rubidium employing an Er doped fiber amplifier (EDFA), which is confocally focused into a succession of two periodically poled Lithium Niobate (PPLN) crystals. This configuration acts as a “lens waveguide”, and for ideal focusing, no insertion loss, and no saturation, increases the SHG output of two crystals by a factor of four relative to that of one crystal [3]. We have characterized the performance of this laser system and demonstrated its utility in a laser cooling apparatus consisting of a 2-D magneto-optical trap (MOT) [4] loading a downstream ultra high vacuum MOT.

2. Experimental methods

A schematic of the apparatus is shown in Fig. 1. A commercial Yb/Er doped fiber amplifier (IPG Photonics model EAD-5-C-LP-JL) is seeded by an external cavity diode laser (New Focus Vortex model 6029), producing up to 5 W of cw power at 1560 nm. We have also used a distributed feedback (DFB) laser as a seed laser, and obtained similar results. Output from the fiber amplifier is collimated, and confocally focused into the first PPLN crystal (crystal-1), recollimated, and then again confocally focused into the second crystal (crystal-2). Each of the PPLN crystals (manufactured by Deltronics, Inc.) are 50 mm long, 0.5 mm thick, with a 19 μm domain period chosen for quasi-phase matching at 100 $^{\circ}\text{C}$. They are anti-reflection coated at both 1560 nm and 780 nm. The two mirrors after the first crystal are mounted on a rail, allowing the relative phase between the fundamental and the second harmonic to be varied by adjusting the path length between the two crystals. The difference of the index of refraction of air between the fundamental and the SH is about 1.6 ppm, so that a path length difference of about 49 cm corresponds to a full wave retardation of the 780 nm light with respect to the 1560 nm light.

A dichroic beam splitter (DBS) is used to separate the second harmonic (transmitted) from the fundamental (reflected). At low powers, each crystal had an insertion loss of approximately 4% for the fundamental. The SH power is measured on a NIST traceable photodiode (PD).

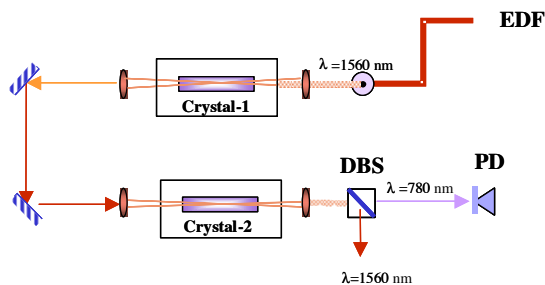


Fig. 1. Schematic diagram of experimental apparatus.

3. Results and discussion

A plot of second harmonic power versus fundamental power is shown in Fig. 2. Here we show the SHG power from the cascade of two crystals, along with the power from each of the crystals individually. The latter plots are obtained by replacing the second mirror in the set-up

shown in Fig. 1 with a dichroic beamsplitter, so that we may monitor the SH power after the first crystal and direct only the fundamental to the second crystal. The power incident on the second crystal is of course reduced relative to that incident on the first, due to the insertion loss of the first crystal and the intervening optics, and, at higher powers, due to pump depletion. At low powers we achieve efficiencies of $4.6 \text{ mW/W}^2\text{-cm}$ for crystal one and two separately, and $5.6 \text{ mW/W}^2\text{-cm}$ for the two crystal cascade. The larger value for the cascade than for the single crystal results is a clear indication that the SH light from the first crystal is acting as a seed for the second. Insertion losses of the crystals and intervening optics, along with a non-ideal overlap of the fundamental and SH in the second crystal (simple plano-convex lenses are used to collimate the light from the first crystal and focus it into the second) prevent us from observing the doubling of the normalized efficiency that we would expect ideally. No evidence of photo-refractive damage is observed after many hours of operation at the highest pump powers.

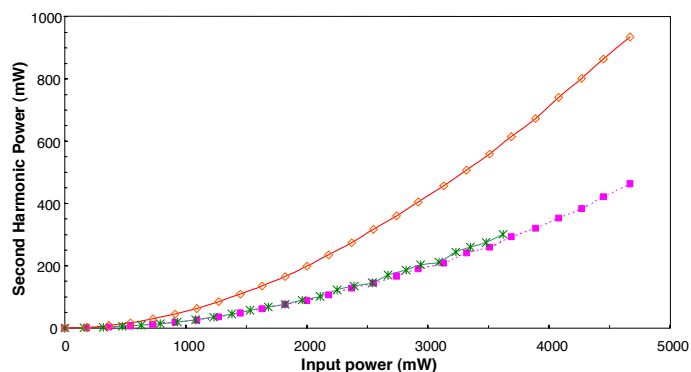


Fig. 2. Measured second harmonic power versus fundamental power after: a cascade of two crystals (diamonds), crystal-1 alone (squares), and after crystal-2, with the SH from crystal-1 removed by replacing the second of the two mirrors in Fig. 1 with a dichroic beamsplitter. For the first two cases the input power is measured at the entrance of crystal-1, for the third case it is measured at the entrance to crystal-2.

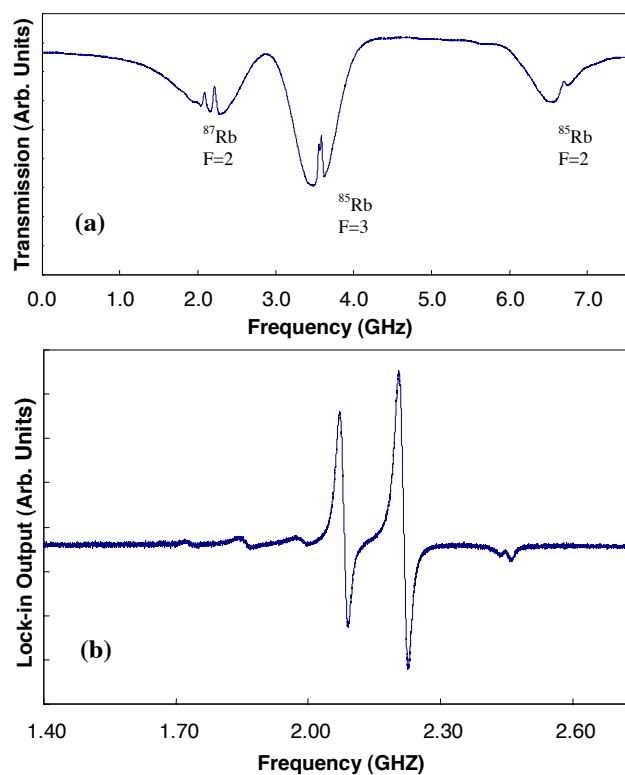


Fig. 3. (a) Saturated absorption spectrum of three of the rubidium D2 lines; (b) error signal derived from the ^{87}Rb F=2 spectrum by lock-in detection of the frequency modulated laser.

The laser system is readily tunable by adjusting the piezo voltage input of the seed laser. We can scan 50 GHz without adjusting the temperatures of the crystal ovens, and observe a 50% loss of power over that range (with a single crystal, we were able to scan 80 GHz before observing a comparable loss of power). We have servo-locked the seed laser frequency relative to the rubidium D2 hyperfine line using a standard atomic saturated absorption setup [5]. Figure 3(a) shows a saturated absorption spectrum of three of the rubidium D2 lines, while Fig. 3(b) shows an error signal generated by frequency modulating the laser output (using an acousto-optic modulator), and employing lock-in detection.

4. Conclusion

In conclusion, we have demonstrated the generation of over 900 mW of tunable cw light at 780 nm, by single pass frequency doubling in a cascade of two PPLN crystals. Over 500 mW is generated in a single crystal, corresponding to an absolute SHG efficiency of 10%. We believe this to be the highest cw SHG efficiency reported for bulk PPLN crystals in the ~ 1.5 μ m wavelength range [6], and is comparable to the best cw results reported at any wavelength [1], with appropriate wavelength scaling.

The laser system we have described is remarkably easy to align and operate. To demonstrate its utility for atomic physics experiments, we have employed the laser system in a sophisticated laser cooling experiment in which a 2-D magneto-optical trap (MOT) [4] is used to load an ultra-high vacuum MOT. In terms of loading rates, the performance is comparable to a Ti:Sapphire based system.

We note that this system allows us to take advantage of the many sophisticated optoelectronic and micro-electro-mechanical devices that have been developed for the telecommunications industry and are designed to operate near 1560 nm. Finally, we also note that high power fiber lasers are available at a wide range of wavelengths, so that the techniques discussed in this letter may be applicable for other atomic wavelengths. In particular, high power Raman fiber lasers are available at 1178 nm, and could be doubled to produce the 589 nm sodium D2 line. This wavelength is of considerable interest for high power laser guide star applications, as well as for atomic physics experiments.

Acknowledgements

We thank Drs. Nan Yu, Bill Klipstein, James Kohel, and Dave Seidel for helpful technical discussions. This research was carried out at the Jet Propulsion Laboratory, California Institute of Technology, under a contract with the National Aeronautics and Space Administration.

Bibliography

It is a noble employment to rescue from oblivion
those who deserve to be remembered.

PLINY THE YOUNGER
Letters, V.

- [1] M. H. Anderson, J. R. Ensher, M. R. Matthews, C. E. Wieman, and E. A. Cornell, “Observation of Bose-Einstein Condensation in a Dilute Atomic Vapor,” *Science* **269** (1995) 198–201. 1
- [2] K. B. Davis, M.-O. Mewes, M. R. Andrews, N. J. van Druten, D. S. Durfee, D. M. Kurn, and W. Ketterle, “Bose-Einstein condensation in a gas of sodium atoms,” *Phys. Rev. Lett.* **75** (1995) 3969. 1
- [3] C. C. Bradley, C. A. Sackett, J. J. Tollett, and R. G. Hulet, “Evidence of Bose-Einstein Condensation in an Atomic Gas with Attractive Interactions,” *Phys. Rev. Lett.* **75** (1995) 1687–1690. 1
- [4] C. C. Bradley, C. A. Sackett, J. J. Tollett, and R. G. Hulet, “Erratum: Evidence of Bose-Einstein Condensation in an Atomic Gas with Attractive Interactions [Phys. Rev. Lett. **75**, 1687 (1995)],” *Phys. Rev. Lett.* **79** (1997) 1170. 1
- [5] C. C. Bradley, C. A. Sackett, and R. G. Hulet, “Bose-Einstein Condensation of Lithium: Observation of Limited Condensate Number,” *Phys. Rev. Lett.* **78** (1997) 985–989. 1

- [6] S. L. Cornish, N. R. Claussen, J. L. Roberts, E. A. Cornell, and C. E. Wieman, “Stable ^{85}Rb Bose-Einstein Condensates with Widely Tunable Interactions,” *Phys. Rev. Lett.* **85** (2000) 1795–1798. 1
- [7] G. Modugno, G. Ferrari, G. Roati, R. J. Brecha, A. Simoni, and M. Inguscio, “Bose-Einstein Condensation of Potassium Atoms by Sympathetic Cooling,” *Science* **294** (2001) 1320–1322. 1
- [8] D. G. Fried, T. C. Killian, L. Willmann, D. Landhuis, S. C. Moss, D. Kleppner, and T. J. Greytak, “Bose-Einstein Condensation of Atomic Hydrogen,” *Phys. Rev. Lett.* **81** (1998) 3811–3814. 1
- [9] F. P. D. Santos, J. Leonard, J. Wang, C. J. Barrelet, F. Perales, E. Rasel, C. S. Unnikrishnan, M. Leduc, and C. Cohen-Tannoudji, “Bose-Einstein Condensation of Metastable Helium,” *Phys. Rev. Lett.* **86** (2001) 3459–3462. 1
- [10] A. Robert, O. Sirjean, A. Browaeys, J. Poupard, S. Nowak, D. Boiron, C. I. Westbrook, and A. Aspect, “A Bose-Einstein Condensate of Metastable Atoms,” *Science* **292** (2001) 461–464. 1
- [11] M. Wheeler, J. Erwin, and D. Hall, “Interference between Bose-Einstein Condensates Independently Prepared in Two Spin States.” The 35th Meeting of the American Physical Society (Division of Atomic, Molecular and Optical Physics), Tucson, AZ (2004). 1
- [12] M. D. Barrett, J. A. Sauer, and M. S. Chapman, “All-Optical Formation of an Atomic Bose-Einstein Condensate,” *Phys. Rev. Lett.* **87** (2001) 010404. 1, 1.2.1, 2.1, 2.3, 3.1.1
- [13] G. Cennini, G. Ritt, C. Geckeler, and M. Weitz, “All-Optical realization of an atom laser,” *Phys. Rev. Lett.* **91** (2003) 240408. 1, 1.2.1, 1.3, 3.4.2

- [14] T. Kinoshita, T. Wenger, and D. S. Weiss, “All-optical Bose-Einstein condensation using a compressible crossed dipole trap,” *Phys. Rev. A* **71** (2005) 011602. 1, 1.2.1, 4.2.2
- [15] N. Lundblad, R. J. Thompson, D. C. Aveline, and L. Maleki, “Single-beam all-optical ^{87}Rb BEC.” The 36th Meeting of the American Physical Society (Division of Atomic, Molecular and Optical Physics), Lincoln, NE (2005). 1
- [16] G. Summy. public web page. 1
- [17] D. Whitaker. private communication. 1
- [18] T. Weber, J. Herbig, M. Mark, H.-C. Nagerl, and R. Grimm, “Bose-Einstein Condensation of Cesium,” *Science* **299** (2003) 232–235. 1, 1.2.1, 1
- [19] Y. Takasu, K. Maki, K. Komori, T. Takano, K. Honda, M. Kumakura, T. Yabuzaki, and Y. Takahashi, “Spin-Singlet Bose-Einstein Condensation of Two-Electron Atoms,” *Phys. Rev. Lett.* **91** (2003) 040404. 1, 1.2.1
- [20] H. Schmaljohann, M. Erhard, J. Kronjager, M. Kottke, S. van Staa, L. Cacciapuoti, J. J. Arlt, K. Bongs, and K. Sengstock, “Dynamics of $F = 2$ Spinor Bose-Einstein Condensates,” *Phys. Rev. Lett.* **92** (2004) 040402. 1, 1.4.1
- [21] T. Kuwamoto, K. Araki, T. Eno, and T. Hirano, “Magnetic field dependence of the dynamics of ^{87}Rb spin-2 Bose-Einstein condensates,” *Phys. Rev. A* **69** (2004) 063604. 1, 1.4.1
- [22] A. Griesmaier, J. Werner, S. Hensler, J. Stuhler, and T. Pfau, “Bose-Einstein Condensation of Chromium,” *Phys. Rev. Lett.* **94** (2005) 160401. 1
- [23] S. R. Granade, M. E. Gehm, K. M. O’Hara, and J. E. Thomas, “All-Optical Production of a Degenerate Fermi Gas,” *Phys. Rev. Lett.* **88** (2002) 120405. 1, 1.2.1

- [24] K. M. O’Hara, S. L. Hemmer, M. E. Gehm, S. R. Granade, and J. E. Thomas, “Observation of a Strongly Interacting Degenerate Fermi Gas of Atoms,” *Science* **298** (2002) 2179–2182. 1
- [25] S. N. Bose, “Plancks Gesetz und Lichtquantenhypothese,” *Zeitschr. für Physik* **26** (1924) 178. 1.1
- [26] A. Einstein, “Quantentheorie des einatomigen idealen Gases,” *Sitzungsber. Kgl. Preuss. Akad. Wiss.* **1924** (1924) 261. 1.1
- [27] A. Einstein, “Quantentheorie des einatomigen idealen Gases (Zweite Abhandlung),” *Sitzungsber. Kgl. Preuss. Akad. Wiss.* **1925** (1925) 3. 1.1, 2
- [28] R. K. Pathria, *Statistical Mechanics*. Butterworth-Heinemann, 2nd edition, 1996. 1.1
- [29] E. A. Cornell, J. R. Ensher, and C. E. Wieman, “Experiments in dilute atomic Bose-Einstein condensation,” in *Bose-Einstein Condensation in Atomic Gases (Proceedings of the International School of Physics “Enrico Fermi,” Course CXL)*, M. Inguscio, S. Stringari, and C. E. Wieman, editors. IOS Press, 1999. 1.1
- [30] A. J. Leggett, “Bose-Einstein condensation in the alkali gases: Some fundamental concepts,” *Rev. Mod. Phys.* **73** (2001) 307. 1.1, 1.1.2
- [31] K. B. Davis, M.-O. Mewes, M. A. Joffe, M. R. Andrews, and W. Ketterle, “Evaporative cooling of sodium atoms,” *Phys. Rev. Lett.* **74** (1995) 5202–5205. 1.1.1, 3.1.1
- [32] N. Masuhara, J. M. Doyle, J. C. Sandberg, D. Kleppner, T. J. Greytak, H. F. Hess, and G. P. Kochanski, “Evaporative cooling of spin-polarized atomic hydrogen,” *Physical Review Letters* **61** (1988) 935–938. 1.1.1

- [33] F. Dalfovo, S. Giorgini, L. P. Pitaevskii, and S. Stringari, “Theory of Bose-Einstein condensation in trapped gases,” *Reviews of Modern Physics* **71** (1999) 463–512. 1.1.2, 1.1.2
- [34] L. Pitaevskii and S. Stringari, *Bose-Einstein Condensation (International Series of Monographs on Physics)*. Oxford University Press, 2003. 1.1.3
- [35] S. Chu, L. Hollberg, J. E. Bjorkholm, A. Cable, and A. Ashkin, “Three-dimensional viscous confinement and cooling of atoms by resonance radiation pressure,” *Phys. Rev. Lett.* **55** (1985) 48–51. 1.2
- [36] P. D. Lett, R. N. Watts, C. I. Westbrook, W. D. Phillips, P. L. Gould, and H. J. Metcalf, “Observation of atoms laser cooled below the Doppler limit,” *Phys. Rev. Lett.* **61** (1988) 169–172. 1.2
- [37] E. Raab, M. Prentiss, A. Cable, S. Chu, and D. Pritchard, “Trapping of neutral sodium atoms with radiation pressure,” *Phys. Rev. Lett.* **59** (1987) 2631. 1.2, 2.2.2
- [38] A. L. Migdall, J. V. Prodan, W. D. Phillips, T. H. Bergeman, and H. J. Metcalf, “First observation of magnetically trapped neutral atoms,” *Phys. Rev. Lett.* **54** (1985) 2596–2599. 1.2
- [39] R. Grimm, M. Weidemuller, and Y. B. Ovchinnikov, “Optical dipole traps for neutral atoms,” *Adv. Atom. Mol. Opt. Phys.* **42** (2000) 95. 1.2
- [40] S. Chu, J. E. Bjorkholm, A. Ashkin, and A. Cable, “Experimental observation of optically trapped atoms,” *Phys. Rev. Lett.* **57** (1986) 314–317. 1.2.1
- [41] A. Ashkin, “Trapping of atoms by resonance radiation pressure,” *Physical Review Letters* **40** (1978) 729–733. 1.2.1
- [42] J. D. Miller, R. A. Cline, and D. J. Heinzen, “Far-off-resonance optical trapping of atoms,” *Phys. Rev. A* **47** (1993) R4567. 1.2.1, 3.1.1

- [43] C. S. Adams, H. J. Lee, N. Davidson, M. Kasevich, and S. Chu, “Evaporative cooling in a crossed dipole trap,” *Phys. Rev. Lett.* **74** (1995) 3577–3580. 1.2.1, 3.1.1
- [44] T. Takekoshi and R. J. Knize, “CO₂ laser trap for cesium atoms,” *Opt. Lett.* **21** (1996) 77–79. 1.2.1
- [45] T. Takekoshi, J. R. Yeh, and R. J. Knize, “Quasi-electrostatic trap for neutral atoms,” *Opt. Comm.* **114** (1995) 421–424. 1.2.1, 3.1.1
- [46] S. Friebel, C. D’Andrea, J. Walz, M. Weitz, and T. W. Hänsch, “CO₂-laser optical lattice with cold rubidium atoms,” *Phys. Rev. A* **57** (1998) R20–R23. 1.2.1, 3.2.3
- [47] S. Friebel, R. Scheunemann, J. Walz, T. W. Hänsch, and M. Weitz, “Laser cooling in a CO₂-laser optical lattice,” *Appl. Phys. B* **67** (1998) 699–704. 1.2.1
- [48] H. Engler, T. Weber, M. Mudrich, R. Grimm, and M. Weidemüller, “Very long storage times and evaporative cooling of cesium atoms in a quasidelectrostatic dipole trap,” *Phys. Rev. A* **62** (2000) 031402. 1.2.1
- [49] T. A. Savard, K. M. O’Hara, and J. E. Thomas, “Laser-noise-induced heating in far-off resonance optical traps,” *Phys. Rev. A* **56** (1997) R1095–R1098. 1.2.1
- [50] K. M. O’Hara, M. E. Gehm, S. R. Granade, and J. E. Thomas, “Scaling laws for evaporative cooling in time-dependent optical traps,” *Phys. Rev. A* **64** (2001) 051403. 1.2.1, 3.3.2, 3.3.2
- [51] M. E. Gehm, K. M. O’Hara, T. A. Savard, and J. E. Thomas, “Dynamics of noise-induced heating in atom traps,” *Phys. Rev. A* **58** (1998) 3914–3921. 1.2.1
- [52] K. M. O’Hara, S. R. Granade, M. E. Gehm, and J. E. Thomas, “Loading dynamics of CO₂laser traps,” *Phys. Rev. A* **63** (2001) 043403. 1.2.1

- [53] K. M. O'Hara, S. R. Granade, M. E. Gehm, T. A. Savard, S. Bali, C. Freed, and J. E. Thomas, "Ultrastable CO₂ Laser Trapping of Lithium Fermions," *Phys. Rev. Lett.* **82** (1999) 4204–4207. 1.2.1
- [54] D. M. Stamper-Kurn, M. R. Andrews, A. P. Chikkatur, S. Inouye, H.-J. Miesner, J. Stenger, and W. Ketterle, "Optical Confinement of a Bose-Einstein Condensate," *Phys. Rev. Lett.* **80** (1998) 2027–2030. 1.2.1, 1.4
- [55] G. Cennini, G. Ritt, C. Geckeler, and M. Weitz, "Bose-Einstein condensation in a CO₂-laser optical dipole trap," *Appl. Phys. B* **77** (2003) 773–779. 1.2.1
- [56] Y. Takasu, K. Honda, K. Komori, T. Kuwamoto, M. Kumakura, Y. Takahashi, and T. Yabuzaki, "High-Density Trapping of Cold Ytterbium Atoms by an Optical Dipole Force," *Phys. Rev. Lett.* **90** (2003) 023003. 1.2.1
- [57] T. Kinoshita, T. Wenger, and D. S. Weiss, "Observation of a One-Dimensional Tonks-Girardeau Gas," *Science* **305** (2004) 1125–1128. 1.2.1
- [58] A. L. Schawlow and C. H. Townes, "Infrared and Optical Masers," *Phys. Rev.* **112** (1958) 1940–1949. 1.3
- [59] T. H. Maiman, "Stimulated Optical Radiation in Ruby," *Nature* **187** (1960) 493–494. 1.3
- [60] A. Javan, W. R. Bennett Jr., and D. R. Herriott, "Population Inversion and Continuous Optical Maser Oscillation in a Gas Discharge Containing a He-Ne Mixture," *Physical Review Letters* **6** (1961) 106–110. 1.3
- [61] M. W. Mitchell, C. I. Hancox, and R. Y. Chiao, "Dynamics of atom-mediated photon-photon scattering," *Phys. Rev. A* **62** (2000) 043819. 4
- [62] M. W. Mitchell, C. I. Hancox, and R. Y. Chiao, "Dynamics of Atom-Mediated Photon-Photon Scattering II: Experiment," [physics/0002013](#). 4

- [63] M. W. Mitchell, *Dynamics of Photon-Photon Scattering In Rubidium Vapor*. Ph.D. thesis, University of California, Berkeley, 1999. 4
- [64] M. R. Andrews, C. G. Townsend, H.-J. Miesner, D. S. Durfee, D. M. Kurn, and W. Ketterle, “Observation of Interference Between Two Bose Condensates,” *Science* **275** (1997) 637–641. 1.3
- [65] M.-O. Mewes, M. R. Andrews, D. M. Kurn, D. S. Durfee, C. G. Townsend, and W. Ketterle, “Output Coupler for Bose-Einstein Condensed Atoms,” *Phys. Rev. Lett.* **78** (1997) 582–585. 1.3
- [66] I. Bloch, T. W. Hansch, and T. Esslinger, “Atom Laser with a cw Output Coupler,” *Physical Review Letters* **82** (1999) 3008–3011. 1.3
- [67] E. W. Hagley, L. Deng, M. Kozuma, J. Wen, K. Helmerson, S. L. Rolston, and W. D. Phillips, “A Well-Collimated Quasi-Continuous Atom Laser,” *Science* **283** (1999) 1706–1709. 1.3
- [68] J. Stenger, S. Inouye, D. Stamper-Kurn, H.-J. Miesner, A. Chikkatur, and W. Ketterle, “Spin domains in ground-state Bose-Einstein condensates,” *Nature* **396** (1998) 345. 1.4, 1.4, 1.4.1
- [69] H.-J. Miesner, D. M. Stamper-Kurn, J. Stenger, S. Inouye, A. P. Chikkatur, and W. Ketterle, “Observation of Metastable States in Spinor Bose-Einstein Condensates,” *Phys. Rev. Lett.* **82** (1999) 2228–2231. 1.4
- [70] D. M. Stamper-Kurn, H.-J. Miesner, A. P. Chikkatur, S. Inouye, J. Stenger, and W. Ketterle, “Quantum Tunneling across Spin Domains in a Bose-Einstein Condensate,” *Phys. Rev. Lett.* **83** (1999) 661–665. 1.4
- [71] C. J. Myatt, E. A. Burt, R. W. Ghrist, E. A. Cornell, and C. E. Wieman, “Production of Two Overlapping Bose-Einstein Condensates by Sympathetic Cooling,” *Phys. Rev. Lett.* **78** (1997) 586–589. 1.4

- [72] T.-L. Ho, “Spinor Bose Condensates in Optical Traps,” *Phys. Rev. Lett.* **81** (1998) 742–745. 1.4, 1.4.1
- [73] T. Ohmi and K. Machida, “Bose-Einstein condensation with internal degrees of freedom in alkali atom gases,” *J. Phys. Soc. Japan* **67** (1998) 1822. 1.4, 1.4.1
- [74] E. G. M. van Kempen, S. J. J. M. F. Kokkelmans, D. J. Heinzen, and B. J. Verhaar, “Interisotope Determination of Ultracold Rubidium Interactions from Three High-Precision Experiments,” *Phys. Rev. Lett.* **88** (2002) 093201. 1.4, 4.1.2
- [75] N. N. Klausen, J. L. Bohn, and C. H. Greene, “Nature of spinor Bose-Einstein condensates in rubidium,” *Phys. Rev. A* **64** (2001) 053602. 1.4, 4.1.2
- [76] H. Pu, C. K. Law, S. Raghavan, J. H. Eberly, and N. P. Bigelow, “Spin-mixing dynamics of a spinor Bose-Einstein condensate,” *Phys. Rev. A* **60** (1999) 1463–1470. 1.4.1
- [77] C. K. Law, H. Pu, and N. P. Bigelow, “Quantum Spins Mixing in Spinor Bose-Einstein Condensates,” *Phys. Rev. Lett.* **81** (1998) 5257–5261. 1.4.1
- [78] M.-S. Chang, C. D. Hamley, M. D. Barrett, J. A. Sauer, K. M. Fortier, W. Zhang, L. You, and M. S. Chapman, “Observation of Spinor Dynamics in Optically Trapped ^{87}Rb Bose-Einstein Condensates,” *Phys. Rev. Lett.* **92** (2004) 140403. 1.4.1, 1.4.1, 4.1.1, 4.1.1, 4.2.2
- [79] S. Yi, O. E. Mustecaplioglu, C. P. Sun, and L. You, “Single-mode approximation in a spinor-1 atomic condensate,” *Phys. Rev. A* **66** (2002) 011601. 1.4.1
- [80] W. Zhang, S. Yi, and L. You, “Mean field ground state of a spin-1 condensate in a magnetic field,” *New J. Phys.* **5** (2003) 77.1. 1.4.1

- [81] J. Kronjager, C. Becker, M. Brinkmann, R. Walser, P. Navez, K. Bongs, and K. Sengstock, “Evolution of a spinor condensate: Coherent dynamics, dephasing, and revivals,” *Phys. Rev. A* **72** (2005) 063619. 1.4.1
- [82] J. Mur-Petit, M. Guilleumas, A. Polls, A. Sanpera, M. Lewenstein, K. Bongs, and K. Sengstock, “Dynamics of $F = 1$ [sup 87]Rb condensates at finite temperatures,” *Phys. Rev. A* **73** (2006) 013629. 1.4.1
- [83] M. Erhard, H. Schmaljohann, J. Kronjager, K. Bongs, and K. Sengstock, “Bose-Einstein condensation at constant temperature,” *Phys. Rev. A* **70** (2004) 031602. 1.4.1
- [84] M.-S. Chang, Q. Qin, W. Zhang, L. You, and M. S. Chapman, “Coherent spinor dynamics in a spin-1 Bose condensate,” *Nature Phys.* **1** (2005) 111. 1.4.1, 4.1.2
- [85] W. Zhang, D. L. Zhou, M.-S. Chang, M. S. Chapman, and L. You, “Dynamical Instability and Domain Formation in a Spin-1 Bose-Einstein Condensate,” *Phys. Rev. Lett.* **95** (2005) 180403. 1.4.1
- [86] W. Zhang, D. L. Zhou, M.-S. Chang, M. S. Chapman, and L. You, “Coherent spin mixing dynamics in a spin-1 atomic condensate,” *Phys. Rev. A* **72** (2005) 013602. 1.4.1
- [87] A. Widera, F. Gerbier, S. Fölling, T. Gericke, O. Mandel, and I. Bloch, “Coherent Collisional Spin Dynamics in Optical Lattices,” *Phys. Rev. Lett.* **95** (2005) 190405. 1.4.1
- [88] A. Einstein, B. Podolsky, and N. Rosen, “Can Quantum-Mechanical Description of Physical Reality Be Considered Complete?,” *Phys. Rev.* **47** (1935) 777. 1.4.2

- [89] J. S. Bell, *Speakable and Unspeakable in Quantum Mechanics: Collected Papers on Quantum Philosophy*. Cambridge University Press, 2nd edition, 2004. 1.4.2
- [90] A. Sørensen, L.-M. Duan, J. I. Cirac, and P. Zoller, “Many-particle entanglement with Bose-Einstein condensates,” *Nature* **409** (2001) 63–66. 1.4.2
- [91] A. Micheli, D. Jaksch, J. I. Cirac, and P. Zoller, “Many-particle entanglement in two-component Bose-Einstein condensates,” *Phys. Rev. A* **67** (2003) 013607. 1.4.2
- [92] N. Bigelow, “Quantum engineering: Squeezing entanglement,” *Nature* **409** (2001) 27–28. 1.4.2
- [93] A. P. Hines, R. H. McKenzie, and G. J. Milburn, “Entanglement of two-mode Bose-Einstein condensates,” *Phys. Rev. A* **67** (2003) 013609. 1.4.2
- [94] K. Helmerson and L. You, “Creating Massive Entanglement of Bose-Einstein Condensed Atoms,” *Phys. Rev. Lett.* **87** (2001) 170402. 1.4.2
- [95] M. Zhang, K. Helmerson, and L. You, “Entanglement and spin squeezing of Bose-Einstein-condensed atoms,” *Phys. Rev. A* **68** (2003) 043622. 1.4.2
- [96] L. You, “Creating Maximally Entangled Atomic States in a Bose-Einstein Condensate,” *Phys. Rev. Lett.* **90** (2003) 030402. 1.4.2
- [97] S. A. Haine and J. J. Hope, “Outcoupling from a Bose-Einstein condensate with squeezed light to produce entangled-atom laser beams,” *Phys. Rev. A* **72** (2005) 033601. 1.4.2
- [98] M. G. Moore and P. Meystre, “Generating Entangled Atom-Photon Pairs from Bose-Einstein Condensates,” *Phys. Rev. Lett.* **85** (2000) 5026–5029. 1.4.2

- [99] M. G. Moore, O. Zobay, and P. Meystre, “Quantum optics of a Bose-Einstein condensate coupled to a quantized light field,” *Phys. Rev. A* **60** (1999) 1491–1506. 1.4.2
- [100] H. Jing, J.-L. Chen, and M.-L. Ge, “Quantum-dynamical theory for squeezing the output of a Bose-Einstein condensate,” *Phys. Rev. A* **63** (2001) 015601. 1.4.2
- [101] M. Fleischhauer and S. Gong, “Stationary Source of Nonclassical or Entangled Atoms,” *Phys. Rev. Lett.* **88** (2002) 070404. 1.4.2
- [102] H. Pu and P. Meystre, “Creating Macroscopic Atomic Einstein-Podolsky-Rosen States from Bose-Einstein Condensates,” *Phys. Rev. Lett.* **85** (2000) 3987. 1.4.2, 4.2
- [103] L.-M. Duan, A. Sorenson, J. I. Cirac, and P. Zoller, “Squeezing and Entanglement of Atomic Beams,” *Phys. Rev. Lett.* **85** (2000) 3991. 1.4.2, 4.2
- [104] L.-M. Duan, J. I. Cirac, and P. Zoller, “Quantum entanglement in spinor Bose-Einstein condensates,” *Phys. Rev. A* **65** (2002) 033619. 1.4.2
- [105] O. E. Mustecaplioglu, M. Zhang, and L. You, “Spin squeezing and entanglement in spinor condensates,” *Phys. Rev. A* **66** (2002) 033611. 1.4.2
- [106] K. V. Kheruntsyan, M. K. Olsen, and P. D. Drummond, “Einstein-Podolsky-Rosen Correlations via Dissociation of a Molecular Bose-Einstein Condensate,” *Phys. Rev. Lett.* **95** (2005) 150405. 1.4.2
- [107] E. V. Goldstein and P. Meystre, “Phase conjugation of multicomponent Bose-Einstein condensates,” *Phys. Rev. A* **59** (1999) 1509–1513. 1.4.2
- [108] E. V. Goldstein and P. Meystre, “Quantum theory of atomic four-wave mixing in Bose-Einstein condensates,” *Phys. Rev. A* **59** (1999) 3896–3901. 1.4.2

- [109] J. Vogels, K. Xu, and W. Ketterle, “Generation of Macroscopic Pair-Correlated Atomic Beams by Four-Wave Mixing in Bose-Einstein Condensates,” *Phys. Rev. Lett.* **89** (2002) 020401. 1.4.2
- [110] G. D. Miller, R. G. Batchko, W. M. Tulloch, D. R. Weise, M. M. Fejer, and R. L. Byer, “42%-efficient single-pass cw second-harmonic generation in periodically poled lithium niobate,” *Opt. Lett.* **22** (1997) 1834–1836. 2.1.1
- [111] P. Champert, S. Popov, and J. Taylor, “Power scalability to 6 W of 770 nm source based on seeded fibre amplifier and PPKTP,” *Electr. Lett.* **37** (2001) 1127–1129. 2.1.1
- [112] P. A. Champert, S. V. Popov, and J. R. Taylor, “3.5 W frequency-doubled fiber-based laser source at 772 nm,” *Appl. Phys. Lett.* **78** (2001) 2420–2421. 2.1.1
- [113] R. J. Thompson, M. Tu, D. C. Aveline, N. Lundblad, and L. Maleki, “High power single frequency 780nm laser source generated from frequency doubling of a seeded fiber amplifier in a cascade of PPLN crystals,” *Optics Express* **11** (2003) 1709. 3
- [114] V. Mahal, A. Arie, M. A. Arbore, and M. M. Fejer, “Quasi-phase-matched frequency doubling in a waveguide of a 1560-nm diode laser and locking to the rubidium D 2 absorption lines,” *Opt. Lett.* **21** (1996) 1217–1219. 3
- [115] D. Fluck and P. Günter, “Efficient second-harmonic generation by lens wave-guiding in KNbO₃ crystals,” *Opt. Comm.* **147** (1998) 305–308. 2.1.1
- [116] N. Lundblad, D. C. Aveline, R. J. Thompson, J. M. Kohel, J. Ramirez-Serrano, W. M. Klipstein, D. G. Enzer, N. Yu, and L. Maleki, “Two-species cold atomic beam,” *J. Opt. Soc. Am. B* **21** (2004) 3–6. 2.2.1, 2.2.2

- [117] Z. T. Lu, K. L. Corwin, M. J. Renn, M. H. Anderson, E. A. Cornell, and C. E. Wieman, “Low-Velocity Intense Source of Atoms from a Magneto-optical Trap,” *Phys. Rev. Lett.* **77** (1996) 3331–3334. 2.2.2
- [118] J. M. Kohel, J. Ramirez-Serrano, R. J. Thompson, L. Maleki, J. L. Bliss, and K. G. Libbrecht, “Generation of an intense cold-atom beam from a pyramidal magneto-optical trap: experiment and simulation,” *J. Opt. Soc. Am. B* **20** (2003) 1161–1168. 2.2.2, C
- [119] R. S. Williamson, P. A. Voytas, R. T. Newell, and T. G. Walker, “A magneto-optical trap loaded from a pyramidal funnel,” *Optics Express* **3** (1998) 111. 2.2.2
- [120] J. J. Arlt, O. Maragò, S. Webster, S. Hopkins, and C. J. Foot, “A pyramidal magneto-optical trap as a source of slow atoms,” *Opt. Comm.* **157** (1998) 303–309. 2.2.2
- [121] A. Camposeo, A. Piombini, F. Cervelli, F. Tantussi, F. Fuso, and E. Arimondo, “A cold cesium atomic beam produced out of a pyramidal funnel,” *Opt. Comm.* **200** (2001) 231–239. 2.2.2
- [122] E. Riis, D. S. Weiss, K. A. Moler, and S. Chu, “Atom funnel for the production of a slow, high-density atomic beam,” *Phys. Rev. Lett.* **64** (1990) 1658–1661. 2.2.2
- [123] T. Swanson, N. Silva, S. Mayer, J. Maki, and D. McIntyre, “Rubidium atomic funnel,” *J. Opt. Soc. Am. B* **13** (1996) 1833. 2.2.2
- [124] P. Berthoud, A. Joyet, G. Dudley, N. Sagna, and P. Thomann, “A continuous beam of slow, cold cesium atoms magnetically extracted from a 2D magneto-optical trap,” *Europhys. Lett.* **41** (1998) 141. 2.2.2

- [125] K. Dieckmann, R. J. C. Spreeuw, M. Weidemuller, and J. T. M. Walraven, “Two-dimensional magneto-optical trap as a source of slow atoms,” *Phys. Rev. A* **58** (1998) 3891–3895. 2.2.2
- [126] J. Schoser, A. Batar, R. Low, V. Schweikhard, A. Grabowski, Y. B. Ovchinnikov, and T. Pfau, “Intense source of cold Rb atoms from a pure two-dimensional magneto-optical trap,” *Phys. Rev. A* **66** (2002) 023410. 2.2.2, 2.2.2
- [127] S. Weyers, E. Aucouturier, C. Valentin, and N. Dimarcq, “A continuous beam of cold cesium atoms extracted from a two-dimensional magneto-optical trap,” *Opt. Comm.* **143** (1997) 30–34. 2.2.2
- [128] J. Ramirez-Serrano, N. Yu, J. M. Kohel, J. R. Kellogg, and L. Maleki, “Multistage two-dimensional magneto-optical trap as a compact cold atom beam source,” *Opt. Lett.* **31** (2006) 682–684. 2.2.2, 2.2.2
- [129] H. J. Metcalf and P. van der Straten, *Laser Cooling and Trapping*. Springer-Verlag, 1999. 2.2.2
- [130] C. G. Townsend, N. H. Edwards, C. J. Cooper, K. P. Zetie, C. J. Foot, A. M. Steane, P. Szriftgiser, H. Perrin, and J. Dalibard, “Phase-space density in the magneto-optical trap,” *Phys. Rev. A* **52** (1995) 1423–1440. 2.2.2
- [131] P. Ahmadi, V. Ramareddy, and G. S. Summy, “Multiple micro-optical atom traps with a spherically aberrated laser beam,” *New J. Phys.* **7** (2005) 4. 7
- [132] P. W. Milonni and J. H. Eberly, *Lasers*. John Wiley & Sons, 1988. 2.3.1
- [133] M. D. Barrett, *A QUEST for BEC: an all optical alternative*. Ph.D. thesis, Georgia Institute of Technology, 2002. 2.3.3, 3.1.1, 3.1.2, 3.2.2
- [134] W. Ketterle, D. S. Durfee, and D. M. Stamper-Kurn, “Making, probing and understanding Bose-Einstein condensates,” in *Bose-Einstein Condensation in*

- Atomic Gases (Proceedings of the International School of Physics “Enrico Fermi,” Course CXL)*, M. Inguscio, S. Stringari, and C. E. Wieman, editors. IOS Press, 1999. 3.1.1
- [135] W. Ketterle, K. B. Davis, M. A. Joffe, A. Martin, and D. E. Pritchard, “High densities of cold atoms in a dark spontaneous-force optical trap,” *Phys. Rev. Lett.* **70** (1993) 2253–2256. 3.1.1
- [136] R. Dumke, M. Johanning, E. Gomez, J. D. Weinstein, K. M. Jones, and P. D. Lett, “All-optical generation and photoassociative probing of sodium Bose-Einstein condensates,” [physics/0602108](#). 1, 3.4
- [137] D. Steck, *Rubidium D Line Data*. Unpublished, 2003. Available at: <http://steck.us/alkalidata/>. 3.1.2, 3.2.1, 4.1.1, A.1
- [138] E. Burt. private communication. 3.2.1
- [139] J. R. Ensher, *The First Experiments with Bose-Einstein Condensation of ^{87}Rb* . Ph.D. thesis, University of Colorado, Boulder, 1998. 3.2.1
- [140] L. D. Landau and E. M. Lifshitz, *Course of Theoretical Physics, Volume 1: Mechanics*. Pergamon Press, 3rd edition, 1976. Translated from the Russian by J. B. Sykes and J. S. Bell. 3.2.3, 3.2.3, 3.2.3
- [141] O. J. Luiten, M. W. Reynolds, and J. T. M. Walraven, “Kinetic theory of the evaporative cooling of a trapped gas,” *Phys. Rev. A* **53** (1996) 381–389. 3.3.2
- [142] E. A. Burt, R. W. Ghrist, C. J. Myatt, M. J. Holland, E. A. Cornell, and C. E. Wieman, “Coherence, Correlations, and Collisions: What One Learns about Bose-Einstein Condensates from Their Decay,” *Phys. Rev. Lett.* **79** (1997) 337–340. 4.1.2
- [143] P. Ahmadi, B. P. Timmons, and G. S. Summy, “Geometrical effects in the loading of an optical atom trap,” *Phys. Rev. A* **72** (2005) 023411. 4.2.2

- [144] A. Gorlitz, T. L. Gustavson, A. E. Leanhardt, R. Low, A. P. Chikkatur, S. Gupta, S. Inouye, D. E. Pritchard, and W. Ketterle, “Sodium Bose-Einstein Condensates in the $F = 2$ State in a Large-Volume Optical Trap,” *Phys. Rev. Lett.* **90** (2003) 090401. 4.2.2
- [145] A. Marte, T. Volz, J. Schuster, S. Durr, G. Rempe, E. G. M. van Kempen, and B. J. Verhaar, “Feshbach Resonances in Rubidium 87: Precision Measurement and Analysis,” *Phys. Rev. Lett.* **89** (2002) 283202. 4.2.2
- [146] M. Erhard, H. Schmaljohann, J. Kronjager, K. Bongs, and K. Sengstock, “Measurement of a mixed-spin-channel Feshbach resonance in ^{87}Rb ,” *Phys. Rev. A* **69** (2004) 032705. 4.2.2
- [147] P. Bouyer and M. A. Kasevich, “Heisenberg-limited spectroscopy with degenerate Bose-Einstein gases,” *Phys. Rev. A* **56** (1997) R1083–R1086. 4.2.2

Vita

NATHAN ERIC LUNDBLAD was born in Ogden, Utah (USA), on September 23, 1976, to John A. and Pamela P. Lundblad. He was raised in Jerusalem (Israel), Los Angeles, and Oceanside (California) and graduated from Vista High School (Vista, California) in 1994, receiving an International Baccalaureate Full Diploma.

He attended the University of California, Berkeley, and in May 1998 graduated with a Bachelor of Arts *cum laude* in astronomy and physics; an honors thesis in physics was written, supervised by Prof. Raymond Chiao. After working for two years at MIT Lincoln Laboratory in Lexington, Massachusetts, he commenced graduate study in September 2000 at the California Institute of Technology as a Robert Andrews Millikan Graduate Fellow.

He has been advised there by Prof. Kenneth Libbrecht and supervised at the Jet Propulsion Laboratory by Dr. Lute Maleki and Dr. Robert J. Thompson. He is a member of the American Physical Society and the Optical Society of America.

This document was typeset by the author with \LaTeX on Mac OS X, using a class file adapted by Ian Swanson from M. Kelsey's and D. Zimmerman's updates of the $\LaTeX 2\epsilon$ `report` class. The text is set in Computer Modern (Gnuth, 1992), with the exception of the lettrines, which are set in Palatino (Zapf, 1948).